Spatio-temporal characterization of the Orinoco low-level jet and its representation by CMIP5/CMIP6 models

Isabel Cristina Correa Sánchez

Tesis de maestría presentada para optar al título de Magíster en Ingeniería Ambiental

Directora
Paola Andrea Arias Gómez, PhD
Co-directora
Sara Cristina Vieira Agudelo, PhD

Universidad de Antioquia
Facultad de Ingeniería
Maestría en Ingeniería Ambiental
Medellín, Antioquia, Colombia
2023

Spatio-temporal characterization of the Orinoco low-level jet and its representation by CMIP5/CMIP6 models

Isabel Cristina Correa Sánchez

Faculty of Engineering

Universidad de Antioquia

Submitted in partial fulfillment of the requirements for the
Degree Master of Environmental Engineering

Supervisor Dr. Paola Andrea Arias Gómez
Second Supervisor Dr. Sara Cristina Vieira Agudelo

October, 2022

To my mother and my sister

Acknowledgements

This work was funded by MINCIENCIAS through program No. 80740-490-2020 and by CLIMAT-AmSud through MINCIENCIAS grant No. 238-2021. I am very grateful to my advisor, Professor Paola, with whom I have worked since my undergraduate studies and who has shared her knowledge with me, has been my guide and has given me many opportunities that have marked my life, and to my co-advisor, Professor Sara, for instructing me, and for her accompaniment and support during these years.

I want to thank my mother, Gloria, and my sister Nathalia for always supporting me in my goals and unconditionally being by my side. Without them, this work would not have been possible. To my family for encouraging me. I thank my friends for their help and supportive comments throughout this process, especially Juanfer, Astrid, Valeria Gil, Isabel Castro, and Camacho.

Thank you very much to my colleagues at SIATA for all the learning and moments that have made me grow professionally and as a person. Sharing with such talented people like you has made me want to improve in everything I do.

Many thanks to all the people who have supported me, from whom I have learned, and who have always advised me.

Table of Contents

Introduction

The hydrological cycle has experienced variations worldwide associated with global climate change that have induced significant variability in the Earth system components. Atmospheric, oceanic and terrestrial processes, alongside processes of other spheres, are interconnected among them, giving a high complexity to the global and regional hydrological cycle and its understanding under different conditions (Douville et al., 2021; Yang et al., 2021). Regarding the atmospheric variability and processes, a significant change is the rise in the tropospheric air temperatures (Al-Ghussain, 2019; Gulev et al., 2021), which has induced noticeable fluctuations in weather and climatological phenomena, and in turn, has led to the intensification of the water cycle (Barichivich et al., 2018; Allan et al., 2020; Douville et al., 2021).

Focusing on South America, climate features exhibit great contrasts across the continent, with regions with high accumulated precipitation throughout the year like in western Colombia. On the other hand, other areas exhibit arid conditions as northeastern Brazil or key regions in Chile (Satyamurty et al., 1998; Anjos et al., 2021). Similar to the effects worldwide, climate change and anthropic activities have altered the observed characteristics of the climate dynamic processes in South America, particularly its hydrological cycle. They have induced changes towards wetter or drier regimes, rising temperature over land, shifts in vegetation and biome distribution, reduction in the Paramo area and snow cover, among other changes (Beck et al., 2018; Almazroui et al., 2021; Fox-Kemper et al., 2021). These changes entail high impacts on South America's social and natural systems, increasing the region's vulnerability to the effects of climate change (Magrin et al., 2014; Anjos and Toledo, 2018; Nagy et al., 2019; Castellanos et al., 2022).

Regarding water vapor and its transport through the atmosphere in South America,

a primordial element of the regional and global hydrological cycle, different studies assess the main features surrounding moisture flux in the region and its observed and projected changes. Particularly associated with rises in temperature over land or changes in the land properties, some near-surface wind circulations have experienced, and are expected to continue experimenting, strengthening in some key regions in the continent, while others may be exhibiting a weakening during the observational and projected periods (e.g., Jones, 2019; Sierra et al., 2021; Thaler et al., 2021). Either way would influence the atmospheric moisture transport in South America, with increased moisture convergence in some regions and decrease in others (e.g., Soares and Marengo, 2009; Algarra et al., 2019; Yang and Dominguez, 2019; Cerón et al., 2021).

The above indicates that the assessment of the observed features and possible future variations of the processes that influence the atmospheric moisture patterns represent a relevant research field to understand the regional processes that modulate water resources availability in South America and its projected changes. Therefore, this study focuses on a low-level jet that develops in the Orinoco basin and plays a relevant role in atmospheric moisture transport to northern South America and the Amazon: the Orinoco low-level jet (OLLJ).

We use information from the historical period in order to characterize the main features of the OLLJ and its links to regional patterns of atmospheric moisture and near-surface variables, and data from General Circulation Models (GCMs) for both the historical and projected periods, in order to assess its changes under the influence of natural and human-induced effects. Thus, the main goal of the present study is to provide a general view of the main features of the OLLJ and the simulation of its main features by GCMs in the historical and projected periods, seeking to relate the activity of the jet with specific regional hydroclimatological processes, and the impacts that changes of the OLLJ could induce in the climate patterns over northern South America.

Understanding the OLLJ can enhance the existing knowledge around the mechanisms that modulate moisture transport in the atmosphere, therefore, regional patterns of

precipitation and humidity in northern South America. The above acquires importance when considering the observed and projected changes in the Earth system and the high vulnerability of the natural and social systems in the region.

This work is developed as follows. Chapter 1 discusses the climatological features of the OLLJ according to multiple datasets. Chapter 2 evaluates the ability of different GCMs to simulate the main features of the OLLJ during the historical period. Chapter 3 analyzes the projections of the OLLJ and the regional circulation by the GCMs under different greenhouse gas (GHG) emission scenarios throughout the 21st century. Finally, Chapter 4 discusses the main findings from this work. Chapters 1 to 3 are structured as individual papers therefore the theoretical framework as well as the data and methodology considered are presented within each chapter.

Chapter 1

Climatology of the Orinoco low-level jet

1.1 Introduction

The hydrological cycle is modulated by multiple factors that define the variability of precipitation pattern over a particular region. With a relevant percentage of the country's economic activities based on agriculture and more than 60% of the energy production obtained from hydropower (Churio-Silvera et al., 2018; Carvajal-Romo et al., 2019; Correa, 2019), Colombia exhibits significant dependency on water resources. Therefore, Colombia is vulnerable to events of low water availability, as it has previously occurred during particular events of the warm phase of the El Niño-Southern Oscillation (ENSO; e.g., Poveda, 2004; Navarro-Monterroza et al., 2019; Ramírez-Tovar et al., 2021). The complexity of the study of the changes in the hydrological cycle under the context of climate change lies in the number of processes that contribute to its terrestrial and atmospheric components, for which it is necessary to analyze the characteristics of these elements and their feedback on the climate system (Allan et al., 2020; Arias et al. 2021b).

In particular, water vapor transport through the atmosphere plays a relevant role in the hydrological cycle. It allows the exchange of water vapor between sources and sinks, enhancing precipitation formation and the maintenance of ecosystems. For instance, water vapor from the oceans and terrestrial sources plays an essential role in the generation of precipitation events around the world and is expected

to strongly influence the changes in precipitation extremes as a response to fluctuations in moisture sources and their transport mechanisms, where the particularities of those changes depend on the region, the season and the features that modulate the moisture related processes (Gimeno et al., 2012; Liu et al., 2020). Atmospheric rivers and low-level jets (LLJs) are known as two effective mechanisms of moisture transport whose role in the formation of extreme events has been analyzed in previous studies (e.g. Gimeno et al., 2016; Ramos et al., 2016, 2019). In particular, increases in atmospheric moisture transport during the last decades, associated with the atmospheric circulation, have produced more extreme weather events, either in terms of intense precipitation or droughts (Bonner, 1968; Stensrud, 1996; Poveda et al., 2014; Gimeno et al., 2016; Douville et al., 2021).

LLJs are generally defined as maximum wind velocities in the first kilometers of the troposphere, and their identification around the globe can be reached by different methods (Stensrud, 1996). A common approach is based on the wind maxima in the vertical and the differences in wind speed at lower and upper levels, aiming to identify the characteristic vertical wind profile associated with a LLJ (Bonner, 1968; Ranjha et al., 2013; Jiménez-Sánchez et al., 2019; Builes-Jaramillo et al., 2022a). On the other hand, as LLJs develop in the lower troposphere, which is strongly influenced by the Planetary Boundary Layer (PBL), other approaches tend to consider both the variation of wind speed in different altitudes and the variation of wind velocities through the day (Rife et al., 2010; Algarra et al., 2019). This methodology is used to assess LLJs with a marked diurnal cycle. These LLJs experience a strengthening during nighttime and a weakening in the daytime, corresponding to the periods of stabilization and mixture of the PBL. Therefore, they are also called nocturnal LLJs.

Worldwide, different LLJs are related to regional climate patterns such as the Great Plains LLJ in North America (e.g. Weaver and Nigam, 2008; Tang et al., 2017; Ferguson, 2022), the Turkana LLJ in Africa (e.g. Munday et al., 2020; Oscar et al., 2022), or the South American LLJ (e.g. Vera et al., 2006; Jones, 2019). In northern South America, some LLJs that converge over the region are important features of the regional climate: the Caribbean LLJ over the Caribbean sea (Amador, 1998, 2008), the Choco LLJ over the eastern tropical Pacific Ocean entering to the

Colombian landmass (e.g. Poveda and Mesa, 1999; Sierra et al. 2018, 2021; Yepes et al. 2019), and the Los Llanos or the Orinoco LLJ (OLLJ) that connects northern South America with the tropical North Atlantic ocean (Torrealba and Amador, 2010; Jiménez-Sánchez et al., 2019, 2020; Builes-Jaramillo et al., 2022a, 2022b; Martínez et al., 2022).

Over northern South America, the Caribbean and Choco LLJs have received important attention (e.g., Poveda and Mesa, 1999; Wang, 2007; Whyte et al., 2007; Amador et al. 2008; Muñoz et al., 2008; Cook and Vizy, 2010; Sierra et al., 2018, 2021; Yepes et al., 2019; Loaiza Cerón et al., 2020; Morales et al., 2021; Valencia and Mejía, 2022) while the OLLJ has been less studied. The different studies assessing the OLLJ highlight the relevance of this LLJ on atmospheric moisture transport and, therefore, the hydrological cycle in the region. Poveda and Mesa (1999) identified this jet from an earlier generation of reanalyses, finding a strengthening of the low-level wind field in the eastern Andes Mountain range of northern South America. Later studies evaluate the seasonal characteristics of the OLLJ, suggesting a stronger jet during December-January-February (DJF; Montoya et al. 2001; LaBar et al. 2005; Rueda, 2015), which corresponds to the dry season in the Orinoco basin (e.g., Arias et al., 2020). Different ranges of pressure levels have been associated with the seasonal activation of the jet; however, this jet is always confined between the 1000 and 800 hPa, consistently with a LLJ. Builes-Jaramillo et al. (2022b) analyzed the interannual variability of the OLLJ associated with ENSO. Particularly, they identify that the OLLJ winds decrease (increase) over the mid and exit of the OLLJ corridor during the occurrence of El Niño (La Niña) events. These changes are modulated by decreases (increases) of the pressure gradient between the North Atlantic Subtropical High (NASH) and the near-equatorial low-pressure regions during El Niño (La Niña), inducing a decrease (increase) of the OLLJ intensity.

On the diurnal scale, the OLLJ reaches its maximum wind velocities at nighttime and early morning, according to in situ pilot balloons and radiosonde data, modeling experiments, and reanalyses. Specifically from modeling experiments, Jiménez-Sánchez et al. (2019) identified four cores of high wind magnitude along with the jet spatial extension, where the wind maximum is reached at different times of the day due

to the acceleration of the flow in association with four main processes: (i) the sea breeze incursion from the Atlantic ocean, (ii) the katabatic flow over the Andes, (iii) the expansion fans generated along the jet corridor due to the topography, and (iv) the diurnal variation of the turbulent diffusivity (Jiménez-Sánchez et al., 2020).

Some studies link the OLLJ with regional phenomena, such as the transport of pollutants from the Atlantic ocean and the Orinoco basin to central Colombia and Ecuador during February-March-April (Rodríguez-Gómez et al., 2022). On the other hand, in terms of the link between the OLLJ and precipitation and atmospheric moisture transport patterns in northern South America, Labar et al. (2005) found that during the dry season in the Orinoco basin (DJF), deep convection occurs in southern Colombia but does not occur in the jet corridor through the Venezuelan Llanos. Nieto et al. (2008) suggest that most of the water observed over the Orinoco basin derives from advective fluxes into the area, while the recycling of moisture is negligible. Moreover, Algarra et al. (2019) used a regional model to track the atmospheric moisture sources and sinks of different nocturnal LLJs, suggesting that the OLLJ plays a relevant role in water vapor transport from the tropical north Atlantic Ocean to the northwestern Amazon. Recently, Builes-Jaramillo et al. (2022a) linked the OLLJ with moisture flux and precipitation in northern South America from composite analysis during the period of activation (DJF) and the period of non-activity of the jet (June-July-August; JJA). Their results indicate that during DJF, precipitation increases south of the exit region of the jet while the moisture flux on the Orinoco basin is enhanced. On the contrary, in JJA, when the jet activity decreases, the main low-level circulation in the region is associated with the southerly cross-equatorial flow from the Amazon basin. Besides, Martinez et al. (2022) found that higher sensible heat flux and lower evaporation in the entrance of the jet can lead to the weakening of the wind flow and decreases in the cross-equatorial moisture transport to the Amazon linked to the OLLJ activity. The above suggests the role of the OLLJ on atmospheric moisture flux from the tropical north Atlantic Ocean to the Amazon basin in DJF.

Most of the state-of-the-art literature about the OLLJ focuses on its spatial and temporal characteristics and its relationship with climate patterns in northern South

America. This chapter aims to extend the analysis of the observed characteristics of the OLLJ at monthly and hourly time scales while including the processes that allow its seasonal activation and its linkage to the atmospheric moisture flux and precipitation regimes in the region.

1.2 Data and methodology

This study uses the ERA5 reanalysis (Hersbach et al., 2020) to describe the main characteristics of the OLLJ during the period 1979-2019. To evaluate the main features of this LLJ at annual and daily scales, we use zonal and meridional wind data at hourly and monthly frequencies. Initially, we compared the vertical structure of the OLLJ estimated from ERA5 to radiosonde data from one station in the Colombian Llanos to validate the reanalysis data and its capacity to capture the strengthening of the wind field in the region during DJF at different times of the day, as described in previous studies (Torrealba and Amador, 2010; Jiménez-Sánchez et al., 2019; Martínez et al., 2022). The data from the Las Gaviotas station was obtained from the Integrated Global Radiosonde Archive (IGRA) (available at https://www.ncei.noaa.gov/products/weather-balloon/integrated-global-radiosonde-archive). The ERA5 vertical profile was considered in the coordinates corresponding to the location of the station, however as ERA5 information is available since 1979 and the radiosonde record has large amounts of missing data, we considered the whole record period of the station (1973-2003; see Table 1.1), while the ERA5 vertical profiles were calculated for the period 1979-2003.

Table 1.1: Description of Las Gaviotas radiosonde station used in this study for comparison with ERA5 data. The station's ID refers to the station's identification code in IGRA.

Station	**ID**	**Latitude**	**Longitude**	**Record Period**
Las Gaviotas	COM00080241	4.5°N	70.9°W	1973-2003

This study considers the domain 20°N-10°S and 85°W-50°W, which encompasses northern South America (Figure 1.1), to assess the annual cycle of the OLLJ. To analyze the wind field associated with the jet, we use the information of zonal and meridional wind at different pressure levels. In addition to the seasonal wind fields,

we propose an index to assess the wind variability in the Orinoco basin associated with the activation of the OLLJ. We define the OLLJ index as the spatial average of the horizontal wind between the levels of 825 and 950 hPa. The wind component to be averaged (zonal wind, meridional wind, or wind magnitude) depends on the region where the index is being calculated, as the jet experiences a curvature throughout its movement from the Tropical Atlantic toward equatorial and northern South America. This approach allows the identification of the periods of strengthening and weakening of the jet and the mean wind values that the jet reaches during its activation periods. However, as this method focuses on a spatial average, it does not represent other characteristics of the jet, such as its vertical structure, the wind shear features, or the frequency of occurrence of a LLJ event.

Following the methodology used by Jiménez-Sánchez et al. (2019), we consider four regions distributed along the jet corridor to describe the characteristics of the OLLJ at monthly and hourly time scales. The four regions are C1 9.5°N-64.2°W, C2 7.5°N-67°W, C3 5°N-72°W and C4 2°N-73.5°W (Figure 1.1). The estimate of the jet index in different regions allows a comparison of the jet main features within its spatial domain.

On the other hand, Rodriguez-Gomez et al. (2022) use the region 75°W-61°W, 4ºN to analyze the vertical structure of the OLLJ. However, as the OLLJ index used in this study considers the average wind field over a spatial domain, a region including a wide range of longitudinal bands that do not correspond to the main developing domain of the jet may bias the index estimate. Thus, we restricted the domain to 3°N-5°N, 73°W-67°W (black square in Figure 1.1). Since this proposed region is located between the C3 and C4 regions, we labeled it C3.4. This region is also considered in our study to evaluate the climatological main features of the jet associated with its diurnal cycle, similar to the C1, C2, C3, and C4 regions described above.

We use the different regions defined above to compute the OLLJ index. Since this jet is mainly zonal at its entrance region (Figure 1.1), the OLLJ index at C1 and C2 regions was calculated as the domain-average zonal wind component. For the other

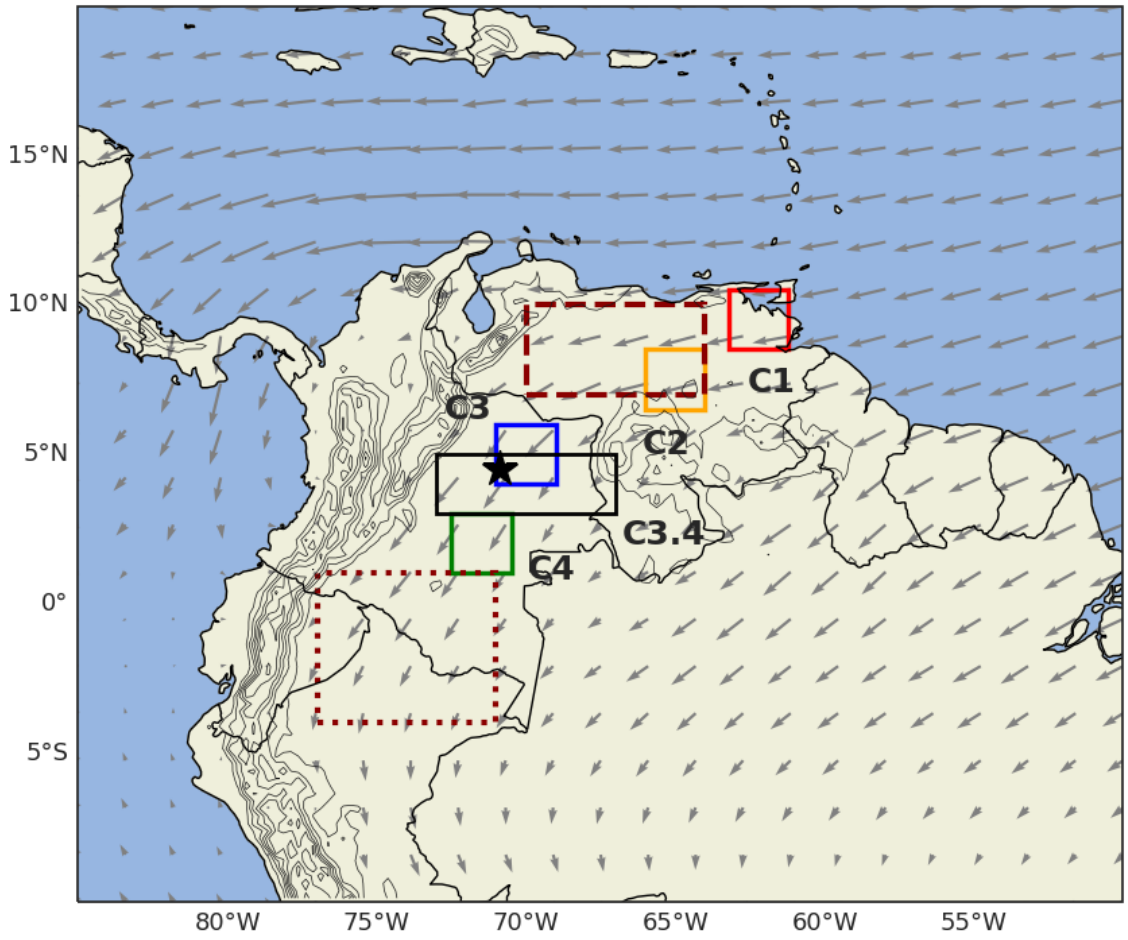

Figure 1.1: The spatial domain considered in this study. The regions C1 (red), C2 (yellow), C3 (blue) and C4 (green) are based on Jiménez-Sánchez et al. (2019). The black rectangle corresponds to the region used by Rodriguez-Gomez et al. (2022) (C3.4). The black asterisk corresponds to the location of the Las Gaviotas radiosonde station (see Table 1.1). The dark red squares represent the Orinoco (dashed) and Andes-Amazon transition (dotted) regions used by Martínez et al. (2022). Vectors represent the 850 hPa wind circulation during DJF.

regions, the index was computed as the average wind speed considering both zonal and meridional components, as the jet develops a meridional component (Figure 1.1).

The diurnal cycle of the OLLJ was evaluated from different variables that allow the analysis of the PBL variations throughout the day. This is based on the fact that the diurnal cycle of the OLLJ is influenced by the dynamics of the PBL, similarly to nocturnal LLJ in other regions. Hence, we use data from the ERA5 reanalysis for the mean boundary layer dissipation, the mean northward and eastward turbulent stress, and the mean sensible and latent heat fluxes at hourly frequency during the 1979-

2019 period in the regions along the wind corridor to assess their diurnal changes and their relationship with the wind field.

On the other hand, we propose an initial approach to understand the role of the OLLJ in the seasonal atmospheric moisture transport in northern South America using zonal and meridional wind data and specific humidity in different pressure levels at monthly frequency. For this purpose, we estimate the vertically integrated moisture flux (VIMF) using equation 1.1. The relationship between VIMF and the jet activity is identified through a simple linear regression between the monthly anomalies of the OLLJ index in all the regions and the anomalies of the VIMF at each grid cell of the spatial domain.

$$VIMF = \frac{1}{g}\int_{pl}^{pu} \mathbf{V}qdp \tag{1.1}$$

where V represents the wind vector in m/s, q is the specific humidity in kg/kg, and pu and pl are the upper and lower pressure levels in Pa.

Additionally, data of precipitation and vertically integrated moisture divergence (VIMD) from ERA5 at monthly frequency is used to evaluate the influence of the OLLJ in precipitation and atmospheric moisture divergence in northern South America. We performed a lagged correlation between the anomalies of the long-term series of the OLLJ index estimated for the different regions (Figure 1.1) and the anomalies of precipitation and VIMD at each grid cell to identify the regions of larger correlation, as well as the lag between an OLLJ strengthening/weakening and a change in the pattern of precipitation and moisture divergence.

Finally, following Martinez et al. (2022), we perform an analysis of the horizontal gradients of mean sea level pressure (MSLP) and surface sensible heat flux (SSHF) since these variables likely influence the strengthening of the OLLJ in DJF on a local scale. The two regions considered for this analysis are based on Martinez et al. (2022), defined as the Orinoco region (64°W-70°W, 7°N-10°N) and the Andes-Amazon transition region (72°W-77°W, 4°S-1°N) (Figure 1.1). In order to evaluate the role of the MSLP and the SSHF gradients between the Orinoco and the transition

region in the strengthening of the OLLJ, we consider the strongest and weakest events from the OLLJ index long-term series in the C4 region (green square in Figure 1.1). We consider this region as it is located at the jet exit, which can allow the identification of periods of higher or lower wind magnitudes associated with the jet activity. We focus on the period DJF. After obtaining the anomalies of the index time series, we define the occurrence of a stronger jet event when the anomaly is above one standard deviation of the long-term series. On the contrary, a weaker jet event is defined from the anomalies that are below one standard deviation. Finally, to assess the influence of these differences on the OLLJ dynamics, we evaluate the patterns of MSLP and SSHF gradients, estimated as the difference between the variable in the Orinoco region minus the variable in the Andes-Amazon transition region for those specific events.

1.3 Results

1.3.1 ERA5 validation

In order to identify the main features of the OLLJ using the ERA5 dataset, it is important to perform an initial validation of this reanalysis with respect to observations. Previous studies provide a first description of this LLJ using radiosonde data from multiple stations, which show the existence of a nocturnal LLJ over the Orinoco region, with a particular change in the vertical structure of the wind field during the nighttime in the period DJF (Torrealba and Amador, 2010). Following this approach, we use the observational record of wind speed provided by Las Gaviotas station, located in the Colombian Llanos. Figure 1.2 shows the vertical profile of wind speed for DJF from this radiosonde data and compares it with the estimates from ERA5. In all cases, we calculate the ERA5 profile for a set of grids that correspond to the coordinates of Las Gaviotas station (between 3.5°N-5.5°N and 69.9°W-71.9°W). On the other hand, we fill the missing records from the Las Gaviotas station by a simple linear regression to predict the missing values from the existing values. Finally, as the resultant vertical profile exhibited much noise from

one level to another, we smoothed the curve with a moving average of 5 vertical levels in the 00:00 UTC profiles and 15 levels in the 12:00:00 UTC profiles.

At a monthly scale, both the reanalysis and the radiosonde data suggest lower wind velocities during February compared to December and January, which is consistent with the periods of full development and weakening of the jet. ERA5 can represent the strengthening of the wind circulation in the nighttime and its weakening in the daytime, which has been documented as one of the main characteristics of the OLLJ during its activation period (Torrealba and Amador, 2010; Jiménez-Sánchez et al., 2019; Martínez et al., 2022). In December and January, the reanalysis tends to overestimate the wind magnitude during daytime and nighttime; however, it captures the differences in wind magnitude throughout the day: at 12:00 UTC (07:00 local time), when the boundary layer is stratified, the wind speed reaches 12 m/s; in contrast, at 00:00 UTC (19:00 local time), when the boundary layer is more mixed due to the influence of incoming solar radiation, the wind speed decreases to approximately 9 m/s. In particular, at 00:00 UTC, when we expect lower wind speeds at the surface levels, the radiosonde profile exhibits higher wind velocities at upper levels, about 600 hPa. Although the reanalysis tends to maintain the structure of maximum values at lower pressure levels, the wind speed at this time is lower than in the early morning, as observed in Figure 1.2.

The comparison of the climatological wind profile in the location of Las Gaviotas station generally agrees with the radiosonde data. It is expected to find some differences between ERA5 and the radiosonde data, mainly due to the nature of both databases: while the radiosonde records consist of in situ raw data, the ERA5 estimates consider data preprocessing as it is a product that combines different types of databases. On the other hand, the spatial average of a set of grids of the reanalysis can also add to the differences between the results from ERA5 and the radiosonde data. However, this reanalysis is helpful to evaluate the temporal and spatial characteristics of the OLLJ since it represents the enhancement of the wind field in the Colombian Llanos at nighttime during DJF and its variations throughout the day, as also indicated by radiosonde data analyzed here and in previous works (Torrealba and Amador, 2010).

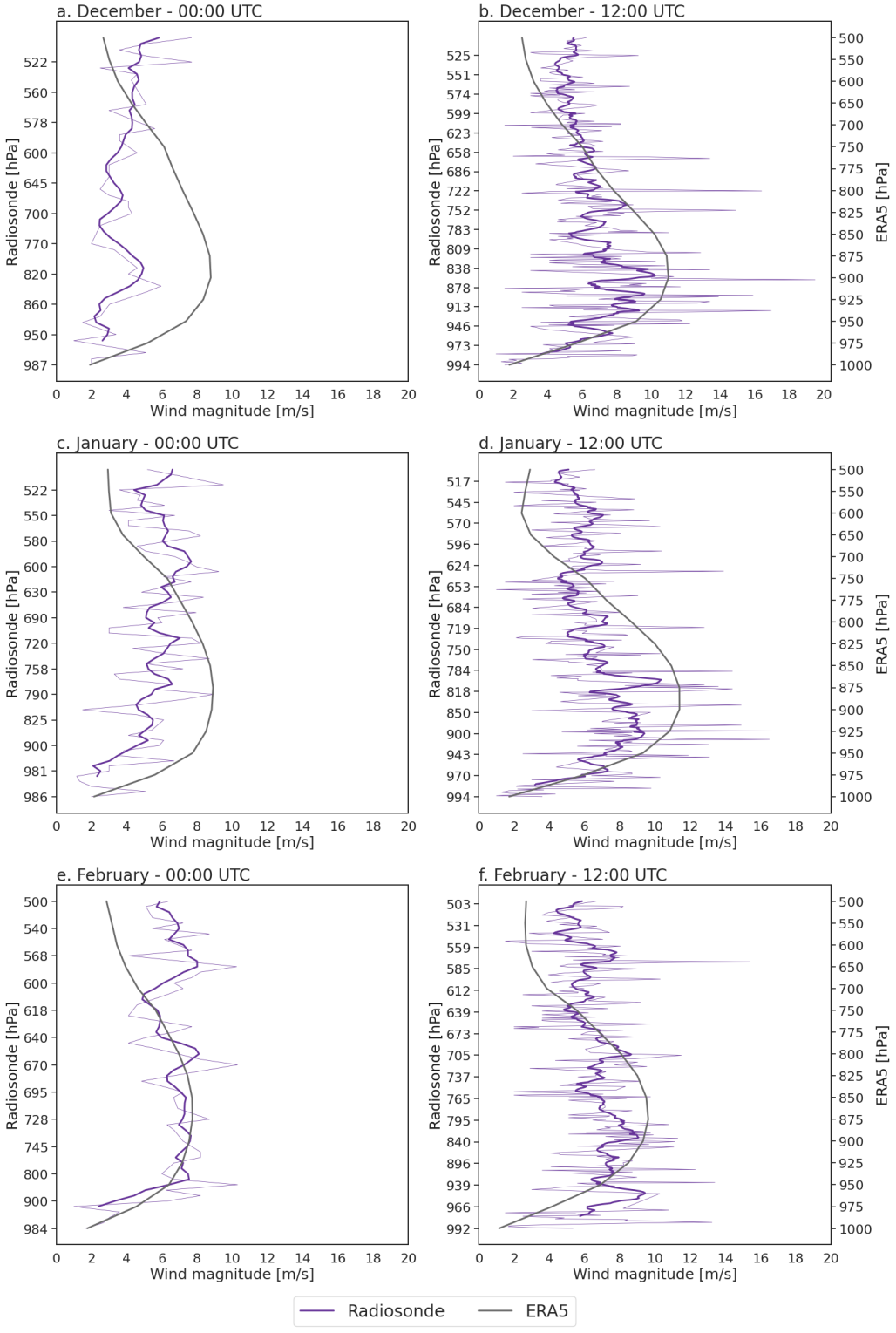

Figure 1.2: Vertical structure of the wind field from radiosonde data in Las Gaviotas station (purple line) and ERA5 data (black line). The thin violet line represents the vertical profile of the radiosonde station after predicting its missing values with linear regression. The thick violet line corresponds to the smoothed curve. a) December at 00:00 UTC, b) December at 12:00 UTC, c) January at 00:00 UTC, d) January at 12:00 UTC, e) February at 00:00 UTC, and f) February at 12:00 UTC.

1.3.2 Annual cycle of the Orinoco low-level jet

From the vertical profiles of the wind magnitude of ERA5 shown in Figure 1.2, it can be noticed that the maxima wind magnitudes are set between 825 and 950 hPa, mainly during the month of full enhancement of the OLLJ (January). Thus, we used these two pressure levels as the range to evaluate the climatology of this LLJ. During DJF, the wind field experiences a strengthening through the Orinoco basin, reaching the Colombian Amazon (Figure 1.3). In March-April-May (MAM), the wind field reduces its magnitude and spatial coverage to reach its minimum during JJA. Hence, ERA5 shows a marked annual cycle of the OLLJ with full development and maximum spatial extension during the dry season of the Orinoco basin (DJF) and with its weakest period during the wet season in the basin (JJA).

Figure 1.3 shows the seasonal variation of the horizontal wind field associated with the OLLJ and its vertical structure at the jet exit (75°W-61°W, 3°N-5ºN). The figure highlights the difference in the vertical structure of the OLLJ during the enhancement and weakening phases of this circulation. Among the regions located at the OLLJ exit (C3, C3.4, and C4; see Figure 1.1), we selected one containing region C3.4 since it encompasses more longitudinal bands and allows better identification of the LLJ variations throughout its vertical cross-section. Figure 1.3 shows that the wind field in the Colombian Llanos experiences a strengthening during DFJ, exhibiting a development of the vertical structure of the jet with its core below 800 hPa. The jet centered at 4°N seems to develop between 73°W and 67°W and this location is strongly influenced by the regional topography, allowing the strengthening of the wind field between the Los Andes mountain range and the Guinea highlands. In JJA, the wind field decreases its magnitude to values lower than 1 m/s below 800 hPa, indicating the period of less activity of the OLLJ. Finally, in SON, the wind magnitudes approximately at 900 hPa increase, marking the activation of the OLLJ.

The spatial distribution of the wind circulation associated with the OLLJ is characterized by the change in the wind direction when crossing the South American landmass, mainly driven by the region's topography. At its entrance, the jet has a strong zonal direction, while at its exit, the low-level circulation has substantial con-

tributions from both components of the horizontal wind field. Therefore, we estimate the OLLJ index for different regions (see Figure 1.1) using different components of the horizontal wind (Figure 1.4). At the jet entrance (C1 and C2), the meridional wind component (line with x) exhibits the lowest values and relatively minor changes throughout the year, suggesting that the horizontal wind magnitude in these regions is strongly related to the zonal component while the meridional component does not have such a significant contribution. On the other hand, at the jet exit (regions C3, C3.4, and C4), both zonal and meridional wind components exhibit larger values in DJF and lower in JJA, similar to the behavior of the OLLJ. Therefore, both wind components have relevant contributions to the resultant wind magnitude. Considering the features of the horizontal wind at lower levels, we define the OLLJ index in regions C1 and C2 as the spatial average of the zonal wind while in the remaining regions (C3, C3.4, and C4), the OLLJ index is estimated using the horizontal wind magnitude using the zonal and meridional components. It is relevant to mention that the OLLJ index uses the spatial average of the horizontal wind speed in a range of pressure levels as a proxy of the jet activity (between 825 and 950 hPa), which is helpful to evaluate climatological features of the jet; however, this approach does not measure other characteristics as the occurrence of specific jet events or its vertical structure.

1.3.3 Diurnal cycle of the Orinoco low-level jet

Figure 1.5 presents the OLLJ index at hourly time scale. The diurnal cycle of the OLLJ is characterized by higher wind speeds in the early morning, when the heating associated with the incoming solar radiation is still weak. Later in the afternoon, the wind speed reaches its minima values along the jet corridor. These variations in wind speed throughout the day indicate that the OLLJ can be classified as a nocturnal LLJ that experiences its strengthening through nighttime and until the early morning. The markers (x) in Figure 1.5 correspond to the maximum values of the OLLJ index during its diurnal cycle for each of the five regions considered (Figure 1.1), indicating that the major intensity of the OLLJ through the day does not occur at the same time along the jet corridor but takes place in the early morning: in C1

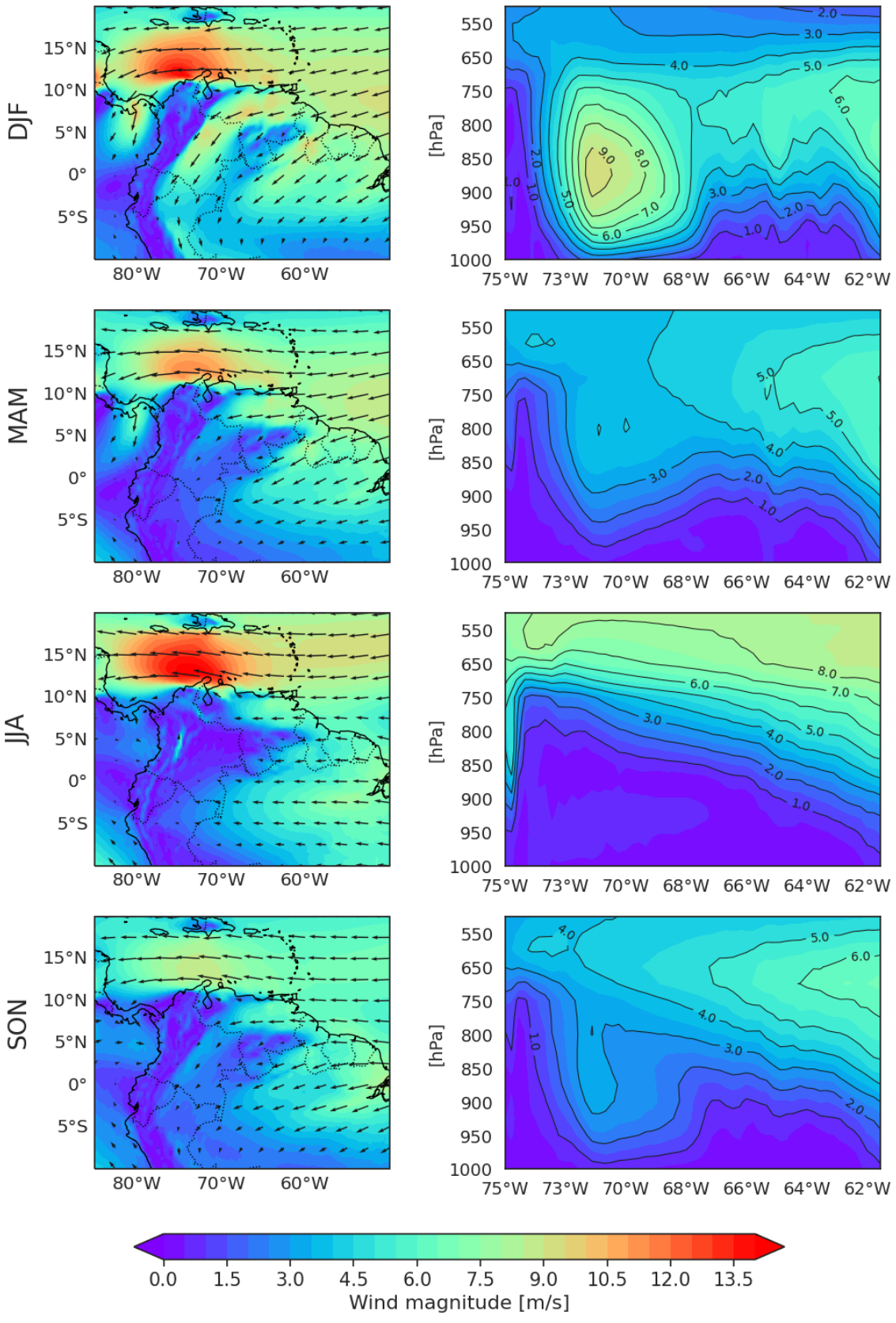

Figure 1.3: (Left) Climatology of the mean horizontal wind between 825 and 950 hPa in northern South America estimated from ERA5 data during 1979-2019. (Right) Vertical structure of the wind field at the exit of the jet (75°W-61°W, 3°N-5ºN).

occurs at 04:00 LT, in C2 at 07:00 LT, and in regions C3, C3.4 and C4 at 08:00 LT. This has been assessed in previous studies suggesting that at daily scale, the wind speed is not uniform in the Orinoco basin; on the contrary, it has an acceleration component that causes the difference in peak time in each region (Jiménez-Sánchez et al., 2019, 2020).

Even though we do not focus on the processes that may cause the acceleration of the low-level flow in the region (see Jiménez-Sánchez et al., 2020 for a discussion on this regard), we focus on the changes of the wind field throughout the day, which can be related to the influence of the PBL dynamics. Particularly, the PBL varies from a mixed layer in the daytime to a decoupled layer at nighttime due to its interaction with the land surface. Therefore, the conditions of the PBL modulate the strengthening and weakening of the OLLJ during the day (Martínez et al., 2022).

We evaluate the diurnal cycle of the sensible and latent heat fluxes, the zonal and meridional components of the surface turbulent stress, and the PBL dissipation. Sensible heat and latent heat refer to the energy required to increase temperature and induce a phase change, respectively. Surface turbulent stress refers to the stress at the surface given by its contact with the surrounding atmosphere. On the other hand, the PBL dissipation alludes to the kinetic energy that is being transformed into heat and thus can be used as a proxy of air movement and turbulence. All these quantities exhibit the variation of the PBL dynamics during the daytime, and they may contribute to its changes as they either enhance the temperature increase that allows the mixture of the air layer or cause movement of air masses that destabilize the PBL (e.g., Molod et al., 2019; Wang et al., 2021).

Figure 1.6 shows the diurnal cycle of these variables along the OLLJ corridor, showing marked changes throughout the day. A common characteristic is that the variables show minima values at nighttime while the opposite occurs during daytime when all variables tend to activate and reach their maximum, approximately at midday. The strengthening periods coincide with the diurnal variation of the solar radiation, so these quantities are influenced by the solar energy and contribute to a mixed PBL in which the wind field weakens. After sunset, as air temperature decreases,

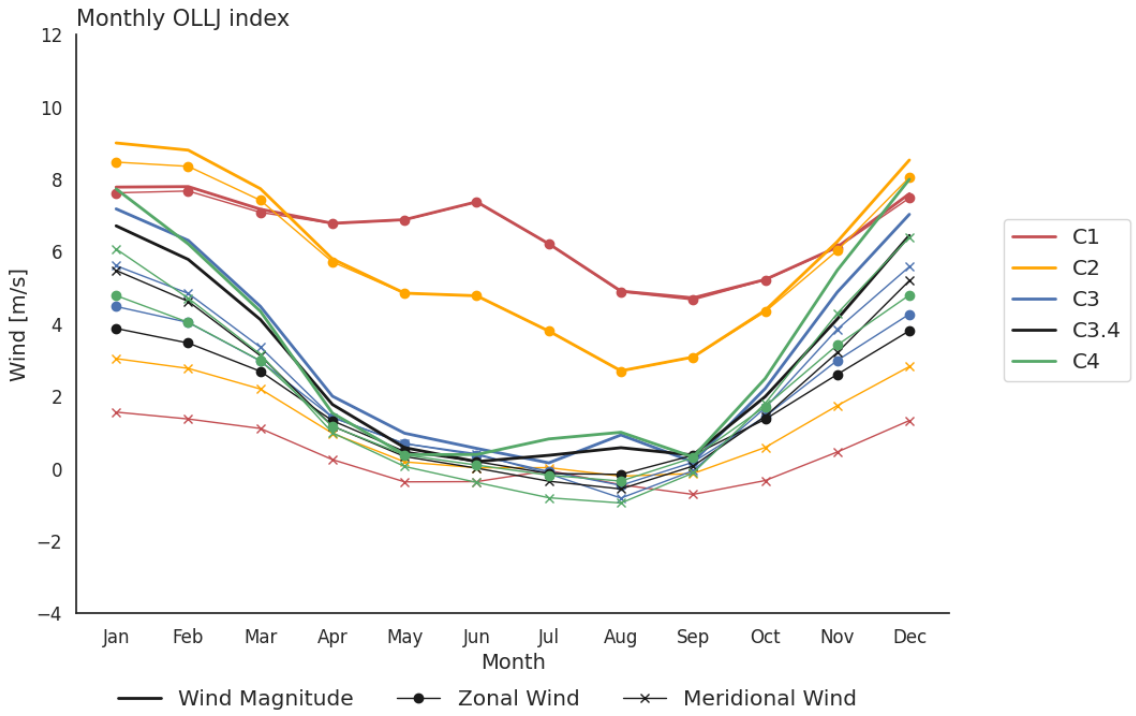

Figure 1.4: Annual cycle of the OLLJ index along the jet corridor. The index was computed in each subregion using the zonal wind (circles), meridional wind (x symbol), and wind magnitude (solid).

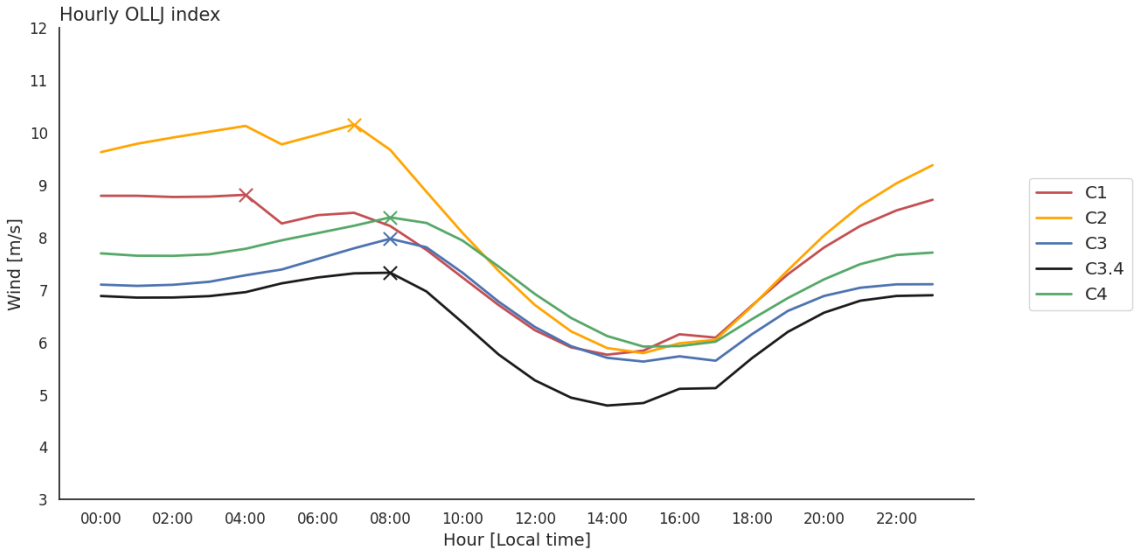

Figure 1.5: Diurnal cycle of the OLLJ index along the jet corridor estimated from ERA5 data during 1979-2019. The x symbol denotes the maximum value of the diurnal cycle.

the surface fluxes and the surface stress opposing the wind circulation also decrease, reducing mixing and turbulence, and allowing the PBL stratification. This leads to the strengthening of the LLJ during the night and early morning, and therefore the maximum wind speeds through the day are found at this time of the day.

In terms of the variations among the regions along the jet corridor, the main differences can be found between the entrance and exit regions (C1 and C4, respectively), given the contrasts between these regions. The OLLJ entrance is drier than the exit region, as the first one is located in the Orinoco basin and the latter is in the Andes-Amazon transition region. Therefore, precipitation, soil moisture patterns, and vegetation vary along the OLLJ corridor, resulting in differences in the surface fluxes and the dissipation of the PBL. Specifically, regions C1 and C2, which are located at the jet entrance, tend to reach higher values of sensible heat flux than latent heat flux due to the savanna land cover of the Orinoco basin (e.g., Martinez et al., 2022). In contrast, the exit region exhibits more humid conditions that enhance the latent heat flux from the surface. On the other hand, the PBL dissipation also experiences its peak approximately at midday; however in C1 and C2, at the entrance of the jet, the PBL dissipation exhibits higher values during nighttime, suggesting that the dissipation in the PBL can be enhanced by solar radiation, however it is also related to wind circulation as, in these regions, the eastward turbulent stress at nighttime still induces opposite drag to the wind field that may cause the turbulence associated to the PBL dissipation.

The turbulent surface stress differs from place to place mainly due to the prevailing direction of the flow along the wind corridor. In the entrance region, the jet is zonally oriented, thus the turbulent surface stress in the C1 and C2 regions are mainly opposed to the westward direction. In contrast, in the OLLJ exit, where the wind direction has relevant contributions from both components, the drag opposite to the flow develops in both directions, towards the east and the north.

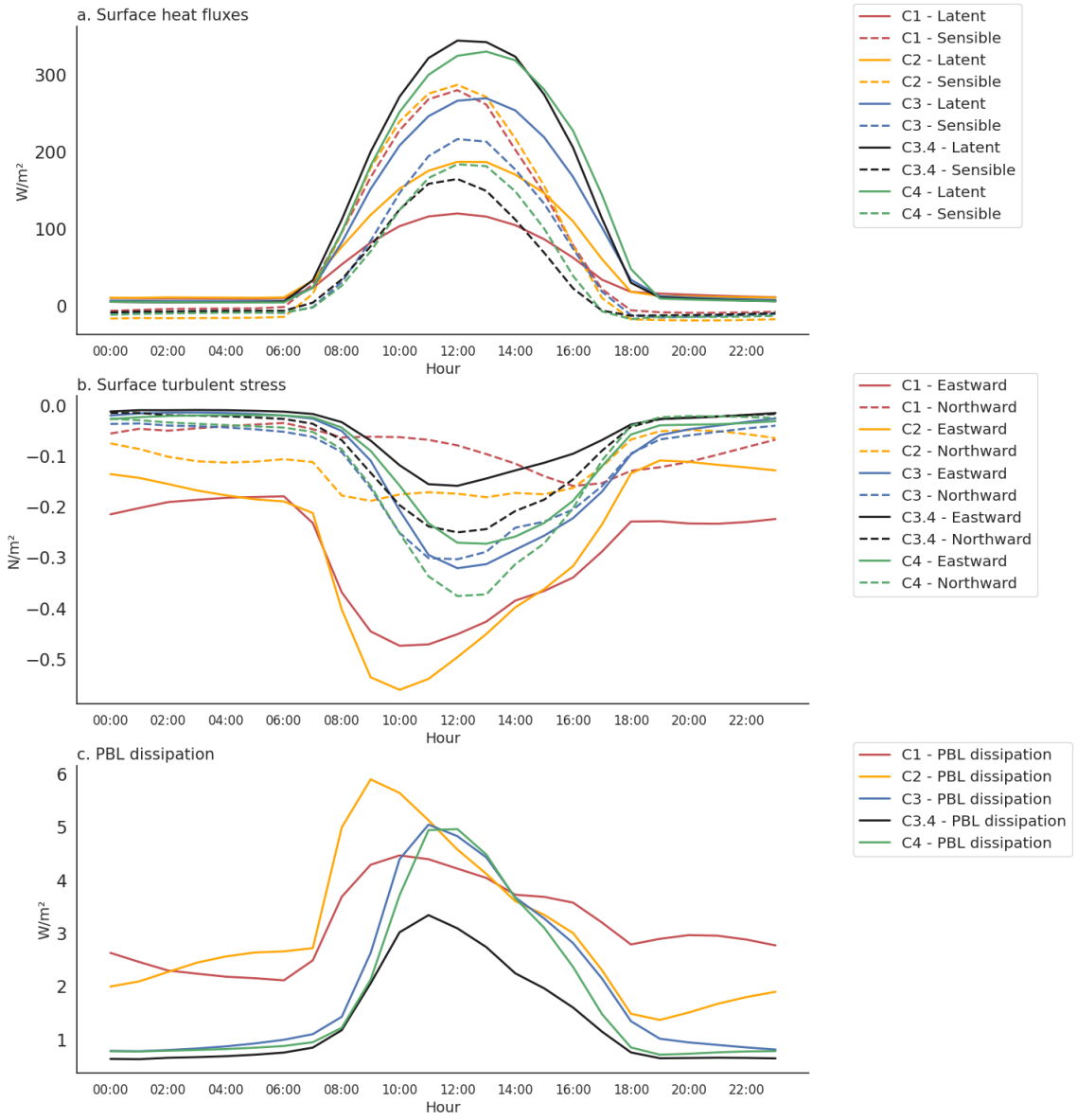

Figure 1.6: Diurnal cycle of a) mean latent and sensible heat fluxes, b) mean eastward and northward surface turbulent stress, and c) mean PBL dissipation along the OLLJ corridor estimated from ERA5 during 1979-2019.

1.3.4 The Orinoco low-level jet, atmospheric moisture transport and precipitation patterns in northern South America

As a LLJ relate to atmospheric moisture transport and precipitation patterns in its developing regions, we perform an analysis based on the monthly series of the OLLJ index, as well as VIMF, precipitation, and VIMD at each grid point in northern South America, to assess the spatial patterns of these variables and their relationship with the OLLJ.

We estimate the VIMF between 1000 hPa and 800 hPa over northern South America using equation 1.1 and its seasonal spatial distribution is presented in Figure 1.7. During DJF, which corresponds to the activation period of the OLLJ, the atmospheric moisture flux through the Orinoco basin surpasses 180 kg/ms. In contrast, during the other seasons, the flux weakens, suggesting the influence of the OLLJ on the moisture flux into the basin. It can be observed that over the Venezuelan Llanos, near the coastal line, the VIMF exhibits values over 140 kg/ms in all seasons, indicating that the wind circulation in the Caribbean Sea and Tropical North Atlantic influence the atmospheric moisture patterns in the Venezuelan Llanos throughout the year. However, as this flux extends towards the south only in DJF, the activation of the OLLJ may modulate the atmospheric moisture flux to the Colombian Llanos and northern Amazon. Therefore, the OLLJ can be identified as a relevant moisture flux mechanism in northern South America, as stated in previous studies (Builes-Jaramillo et al. 2022a; Martinez et al. 2022).

To confirm the above, we perform a simple linear regression between the OLLJ index along the jet corridor and the series of VIMF at each grid cell in northern South America. Figure 1.8 shows the spatial distribution of the location where the OLLJ affects the 950-825 hPa VIMF (where the linear regression is statistically significant with an alpha of 0.05). We estimate a simple linear regression with the OLLJ index in the five different regions along the jet corridor (Figure 1.1) to assess the existence of

possible differences in the effects of the OLLJ over the spatial patterns of atmospheric moisture flux in northern South America.

At first, the spatial effects of the OLLJ on VIMF over northern South America varies according to the region in which the OLLJ index is estimated. The OLLJ in region C1 has a more significant effect on the VIMF in the Venezuelan Llanos, northern Colombia, and some regions in the Los Andes mountain range. As the jet reaches a southernmost location, its influence in the atmospheric moisture flux extends over the Orinoco basin and northern Amazon. In C2, the region where VIMF can be influenced by the OLLJ extends to some parts of the Colombian Llanos and northern Peru, while regions C3, C3.4, and C4 exhibit similar effects as the OLLJ index computed over these regions influences the VIMF through the jet corridor and the northern Amazon.

According to the linear regression analysis, the role of the OLLJ in the VIMF over northern South America is more significant at its exit region, as the VIMF in northern Amazon, Los Llanos, and some areas in the Magdalena-Cauca basin in Colombia can be influenced by the fluctuations of the OLLJ activity. This pattern is similar when considering the VIMF at lower levels (between 1000 and 925 hPa, Figure S1.1), reaffirming that the effect of the OLLJ on the atmospheric moisture patterns in northern South America is not spatially uniform. On the contrary, it depends on the location considered along the jet corridor. The sign of the slope of the linear regression indicates that higher values of the OLLJ index potentiate the VIMF through Los Llanos and northern Amazon (red shading), while, depending on the region in the jet corridor, higher values of the index produce lower VIMF (blue shading) in western Colombia (C1 and C2, Figure 1.8a, b), and the Andes mountain range and northern Brazil (C3, C3.4, and C4, 1.8c, d, e).

When evaluating the lagged correlations between the anomalies of the OLLJ index for each region and the VIMD anomalies for each grid point, similar differences are observed (Figure 1.9). In Figure 1.9, the dots represent the lag of the highest correlations. Thus, thicker dots suggest a lag of up to six months between the jet activity and VIMD, while no dots in the grid cell suggests a simultaneous relationship

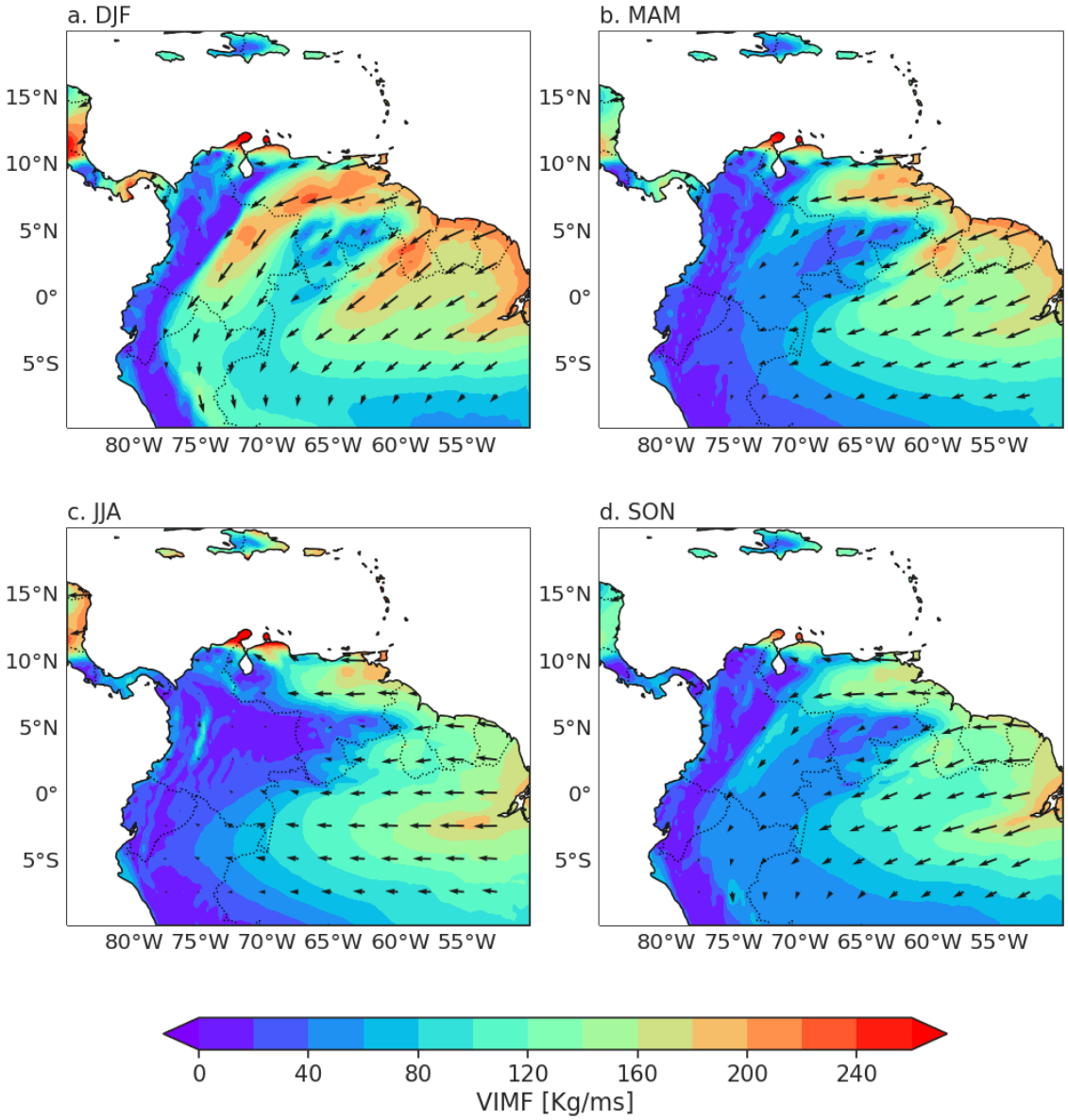

Figure 1.7: Climatology of the seasonal Vertically Integrated Moisture Flux (VIMF) for the atmospheric column between 1000 hPa and 800 hPa in northern South America, estimated from ERA5 during 1979-2019: a) DJF, b) MAM, c) JJA, and d) SON.

(lag zero). At the entrance of the jet, in regions C1 and C2 (Figure 1.9a, b), a strengthening in the OLLJ is accompanied by atmospheric moisture divergence in the Venezuelan Llanos and atmospheric moisture convergence in the Colombian Llanos and northern Amazon. As there are no dots in much of the region, it suggests that a change in the jet activity is associated with a simultaneous change in the divergence and convergence patterns. These results are consistent with previous studies evaluating the spatial patterns of atmospheric moisture divergence through a composite analysis on specific days of the occurrence of the OLLJ (Builes-Jaramillo et al. 2022a). On the other hand, the exit regions (C3, C3.4, and C4, Figure 1.9c, d, e) exhibit a contrasting pattern, with a positive correlation along the Colombian Llanos and northwestern Amazon. The above indicates that the strengthening of the OLLJ in these locations is accompanied by the occurrence of simultaneous atmospheric moisture divergence. These patterns exhibit statistically significant relationships across most of the spatial domain, regardless of the region where the OLLJ index was computed (Figure S1.2). However, the lagged correlations reduce their statistical significance in central and western Colombia when considering the index in the exit regions (C3, C3.4 and C.4), which suggests that the effect of the OLLJ on the VIMD patterns is particularly robust along the OLLJ corridor and northern Amazon.

Regarding the relationship between the OLLJ and precipitation in northern South America, Figure 1.10 shows the lagged correlations between the anomalies of the OLLJ index in each region and the anomalies of precipitation at each grid cell. Positive correlations indicate that a stronger jet is associated with higher precipitation, while negative correlations represent an inverse relationship. The highest correlations are obtained with the C1 and C2 indices, suggesting that a stronger OLLJ in the entrance regions favors precipitation in the Colombian Llanos and the Amazon region. On the contrary, the OLLJ in the C3, C3.4, and C4 (exit) regions is more related to less precipitation in the Colombian Llanos and northwestern Amazon, although it seems to be accompanied by increases in precipitation over Los Andes.

The lags in the correlation between the OLLJ index and precipitation reaffirm differences in the effect of the jet on regional precipitation patterns. At the entrance region (Figure 1.10a, b), the OLLJ has positive simultaneous correlations in the

Amazon region, suggesting a more direct relationship between the strengthening of the surface flow and increases in precipitation. At the jet exit (Figure 1.10c, d, e), its strengthening is accompanied by simultaneously reduced precipitation in the Colombian Llanos and the northwestern Amazon. On the other hand, lags up to six months can be found in the relation between the two quantities over some regions. For instance, a more intense jet in regions C3, C3.4, and C4 may be related to higher precipitation in the Colombian Andes and northern Brazil, with a lag between two and three months. Regarding the significance of the lagged correlations (Figure S1.3), the pattern is similar to that obtained for the VIMD since, at the exit region, the correlation between the OLLJ and precipitation anomalies are statistically significant throughout the Orinoco basin, northern Amazon and western Colombia. However, in the jet exit region, significance is found in the jet corridor and northern Amazon, but is not widely distributed west of the Andes Mountain range, which supports that the OLLJ can modulate regional characteristics of precipitation and humidity divergence, but its effect changes according to a specific region of the jet.

1.3.5 Regional gradients of mean sea level pressure, near-surface air temperature and surface sensible heat flux

Martinez et al. (2022) suggest that surface fluxes influence the pressure gradients between the northern Orinoco and the Andes-Amazon transition. Hence, we evaluated the influence of these regional gradients in the strengthening and weakening of the flow associated with the OLLJ. Figure 1.11 presents the climatological fields of the SSHF and MSLP for DJF, which shows that the Venezuelan Llanos exhibits higher values of MSLP during this season. On the contrary, the transition region, located at the jet exit, exhibits lower pressure values on the surface during DJF. On the other hand, the SSHF over the Orinoco region is higher than over the transition zone, which is strongly influenced by the hydroclimatological characteristics of each area: the Llanos are characterized by drier conditions where the typical vegetation is grassland, while on the contrary, the Andes-Amazon transition zone has a more humid regime characterized by higher amounts of precipitation and soil moisture

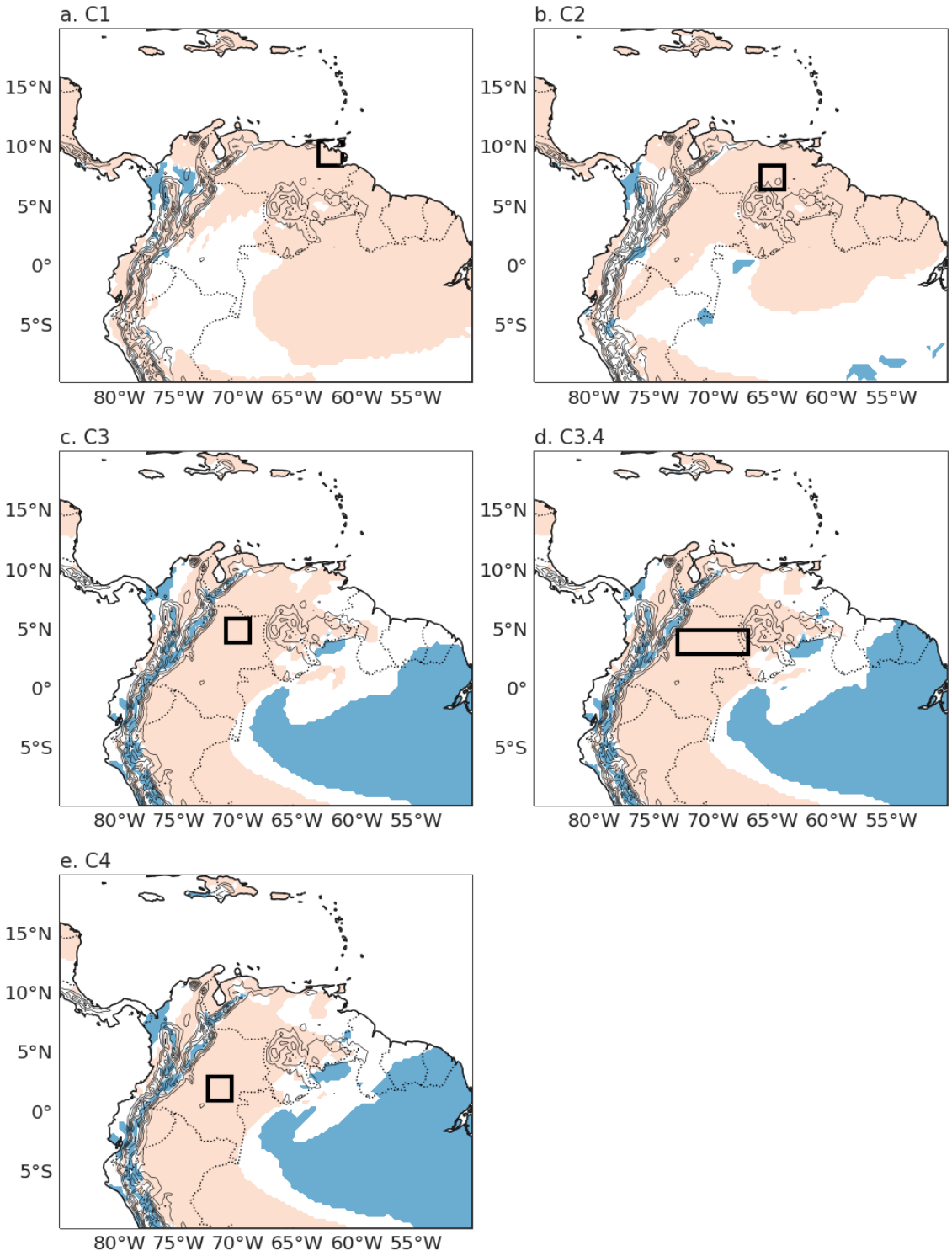

Figure 1.8: Linear regression between the 950-825 hPa VIMF series at each grid cell and the OLLJ index estimated using ERA5 data during 1979-2019. Shading indicates the grid cells in which the simple linear regression was statistically significant (p-value < 0.05). Black rectangles represent the region of calculation of the OLLJ index: a) C1, b) C2, c) C3, d) C3.4, and e) C4. Red shading indicates grid cells in which the slope of the regression is positive, while blue shading indicates grid cells with negative linear regression slope.

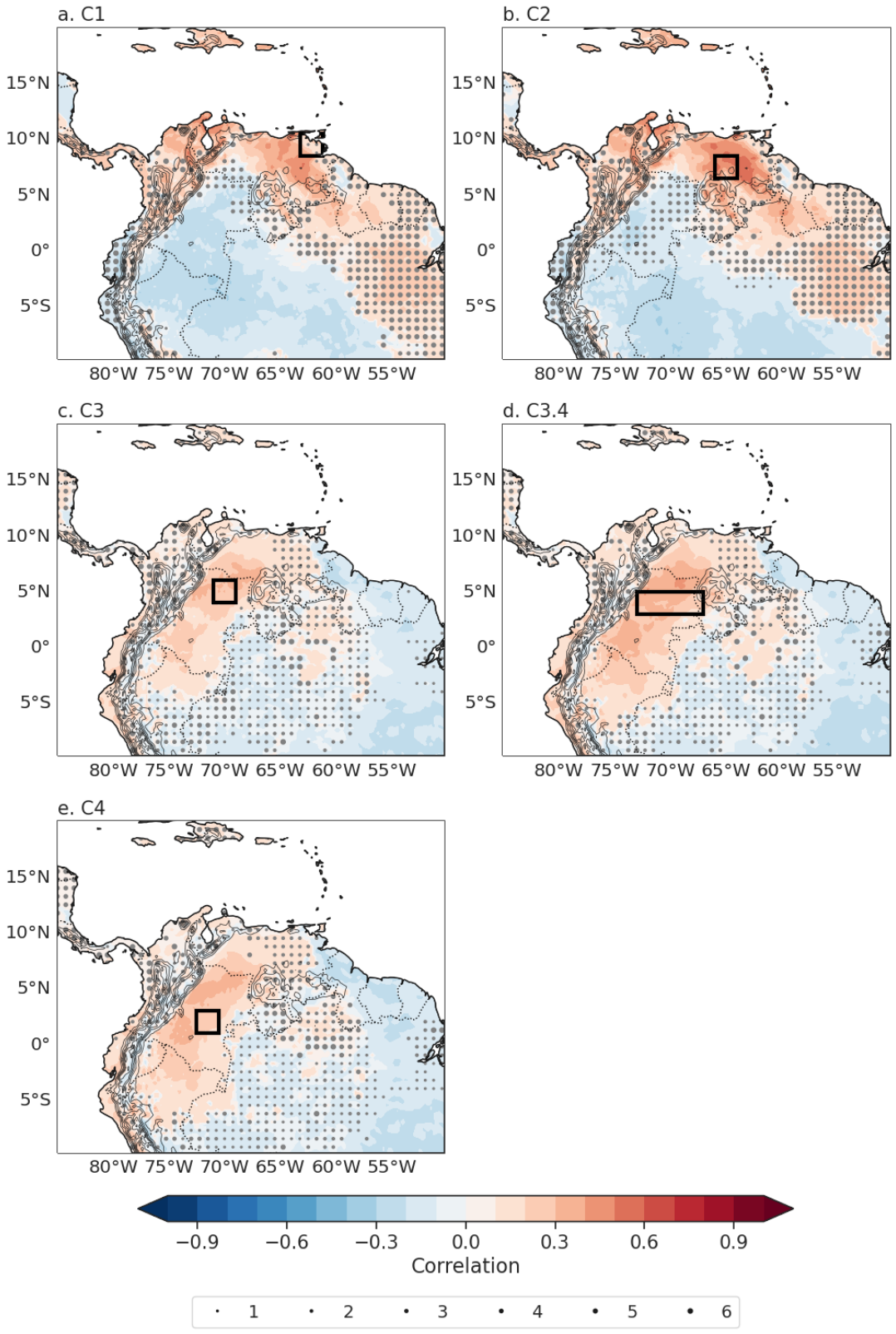

Figure 1.9: Maximum lagged correlation between the anomalies of the OLLJ and the VIMD at each grid point in northern South America estimated from ERA5 data during 1979-2019. Dots represent the lag (in months) of the maximum correlation between the OLLJ index and the VIMD. Black rectangles represent the region of the calculation of the OLLJ index.

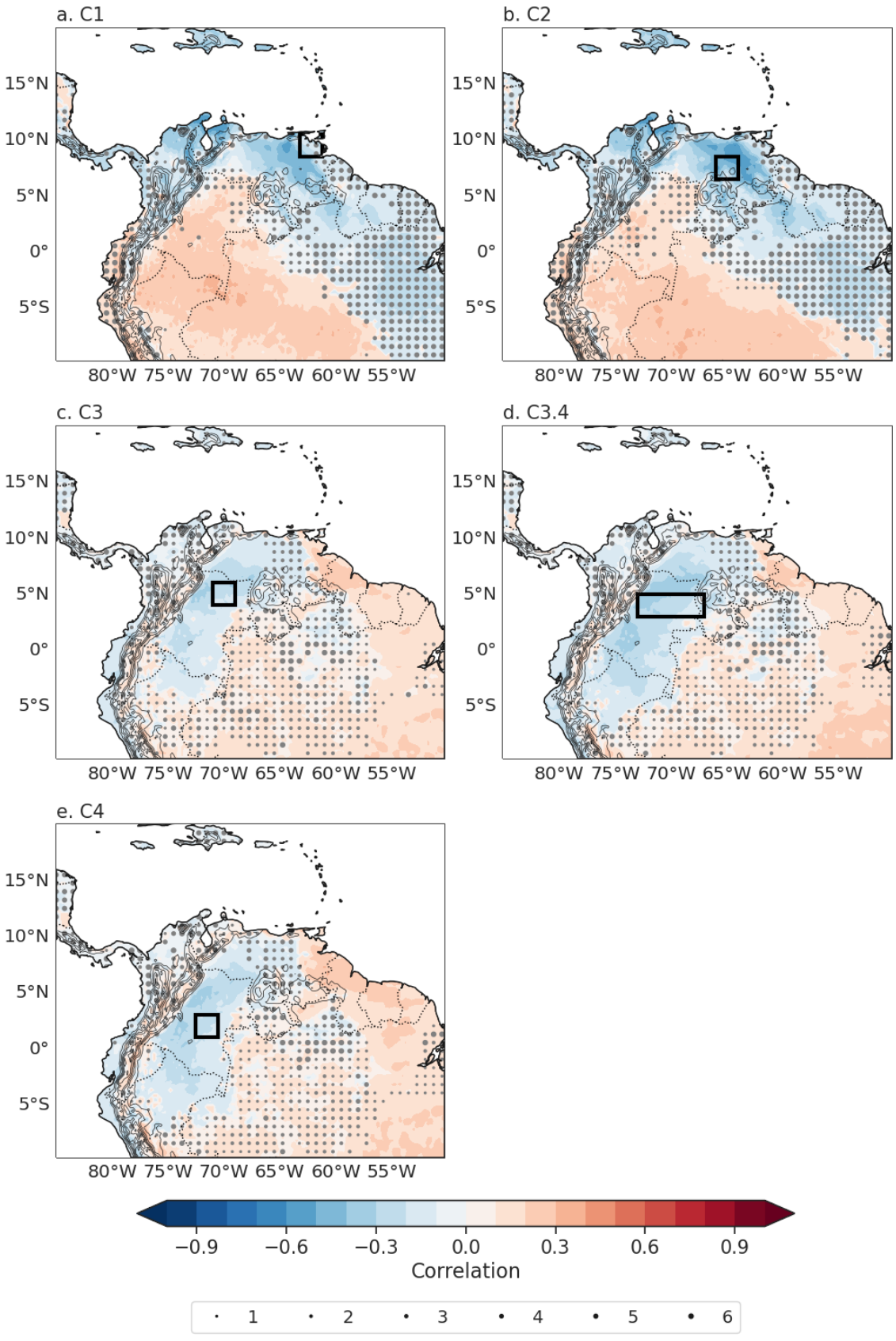

Figure 1.10: As in Figure 1.9 but for precipitation anomalies.

(e.g., San José et al., 1998; Arias et al., 2020; Espinoza et al., 2020; Martínez et al., 2022).

The spatial pattern of MSLP is consistent with the activation of the OLLJ during DJF, since the wind flows from higher to lower pressures. However, an enhanced pressure gradient occurs when the northern region, associated with higher surface pressure, exhibits higher values of SSHF. To assess this relationship, Figure 1.11 also presents the monthly variation of the MSLP and SSHF gradients, calculated as the difference between the spatial average of the variables in the Orinoco region and the Andes-Amazon transition region (red and blue rectangles in Figure 1.11, respectively). Our findings suggest that the Orinoco region exhibits higher SSHF values throughout the year than those in the Andes-Amazon transition region, and the MSLP gradient shows marked variations during the year. Specifically, the gradients strengthen in DJF, and the activation of the OLLJ is accompanied by higher contrasts of MSLP and SSHF between the northern zone of the jet corridor and its southernmost region. As assessed in previous works, the MSLP gradients between the NASH and the lower surface pressures associated with the southernmost location of the Intertropical Convergence Zone (ITCZ) allow the strengthening of the northeasterly trade winds and, therefore the activation of the OLLJ (Jiménez-Sánchez et al., 2019; Jones, 2019; Builes-Jaramillo et al., 2022b). On the other hand, the influence of the regional SSHF gradient was previously suggested by Martinez et al. (2022), as they found that the simulation of lower (higher) SSHF values in the Orinoco, which lead to the decrease (increase) in the near-surface air temperature in the region, could increase (decrease) the MSLP gradient between the Orinoco and the Andes-Amazon transition region and therefore modulate the strengthening (weakening) of the OLLJ.

Based on these findings, we evaluate the regional patterns of the MSLP and SSHF gradients during strong and weak OLLJ events. We focus on the period DJF. Also, from the anomalies of the monthly long-term series of the OLLJ index at region C4, we selected the years of strong and weak OLLJ as those when the wind magnitude in DJF is above or below one standard deviation, respectively. We consider the OLLJ index at region C4 because this region corresponds to the southernmost

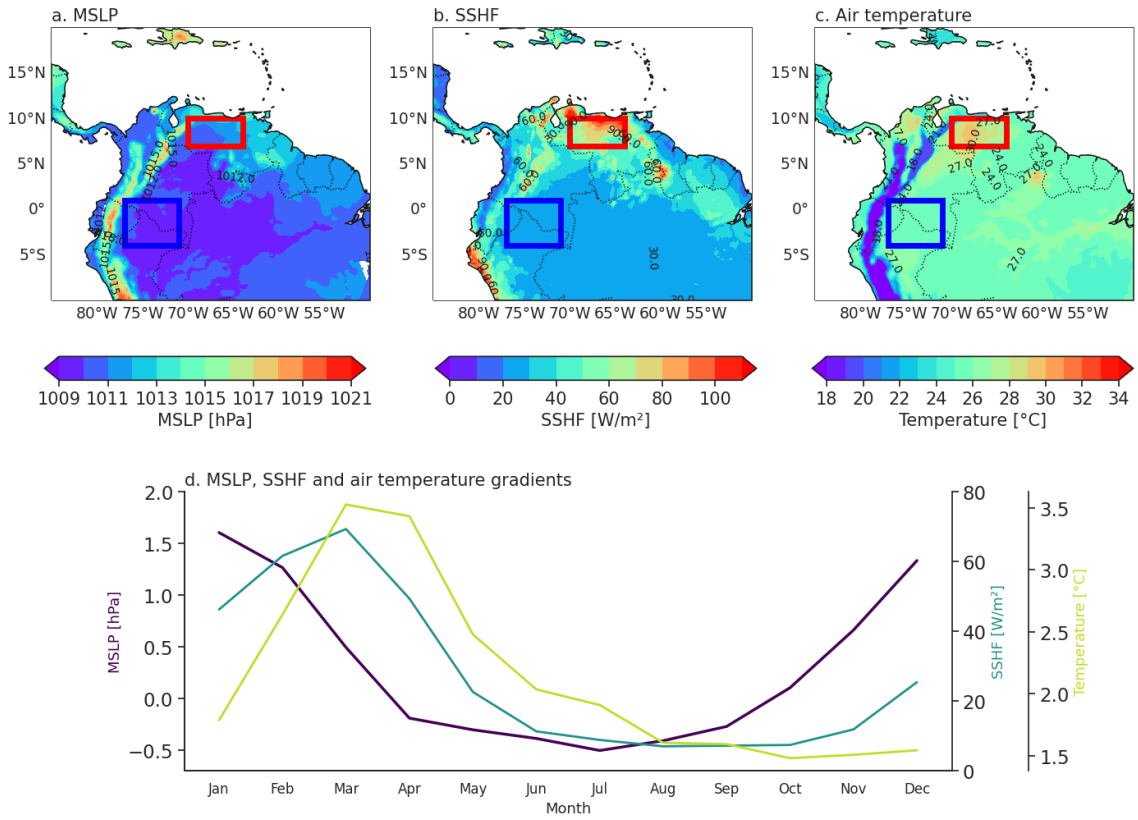

Figure 1.11: Climatology of the a) mean sea level pressure (MSLP), b) surface sensible heat flux (SSHF) and c) near-surface air temperature for DJF estimated from ERA5 data during 1979-2019. d) Annual cycle of the gradients of MSLP (purple line), SSHF (blue line) and air temperature (green line) between the Orinoco (red rectangle in a)) and the Andes-Amazon transition (blue rectangle in a)) regions.

extension of the jet (jet exit), so higher and lower wind magnitudes during DJF can be directly related to changes in the OLLJ intensity. Table 1.2 shows the years with the occurrence of strong and weak OLLJ events. In general, strong (weak) OLLJ events occurred during La Niña (El Niño) (years highlighted in colored bold), as also suggested by Builes-Jaramillo et al. (2022b). On the other hand, after analyzing the probability density function (PDF) of the wind speed during the occurrence of strong, weak and normal OLLJ events, the results suggest marked changes in the PDFs: during strong events the wind speeds tend to exhibit higher values, and during weak events, the PDF shifts to the left and encompasses lower wind speeds (Figure S1.4). Furthermore, the Kolmogorov-Smirnov test suggests a statistical difference of the wind speeds that occur during strong, weak, and normal OLLJ events.

Table 1.2: Years of occurrence of strong and weak OLLJ events during DJF according to ERA5 data during 1979-2019. Bold red years represent OLLJ events under El Niño conditions while bold blue years represent OLLJ events under La Niña conditions.

Strong OLLJ events	**Weak OLLJ events**
1984	**1982**
1988	**1986**
1989	**1997**
1999	**2002**
2007	**2009**
2008	**2015**
2011	

The above suggests that the interannual strengthening of the OLLJ is strongly influenced by the warm and cold phases of ENSO. Regarding the SSTs patterns in the periods of different intensities of the OLLJ, Figure 1.12 presents the composites of SST anomalies during strong (Figure 1.12a) and weak (Figure 1.12b) jet events during DJF. The results suggest that during strong OLLJ events, negative SST anomalies occur in the tropical Pacific and Atlantic oceans, even though the anomalies in the Pacific Ocean are stronger. On the other hand, an opposite pattern is found during weak OLLJ years, with high positive SST anomalies in eastern and central tropical Pacific, and with lower positive anomalies through the Caribbean Sea and the tropical north Atlantic. These spatial patterns of SST reinforce the link between the occurrence of El Niño and La Niña conditions and variations on the strength of the OLJJ. The patterns in the Atlantic Ocean suggest lower anomaly values but

similar to the patterns in the Pacific Ocean. Strong (weak) OLLJ events are accompanied by negative (positive) SST anomalies in the tropical Atlantic and the Caribbean Sea, which may influence the regional gradients of sea level pressure and therefore the intensity of the jet.

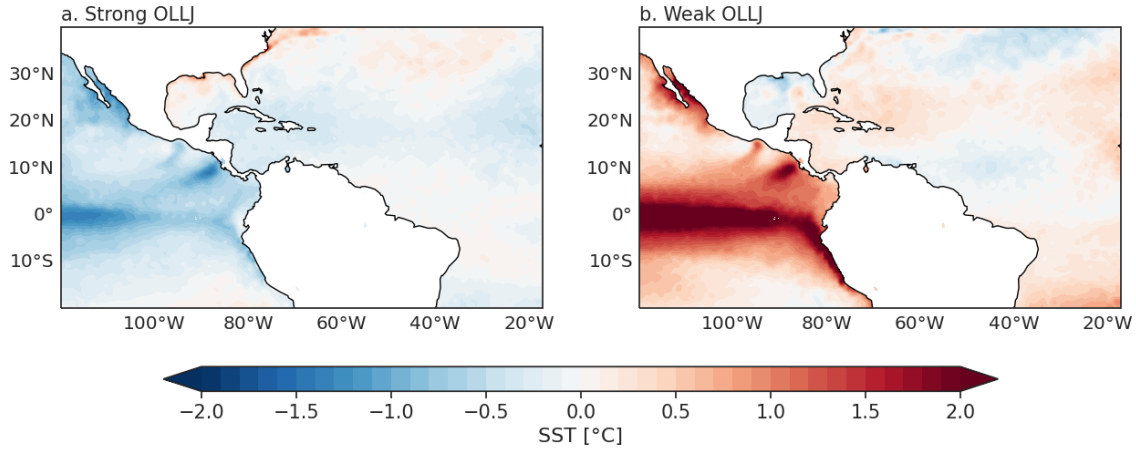

Figure 1.12: Composites of the anomalies of SSTs during a) strong and b) weak OLLJ events using ERA5 data during 1979-2019. The strong and weak OLLJ events used are shown in Table 1.2.

Figure 1.13 shows the series of anomalies of the OLLJ index for DJF and the gradients of MSLP and SSHF between the Orinoco (red rectangle in Figure 1.11) and the Andes-Amazon transition (blue rectangle in Figure 1.11) regions during 1979-2019. Additionally, the bottom panel shows the near-surface temperature gradients in order to relate changes of the SSHF and MSLP gradients to changes in surface air temperature. The red (blue) lines correspond to the events of strong (weak) OLLJ events in DJF, as indicated in Table 1.2. A stronger OLLJ tends to be accompanied by stronger MSLP and weaker SSHF gradients between the Orinoco and the Andes-Amazon transition region. On the contrary, a weaker OLLJ is accompanied by a weaker MSLP and a stronger SSHF gradient between these two regions. This can be explained since a higher SSHF in the Orinoco region is related to an increase in near-surface air temperature that decreases the MSLP in the region. This leads to the decrease in MSLP differences between the Orinoco and the Andes-Amazon transition region, and finally, a weakening of the flow associated with the OLLJ. The contrary occurs during strong OLLJ events: lower SSHF over the Orinoco relates to decreased air temperature in the region, increasing the MSLP locally and strength-

ening the MSLP gradient between the Orinoco and the Andes-Amazon transition region, therefore, allowing the intensification of the OLLJ. Computing the OLLJ index for region C3.4 leads to similar patterns of MSLP, SSFH and near-surface air temperature during strong or weak OLLJ events (Figure S1.5).

These results are consistent with Martinez et al. (2022) and confirm that although the meridional pressure gradients between the Tropical North Atlantic and the Andes-Amazon transition are relevant to the development of the OLLJ, other regional aspects like the surface fluxes between the northern and southern zones of the OLLJ corridor affect the MSLP conditions in those regions, influencing the OLLJ strength during its activation period. It is relevant to notice that although the patterns of the gradients of MSLP, SSHF and air temperature tend to be distinctive depending on the intensity of the OLLJ, they are not always similar in all the selected events. One example is 1982, when a strong El Niño ocurred and a weak OLLJ event is identified, but the patterns of decreasing MSLP and increasing air temperature and SSHF gradients are not very clear. Similarly, not all the changes in these gradients are related to a change in the OLLJ intensity. This suggests that gradients between the northern and southern regions of the OLLJ corridor influence the strengthening of the surface wind field but may not be the only elements to consider in order to evaluate a change in the intensity of the OLLJ, for which further studies are needed.

1.4 Conclusions

The OLLJ is an important feature of the climate in northern South America as it modulates atmospheric moisture flux along the Orinoco basin towards the Andes-Amazon transition region and the Amazon. The results of this chapter are consistent with previous studies focused on the analysis of the main spatial and temporal features of the OLLJ, as well as its connection with other regional processes. For the first diagnostics of the mean annual and diurnal behavior of the OLLJ, we used the ERA5 reanalysis and compared it with in situ radiosonde data. The reanalysis ERA5 exhibits some differences compared to the observations of the vertical wind

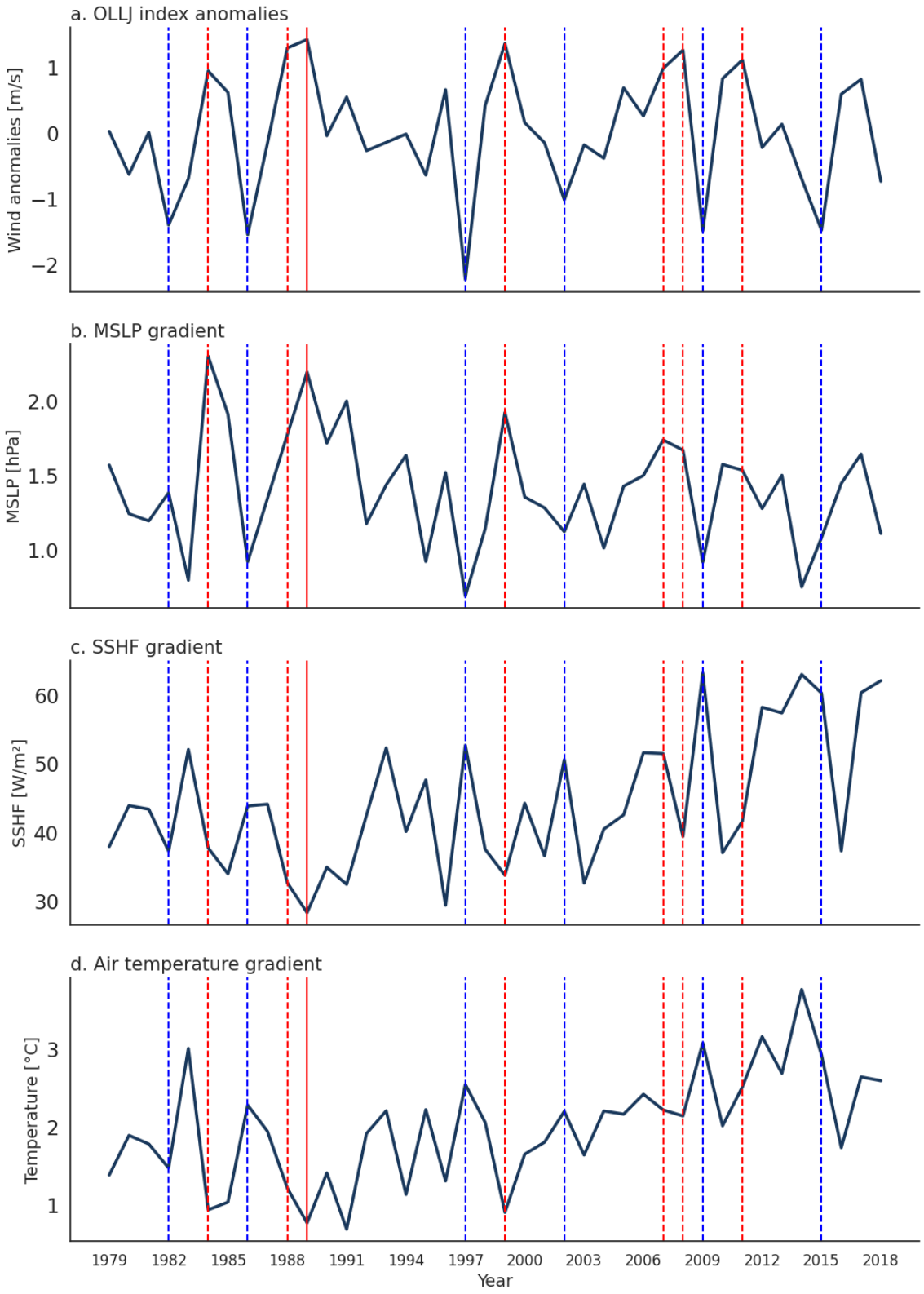

Figure 1.13: a) Anomalies of the OLLJ index at region C4 for DJF using ERA5 data during 1979-2019. Gradients of b) MSLP, c) SSHF and d) near-surface temperature between the Orinoco and the Andes-Amazon transition region. Red vertical lines indicate years with the occurrence of a strong OLLJ in DJF. Blue lines represent the years of the occurrence of a weak OLLJ. Dashed lines indicate the occurrence of El Niño (blue) and La Niña (red) events.

structure in Los Llanos, as it exhibits an overestimation of the wind magnitude at lower levels during daytime and nighttime (Figure 1.2). However, these differences are expected given the characteristics of each database. Despite those differences, it is worth noting that ERA5 represents the strengthening of the wind field during DJF and the contrast in the vertical wind structure in daytime and nighttime. Therefore, this reanalysis captures the main features of the OLLJ.

The OLLJ develops below 800 hPa over the Orinoco basin, in northern South America, during DJF, and reaches its minimum intensity during JJA (Figure 1.3). The seasonal activation of the jet occurs as a result of the pressure gradients between the NASH and the low surface pressures of the ITCZ, indicating that a stronger MSLP gradient between the NASH and the Orinoco is associated with a stronger OLLJ, as also identified by other studies (Builes-Jaramillo et al., 2022b; Martínez et al., 2022). However, some regional processes can have a relevant effect on the interannual intensity of the jet. Specifically, the differences in MSLP and SSHF between the northern and the southern regions of the jet corridor showed a link with the occurrence of strong and weak OLLJ events, as variations in these gradients influence the wind flow associated with the jet. As indicated in previous studies (Martinez et al., 2022), a stronger OLLJ tends to be accompanied by decreasing SSHF in the Orinoco region which allows higher MSLP over this region, enhancing the regional pressure gradients (Figure 1.13). An opposite relationship occurs when the jet is weaker.

Generally, the core of the OLLJ can be found between 825 and 950 hPa. However, this can vary throughout the year because of the friction effect of the land surface over the low-level wind field. Related to its diurnal variation, the jet reaches its maximum strengthening in the early morning, from 04:00 LT, near the coastal line in Venezuela, until 08:00 local time at its exit region (see Figure 1.5). These contrasts in the wind speed during daytime and nighttime are likely to occur because of the diurnal dynamics of the PBL. A mixed layer weakens the surface wind field during the day while a stratified layer enhances the low-level wind circulation during the night in the region. The variations in the PBL occur because of its interaction with the land surface, in which heat fluxes from the surface are enhanced by solar radiation,

and the stresses and air movements induced by the surface roughness influence the state of this layer, therefore, the intensity of the jet through the day.

Finally, regarding the relationship of the OLLJ with atmospheric moisture flux and precipitation in northern South America, our results suggest that the OLLJ has a relevant role in the moisture flux along the Orinoco basin; however, its effects differ when considering the jet intensity at its entrance or exit regions (section 1.3.4). At its entrance, the OLLJ favors atmospheric moisture flux in the Venezuelan Llanos and positively correlates with moisture convergence and increases in precipitation in the Colombian Llanos and northern Amazon during DJF. On the other hand, the OLLJ enhances the moisture flux along the Orinoco basin at its exit region and therefore it is positively related to moisture divergence and decreases in precipitation in the Colombian Llanos and northwestern Amazon during DJF. In addition, as seen in Figures 1.9 and 1.10, the strengthening of the OLLJ may be accompanied by atmospheric moisture convergence and increasing precipitation in the Colombian Andes and northern Brazil. However, this relationship can exhibit a lagged response between changes in the OLLJ strength and changes in atmospheric moisture and precipitation patterns.

1.5 Supplementary material

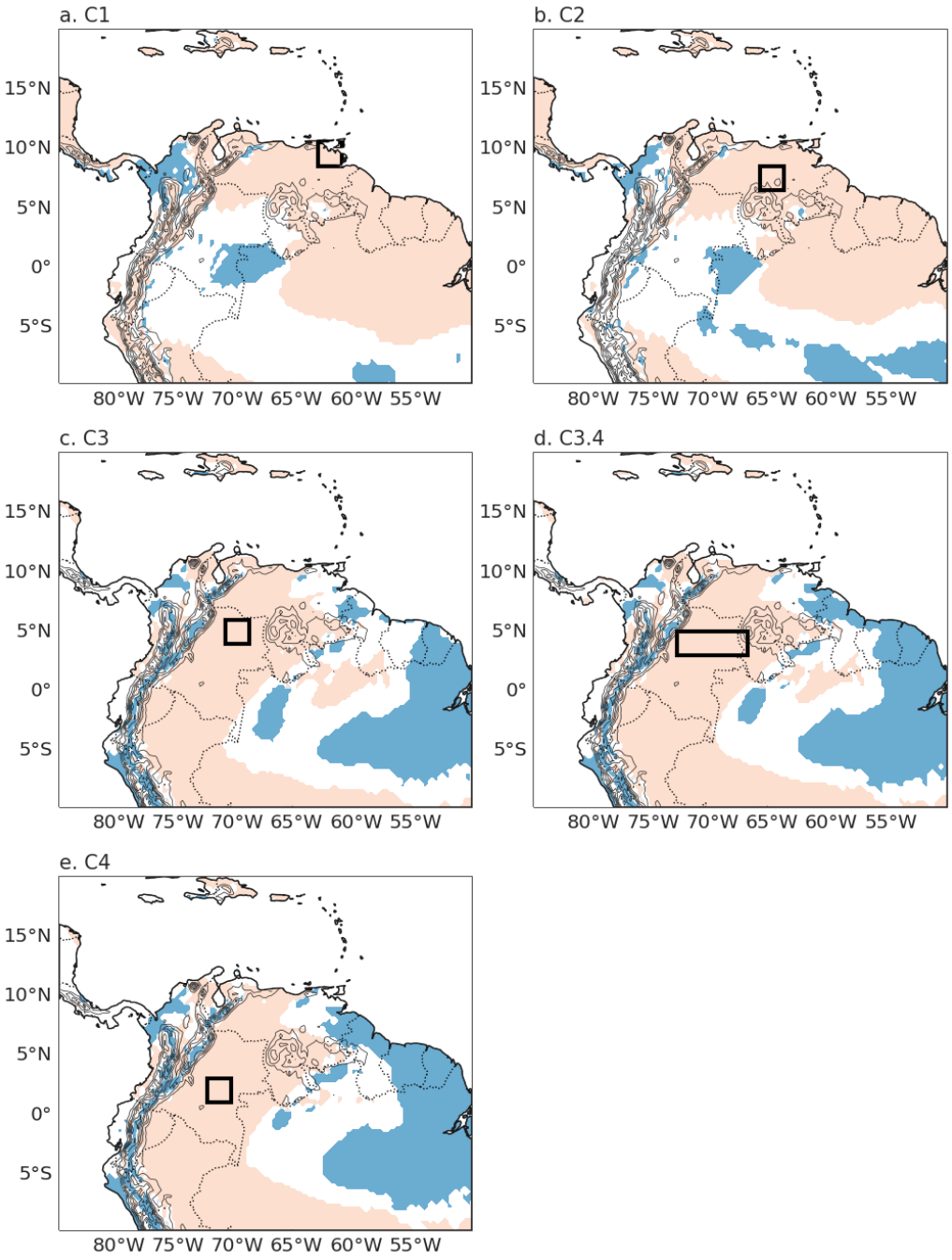

Figure S1.1: Linear regression between the 1000-925 hPa VIMF series at each grid and the OLLJ index using ERA5 data during 1979-2019. Shading indicates the grid cells in which the simple linear regression was statistically significant (p-value < 0.05). Black rectangles represent the region of calculation of the OLLJ index: a) C1, b) C2, c) C3, d) C3.4, and e) C4. Red shading indicates grid cells in which the slope of the regression is positive, while blue shading indicates grid cells with negative linear regression slope.

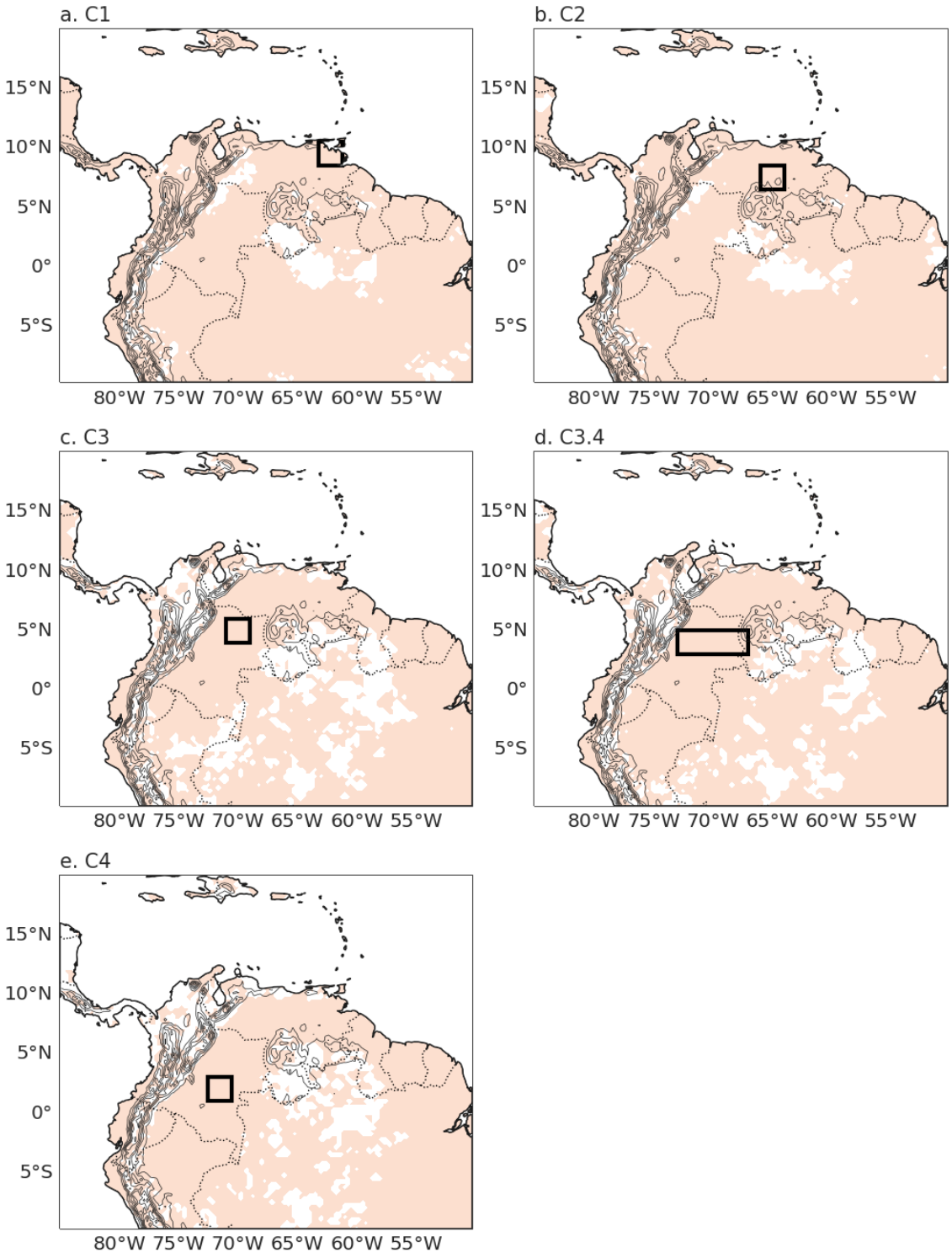

Figure S1.2: Statistical significance of the maximum lagged correlation between the OLLJ and VIMD anomalies at each grid point in northern South America considering an alpha of 0.05. Black rectangles represent the region of the calculation of the OLLJ index.

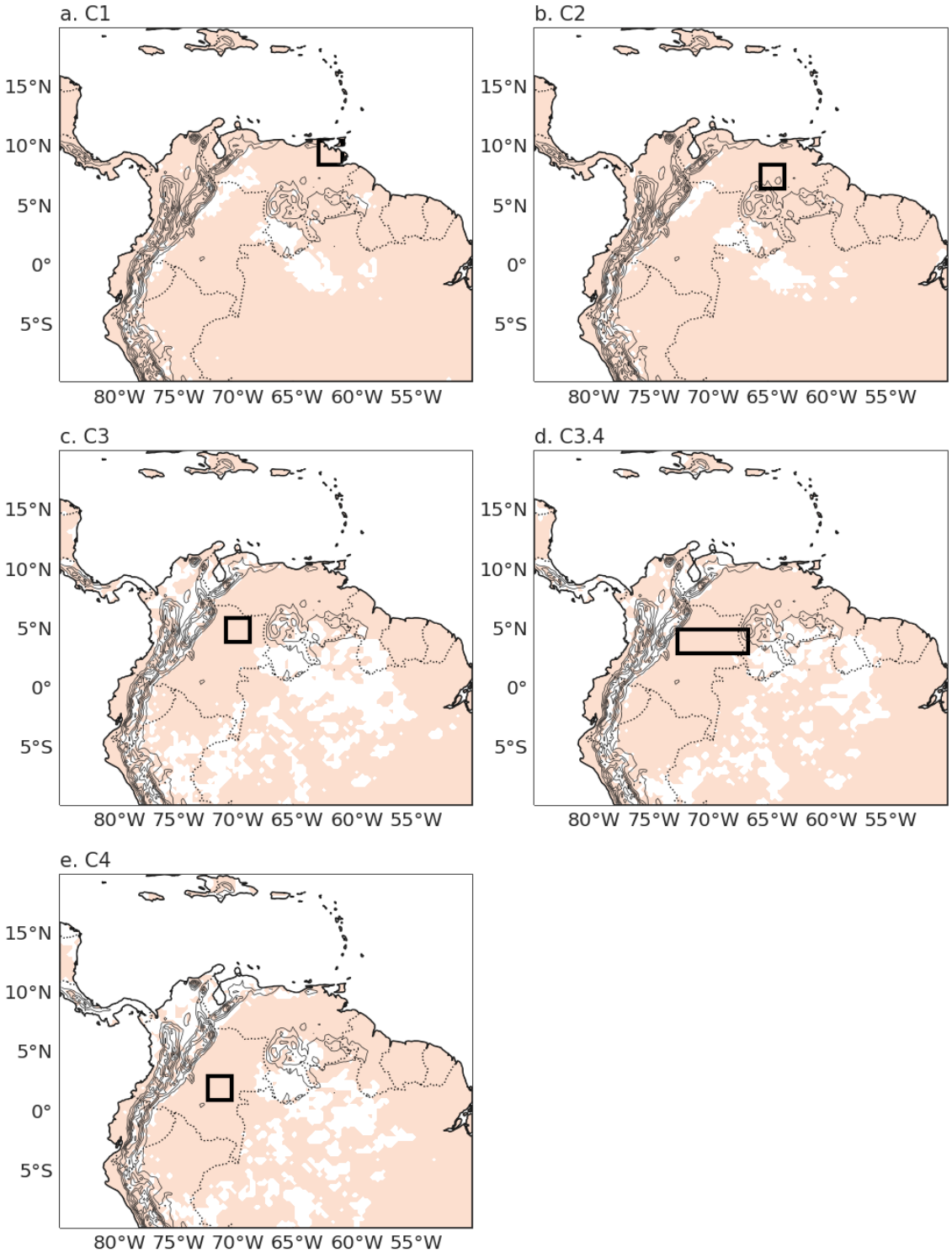

Figure S1.3: Statistical significance of the maximum lagged correlation between the OLLJ and precipitation anomalies at each grid point in northern South America considering an alpha of 0.05. Black rectangles represent the region of the calculation of the OLLJ index.

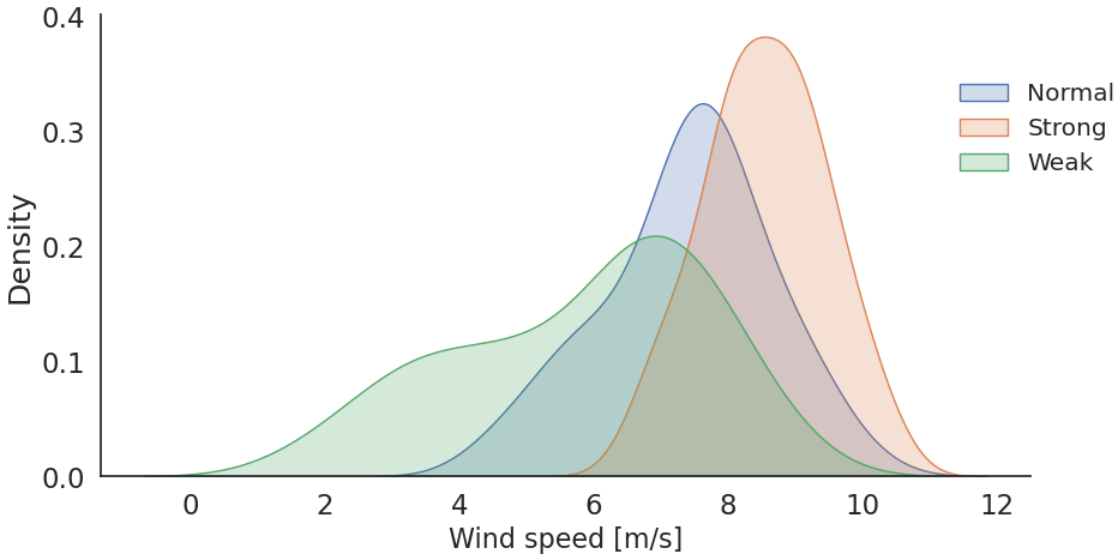

Figure S1.4: Probability density function of the monthly wind speeds in DJF during weak, strong and normal OLLJ events.

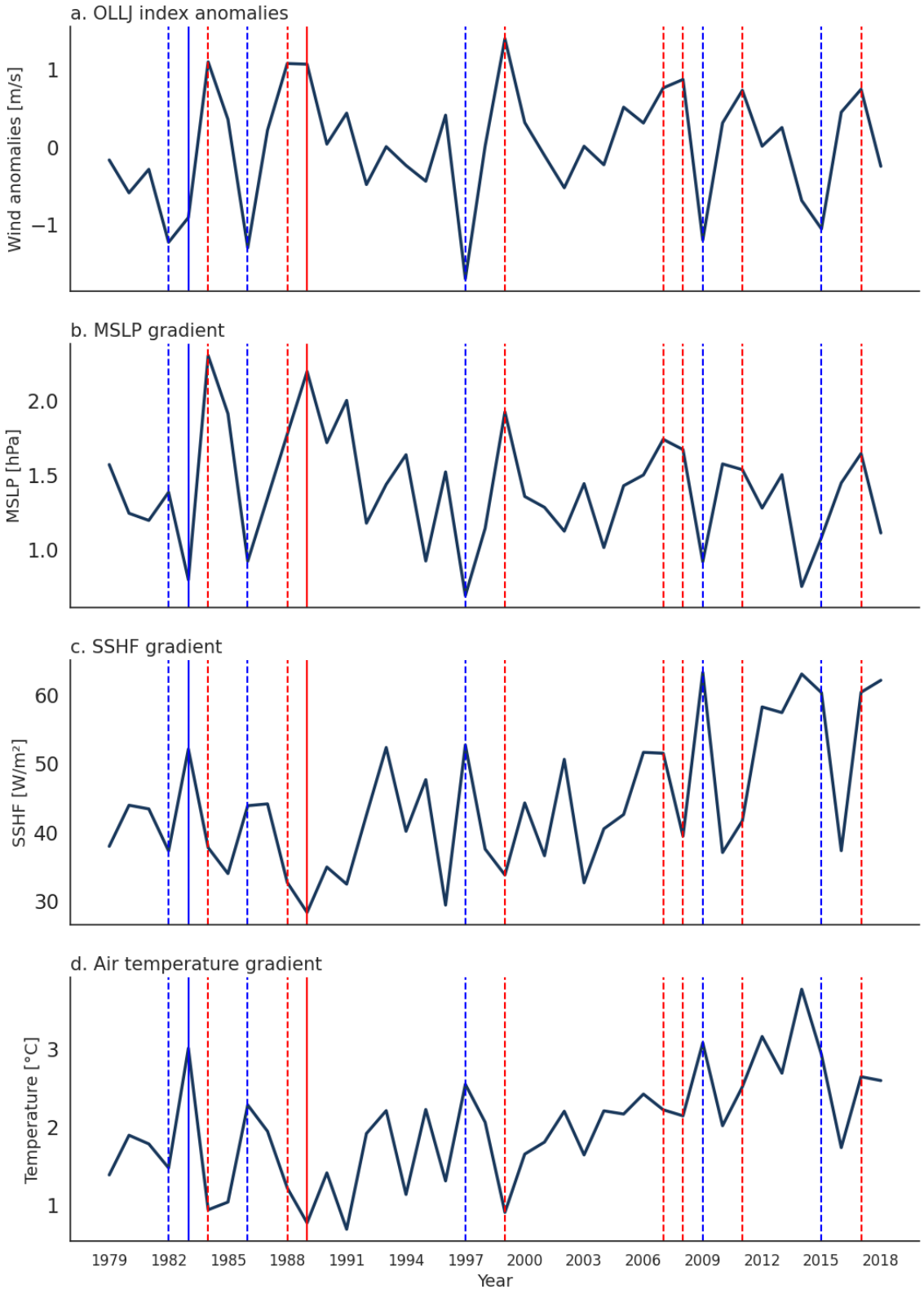

Figure S1.5: a) Anomalies of the OLLJ index at region C3.4 for DJF using ERA5 data during 1979-2019. Gradients of b) MSLP, c) SSHF and d) near-surface temperature between the Orinoco and the Andes-Amazon transition region. Red vertical lines indicate the occurrence of a strong OLLJ in DJF. Blue lines represent the years of the occurrence of a weak OLLJ.

Chapter 2

The Orinoco low-level jet in the historical experiment of CMIP5/CMIP6 models

2.1 Introduction

Higher concentrations of GHGs in the atmosphere and their associated effect on the Earth's energy balance are recognized as the causes of the global warming observed since the industrial revolution (Gulev et al., 2021; IPCC, 2021). The observed increases in well-mixed GHG concentrations since around 1750 are unequivocally caused by human activities (IPCC, 2021). Also, it is unequivocal that human influence has warmed the atmosphere, ocean, and land; consequently, widespread and rapid changes in the atmosphere, ocean, cryosphere, and biosphere have occurred (IPCC, 2021). In this sense, one of the main effects of climate change is the rise in global mean temperature, which affects the structure and characteristics of the Earth system components at different temporal and spatial scales (Chen et al., 2021). In addition, the intensification of the hydrological cycle, with the occurrence of more frequent and severe droughts and heavy precipitation events, is another feature of climate change (Allan et al., 2020; Douville et al., 2021; IPCC, 2021; Seneviratne et al., 2021). The knowledge about the specific variations in the Earth system components in the context of climate change is crucial to assess their associated impacts on the ecosystems and human activities.

Monitoring the meteorological conditions worldwide during extended periods allows the identification of shifts in the Earth's system components. Another approach widely used to evaluate changes in the climate system at different scales is using General Circulation Models (GCMs), which enable the evaluation of present characteristics of the climate system and suggest possible future changes in these features (CCSP, 2008). Specifically, those models included in the Coupled Model Intercomparison Project (CMIP) are used by the Intergovernmental Panel on Climate Change (IPCC) to assess the scientific evidence of human-induced climate change in the Earth system because of the uniformity of their experiments, such as the initial conditions and parametrizations. Since the first unified experiments were performed using GCMs, CMIP has applied changes in the activities, experiments, and guidelines to compare the model's estimates, resulting in different CMIP phases. CMIP5 (Taylor et al., 2012) and CMIP6 (Eyring et al., 2016) are the most recent phases of the project that encompass the response of a high number of GCMs from different institutes worldwide under different forcing.

In Chapter 1, we analyzed the main features of the Orinoco low-level jet (OLLJ) and its role in atmospheric moisture transport from the Atlantic Ocean and the Orinoco basin to the Amazon. Our results, in agreement with other studies, confirm the importance of the OLLJ in the hydroclimate of northern South America (e.g., Jiménez-Sánchez et al., 2019, 2020; Builes-Jaramillo et al., 2022a, 2022b; Martínez et al., 2022). The above suggests the relevance of analyzing how GCMs represent the OLLJ during the recent past to assess changes in this low-level jet (LLJ) in the context of climate change.

Previous studies analyze how GCMs simulate the structure of different LLJs worldwide under historical forcing (e.g historical conditions of solar variability, volcanic activity, GHG concentrations, among others), based on their annual cycle, vertical structure, and horizontal distribution, among other characteristics (e.g., Martin and Schumacher, 2011; Sheffield et al., 2013; Danco and Martin, 2018; Sierra et al., 2018, 2021; Oscar et al., 2022). On the other hand, other studies evaluate the connections between the intensification of LLJs, atmospheric moisture fluxes, and precipitation in the regions of influence, as LLJs play a relevant role in atmospheric moisture

transport (e.g., Stensrud et al., 1996; Martin and Schumacher, 2011; Acosta and Huber, 2017; Algarra et al., 2019; Braz et al., 2021; Munday et al., 2021; Makinde et al., 2022).

Although GCMs have been useful in understanding the variability of the different processes influencing the Earth system, it is essential to consider the uncertainties associated with this dataset. The uncertainties and deviations of the model estimates are associated with multiple factors such as internal climate variations and the uncertainty of the climate response. Besides, model performance depends on limitations due to the simplifications considered by these models, the parameterizations included to simulate specific processes, and the grid size and its equivalence in the structures that can be adequately represented (Chen et al., 2021). Also, Working Group I in the Fifth Assessment Report of the IPCC points out that the observational information used in the model's evaluation and the internal variability is among the different sources of uncertainties in simulations (Flato et al., 2013; Collins et al., 2013). Different studies analyze this last factor around several LLJs, such as the Great Plains LLJ (Wimhurst and Greene, 2020) or the LLJs on the eastern coast of Africa (Munday et al., 2021), suggesting a direct relationship between a finer spatial resolution and a better model performance. However, other studies indicate that an adequate representation of some LLJs, like the Choco LLJ in northwestern South America, does not completely depend on the spatial resolution of the models considered (Sierra et al., 2018).

Additionally, the simulation of the main characteristics of LLJs by GCMs is strongly influenced by the model skill in the representation of the mechanisms that allow the activation and strengthening of the jet, such as surface pressure or temperature gradients (e.g., Bracegirdle et al., 2022; Sierra et al., 2018). The above implies that the analysis of the LLJs, and generally of other climatological processes, depends on the ability of GCMs to adequately represent these structures. The comparison of GCM estimates with other available datasets, usually reanalyses, allows the evaluation of the performance of the GCMs in the representation of different phenomena, enabling the classification of these models in terms of their capacity to simulate present climate features.

Our literature review indicates that although previous studies have analyzed the main features of the OLLJ, using observational and modeling approaches, none of these studies have explored the ability of current GCMs to represent this low-level circulation or its possible changes under different climate change scenarios. Thus, this chapter focuses on how GCMs included in CMIP5/CMIP6 simulate the main characteristics of the OLLJ under the historical experiment (simulations under observed forcing of solar variability, volcanic activity, GHG concentrations) (Taylor et al., 2012; Eyring et al., 2016). The above is relevant due to the role of the OLLJ in moisture fluxes in northern South America and, therefore, its importance in the modulation of the regional climate (Jiménez-Sánchez et al., 2019, 2020; Builes-Jaramillo et al., 2022a; Martínez et al., 2022), as analyzed in Chapter 1. Evaluating the OLLJ from the response of GCMs to observed forcings enables a better understanding of the regional climatic processes during the recent past in northern South America, which in turn allows evaluating possible future changes of this LLJ that may affect the hydro-climatological conditions in the region.

2.2 Data and methodology

In this chapter, we analyze the annual cycle of the OLLJ using the simulations of 37 CMIP5 models and 34 CMIP6 models under the historical experiment, considering the first model initialization (r1i1p1 for CMIP5 and r1i1p1f1 for CMIP6). We focus on the analysis of zonal and meridional wind components at different pressure levels at a monthly frequency to evaluate the monthly variations of the OLLJ in northern South America. We use CMIP5/CMIP6 models as they correspond to the most recent versions of GCMs included in the CMIP experiments. Also, the consideration of two CMIP phases allows the comparison of the differences between them. In the historical experiment, CMIP5 covers the period 1850-2005 and CMIP6 the period 1850-2014. CMIP5/CMIP6 models are evaluated using the ERA5 reanalysis (Hersbach et al., 2020), which is available for the period 1979-present. Thus, the period of analysis in this chapter encompasses the period 1979-2005 for CMIP5 models, and

1979-2014 for CMIP6 models. Table 2.1 presents the models used in this analysis, their spatial resolution, and available experiments.

As analyzed in Chapter 1, the main features of the OLLJ can be evaluated using the monthly OLLJ index, the seasonal vertical structure of the wind field, and the seasonal spatial distribution of the horizontal wind, estimated from the ERA5 reanalysis. In this chapter, we compare the simulations from the GCMs presented in Table 2.1 with that from ERA5. For calculating the OLLJ index, we use the C3.4 region (black rectangle in Figure 2.1) since it encompasses a larger spatial domain than the four regions suggested by Jiménez-Sánchez et al. (2019) (regions C1 to C4 in Figure 1.1). This method could allow better identification of the OLLJ in GCMs, which tend to have coarse spatial resolutions; therefore, they may misrepresent this low-level circulation in a small domain. Similarly, the cross-section used to evaluate the vertical structure of the OLLJ is centered on the region C3.4 but includes a wider range of longitudinal bands (3°N-5°N and 75°W-61°W) to identify the core of the OLLJ, as suggested by Rodriguez-Gómez et al. (2022)(black dashed rectangle in Figure 2.1). On the other hand, following the findings discussed in Chapter 1, we focus on the pressure levels between 825 and 950 hPa to estimate the OLLJ index and the seasonal variation of the horizontal wind in northern South America. Figure 2.1 shows the regions described above and considered in our analysis of the CMIP5/CMIP6 simulations of the OLLJ.

Following the methodology proposed by Sierra (2017) and Sierra et al. (2018), we use the Root Mean Square Error (RMSE) and the pattern correlation coefficient (PCC) as the evaluation metrics of the performance of each model in the simulation of the observed seasonal characteristics of the OLLJ (Taylor, 2001). For calculating the evaluation metrics, ERA5 data is interpolated to each model grid size (Table 2.1) by bilinear interpolation, which considers a linear interpolation in two different directions and is widely used in managing two-dimensional matrices. Then, to classify the set of CMIP5/CMIP6 models according to their ability to simulate seasonal variations of the wind field in northern South America, we perform a factor analysis using the metrics described above. From this methodology, it is possible to obtain a small number of factors that explain most of the original variance and

Table 2.1: CMIP5 and CMIP6 models used in this study for the historical experiment.

Model	CMIP phase	Institution	Resolution (lat x lon)	Reference
ACCESS1-0	CMIP5	Commonwealth Scientific and Industrial Research Organisation, Australia, Bureau of Meteorology, Australia	1.2° x 1.8°	Dix et al. (2013)
ACCESS1-3	CMIP5	Commonwealth Scientific and Industrial Research Organisation, Australia, Bureau of Meteorology, Australia	1.2° x 1.8°	Dix et al. (2013)
CanCM4	CMIP5	Canadian Centre for Climate Modelling and Analysis	2.7° x 2.8°	Merryfield et al. (2013)
CanESM2	CMIP5	Canadian Centre for Climate Modelling and Analysis	2.7° x 2.8°	Arora et al. (2011)
CMCC-CESM	CMIP5	Centro Euro-Mediterraneo per I Cambiamenti Climatici	3.7° x 3.7°	Vichi et al. (2011)
CMCC-CM	CMIP5	Centro Euro-Mediterraneo per I Cambiamenti Climatici	0.7° x 0.7°	Scoccimarro et al. (2011)
CMCC-CMS	CMIP5	Centro Euro-Mediterraneo per I Cambiamenti Climatici	1.8° x 1.8°	Scoccimarro et al. (2011)
CNRM-CM5	CMIP5	Centre National de Recherches Meteorologiques / Centre Europeen de Recherche et Formation Avancees en Calcul Scientifique	1.4° x 1.4°	Voldoire et al. (2013)
CNRM-CM5-2	CMIP5	Centre National de Recherches Meteorologiques / Centre Europeen de Recherche et Formation Avancees en Calcul Scientifique	1.4° x 1.4°	Sénési et al. (2014)
CSIRO-Mk3-6-0	CMIP5	Commonwealth Scientific and Industrial Research Organisation in collaboration with the Queensland Climate Change Centre of Excellence	1.8° x 1.8°	Jeffrey et al. (2013)
GFDL-CM2.1	CMIP5	Geophysical Fluid Dynamics Laboratory	1.5° x 2.5°	Delworth et al. (2006)
GFDL-CM3	CMIP5	Geophysical Fluid Dynamics Laboratory	2° x 2.5°	Donner et al. (2011)
GFDL-ESM2G	CMIP5	Geophysical Fluid Dynamics Laboratory	1.5° x 2.5°	Dunne et al. (2012)

Table 2.1: Continuation

Model	CMIP phase	Institution	Resolution (lat x lon)	Reference
GFDL-ESM2M	CMIP5	Geophysical Fluid Dynamics Laboratory	1.5° x 2.5°	Dunne et al. (2012)
GISS-E2-H	CMIP5	NASA Goddard Institute for Space Studies	2° x 2.5°	Schmidt et al. (2014)
GISS-E2-H-CC	CMIP5	NASA Goddard Institute for Space Studies	2° x 2.5°	Romanou et al. (2013)
GISS-E2-R	CMIP5	NASA Goddard Institute for Space Studies	2° x 2.5°	Schmidt et al. (2014)
GISS-E2-R-CC	CMIP5	NASA Goddard Institute for Space Studies	2° x 2.5°	Romanou et al. (2013)
HadCM3	CMIP5	Met Office Hadley Centre (additional HadGEM2-ES realizations contributed by Instituto Nacional de Pesquisas Espaciais)	2.5° x 3.7°	Gordon et al. (2000)
HadGEM2-AO	CMIP5	National Institute of Meteorological Research/Korea Meteorological Administration	1.2° x 1.8°	Bellouin et al. (2011)
HadGEM2-CC	CMIP5	Met Office Hadley Centre (additional HadGEM2-ES realizations contributed by Instituto Nacional de Pesquisas Espaciais)	1.2° x 1.8°	Bellouin et al. (2011)
HadGEM2-ES	CMIP5	Met Office Hadley Centre (additional HadGEM2-ES realizations contributed by Instituto Nacional de Pesquisas Espaciais)	1.2° x 1.8°	Bellouin et al. (2011)
INM-CM4	CMIP5	Institute for Numerical Mathematics	1.5° x 2°	Volodin et al. (2014)
IPSL-CM5A-LR	CMIP5	Institut Pierre-Simon Laplace	1.8° x 3.7°	Dufresne et al. (2013)
IPSL-CM5A-MR	CMIP5	Institut Pierre-Simon Laplace	1.2° x 2.5°	Dufresne et al. (2013)
IPSL-CM5B-LR	CMIP5	Institut Pierre-Simon Laplace	1.8° x 3.7°	Hourdin et al. (2013b)
MIROC-ESM	CMIP5	Japan Agency for Marine-Earth Science and Technology, Atmosphere and Ocean Research Institute (The University of Tokyo), and National Institute for Environmental Studies	2.8° x 2.8°	Watanabe et al. (2011)

Table 2.1: Continuation

Model	CMIP phase	Institution	Resolution (lat x lon)	Reference
MIROC-ESM-CHEM	CMIP5	Japan Agency for Marine-Earth Science and Technology, Atmosphere and Ocean Research Institute (The University of Tokyo), and National Institute for Environmental Studies	2.8° x 2.8°	Watanabe et al. (2011)
MIROC4h	CMIP5	Atmosphere and Ocean Research Institute (The University of Tokyo), National Institute for Environmental Studies, and Japan Agency for Marine-Earth Science and Technology	0.5° x 0.5°	Sakamoto et al. (2012)
MIROC5	CMIP5	Atmosphere and Ocean Research Institute (The University of Tokyo), National Institute for Environmental Studies, and Japan Agency for Marine-Earth Science and Technology	1.4° x 1.4°	Watanabe et al. (2010)
MPI-ESM-MR	CMIP5	Max Planck Institute for Meteorology (MPI-M)	1.8° x 1.8°	Giorgetta et al. (2013)
MPI-ESM-P	CMIP5	Max Planck Institute for Meteorology (MPI-M)	1.8° x 1.8°	Giorgetta et al. (2013)
MPI-ESM-LR	CMIP5	Max Planck Institute for Meteorology (MPI-M)	1.8° x 1.8°	Giorgetta et al. (2013)
MRI-CGCM3	CMIP5	Meteorological Research Institute	1.1° x 1.1°	Yukimoto et al. (2012)
MRI-ESM1	CMIP5	Meteorological Research Institute	1.1° x 1.1°	Yukimoto et al. (2011)
NorESM1-M	CMIP5	Norwegian Climate Centre	1.8° x 2.5°	Bentsen et al. (2013)
NorESM1-ME	CMIP5	Norwegian Climate Centre	1.8° x 2.5°	Tjiputra et al. (2013)
ACCESS-CM2	CMIP6	Commonwealth Scientific and Industrial Research Organisation, Australian Research Council Centre of Excellence for Climate System Science	1.2° x 1.8°	Bi et al. (2020)
ACCESS-ESM1-5	CMIP6	Commonwealth Scientific and Industrial Research Organisation	1.2° x 1.8°	Ziehn et al. (2020)
BCC-CSM2-MR	CMIP6	Beijing Climate Center	1.1° x 1.1°	Wu et al. (2019)
BCC-ESM1	CMIP6	Beijing Climate Center	2.8° x 2.8°	Wu et al. (2020)

Table 2.1: Continuation

Model	CMIP phase	Institution	Resolution (lat x lon)	Reference
CAMS-CSM1-0	CMIP6	Chinese Academy of Meteorological Sciences	1.1° x 1.1°	Xin-Yao et al. (2019)
CanESM5	CMIP6	Canadian Centre for Climate Modelling and Analysis	2.8° x 2.8°	Swart et al. (2019)
CESM2-FV2	CMIP6	National Center for Atmospheric Research	1.9° x 2.5°	Danabasoglu (2019)
CMCC-CM2-HR4	CMIP6	Fondazione Centro Euro-Mediterraneo sui Cambiamenti Climatici	0.9° x 1.2°	Cherchi et al. (2019)
CMCC-CM2-SR5	CMIP6	Fondazione Centro Euro-Mediterraneo sui Cambiamenti Climatici	0.9° x 1.2°	Cherchi et al. (2019)
CMCC-ESM2	CMIP6	Fondazione Centro Euro-Mediterraneo sui Cambiamenti Climatici	0.9° x 1.2°	Cherchi et al. (2019)
E3SM-1-0	CMIP6	Lawrence Livermore National Laboratory, Argonne National Laboratory, Brookhaven National Laboratory, Los Alamos National Laboratory,Lawrence Berkeley National Laboratory, Oak Ridge National Laboratory, Pacific Northwest National Laboratory, Sandia National Laboratories, Department of Earth System Science	1.0° x 1.0°	Golaz et al. (2019)
E3SM-1-1-ECA	CMIP6	Lawrence Livermore National Laboratory, Argonne National Laboratory, Brookhaven National Laboratory, Los Alamos National Laboratory,Lawrence Berkeley National Laboratory, Oak Ridge National Laboratory, Pacific Northwest National Laboratory, Sandia National Laboratories	1.0° x 1.0°	Burrows et al. (2020)
FIO-ESM-2-0	CMIP6	First Institute of Oceanography, Qingdao National Laboratory for Marine Science and Technology	0.9° x 1.2°	Bao et al. (2020)
GFDL-ESM4	CMIP6	National Oceanic and Atmospheric Administration, Geophysical Fluid Dynamics Laboratory	1.0° x 1.2°	Dunne et al. (2020)
GISS-E2-1-G	CMIP6	Goddard Institute for Space Studies	2.0° x 2.5°	Kelley et al. (2020)

Table 2.1: Continuation

Model	CMIP phase	Institution	Resolution (lat x lon)	Reference
GISS-E2-1 -H	CMIP6	Goddard Institute for Space Studies	2.0° x 2.5°	Kelley et al. (2020)
GISS-E2-2-H	CMIP6	Goddard Institute for Space Studies	2.0° x 2.5°	Rind et al. (2020)
IITM-ESM	CMIP6	Centre for Climate Change Research, Indian Institute of Tropical Meteorology Pune	1.9° x 1.9°	Krishnan et al. (2021)
INM-CM5-0	CMIP6	Institute for Numerical Mathematics	1.5° x 2.0°	Volodin and Gritsun (2018)
IPSL-CM5A2-INCA	CMIP6	Institut Pierre-Simon Laplace	1.8° x 3.7°	Sepulchre et al. (2020)
IPSL-CM6A-LR	CMIP6	Institut Pierre-Simon Laplace	1.3° x 2.5°	Boucher et al. (2020)
IPSL-CM6A-LR-INCA	CMIP6	Institut Pierre-Simon Laplace	1.3° x 2.5°	Boucher et al. (2020)
KACE-1-0-G	CMIP6	National Institute of Meteorological Sciences, Korea Meteorological Administration	1.2° x 1.8°	Lee et al. (2020)
KIOST-ESM	CMIP6	Korea Institute of Ocean Science and Technology	1.9° x 1.9°	Pak et al. (2021)
MCM-UA-1-0	CMIP6	Department of Geosciences, University of Arizona	2.2° x 3.7°	Stouffer (2019)
MIROC6	CMIP6	Japan Agency for Marine-Earth Science and Technology, Atmosphere and Ocean Research Institute (The University of Tokyo), National Institute for Environmental Studies, Ibaraki 305-8506, RIKEN Center for Computational Science	1.4° x 1.4°	Tatebe et al. (2019)
MPI-ESM-1-2-HAM	CMIP6	ETH Zurich, Max Planck Institut fur Meteorologie, Forschungszentrum Julich, University of Oxford, Finnish Meteorological Institute, Leibniz Institute for Tropospheric Research, Center for Climate SystemsModeling (C2SM) at ETH Zurich	1.8° x 1.8°	Mauritsen et al. (2019)

Table 2.1: Continuation

Model	CMIP phase	Institution	Resolution (lat x lon)	Reference
MPI-ESM1 -2-LR	CMIP6	Max Planck Institute for Meteorology, Alfred Wegener Institute, Helmholtz Centre for Polar and Marine Research, Deutsches Klimarechenzentrum, Deutscher Wetterdienst	1.8° x 1.8°	Mauritsen et al. (2019)
MPI-ESM1-2-HR	CMIP6	Max Planck Institute for Meteorology, Deutsches Klimarechenzentrum, Deutscher Wetterdienst	0.9° x 0.9°	Mauritsen et al. (2019)
MRI-ESM2-0	CMIP6	Meteorological Research Institute	1.1° x 1.1°	Yukimoto et al. (2019)
NorCPM1	CMIP6	Center for International Climate and Environmental Research, Norwegian Meteorological Institute, Nansen Environmental and Remote Sensing Center, Norwegian Institute for Air Research, University of Bergen, University of Oslo, Uni Research	1.8° x 2.5°	Bethke et al. (2021)
NorESM2-LM	CMIP6	Center for International Climate and Environmental Research, Norwegian Meteorological Institute, Nansen Environmental and Remote Sensing Center, Norwegian Institute for Air Research, University of Bergen, University of Oslo, Uni Research	1.8° x 2.5°	Seland et al. (2020)
NorESM2-MM	CMIP6	Center for International Climate and Environmental Research, Norwegian Meteorological Institute, Nansen Environmental and Remote Sensing Center, Norwegian Institute for Air Research, University of Bergen, University of Oslo, Uni Research	0.9° x 1.2°	Seland et al. (2020)
SAM0-UNICON	CMIP6	NCC Seoul National University	0.9° x 1.2°	Park et al. (2019)

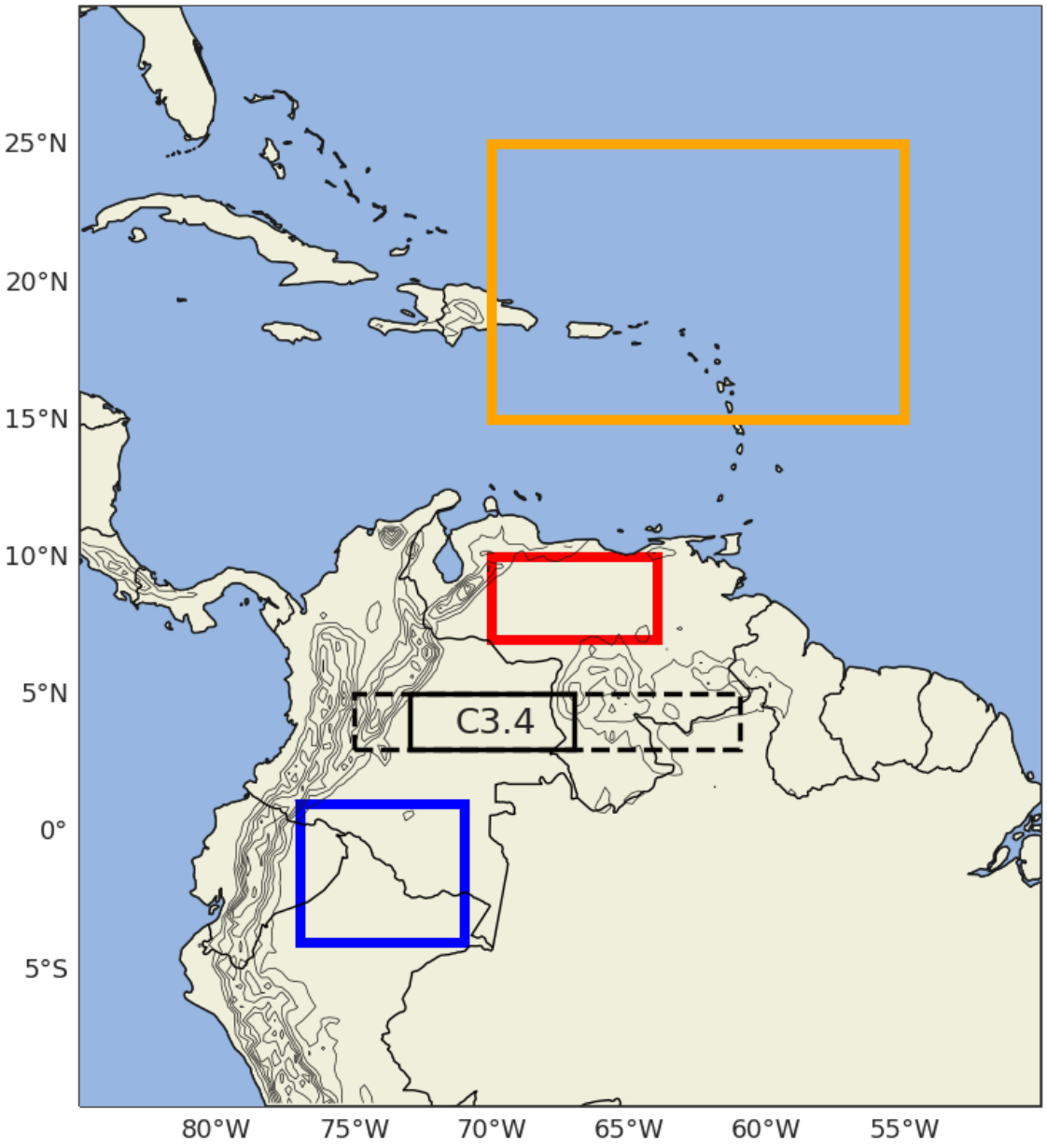

Figure 2.1: Spatial domains consider to evaluate the simulation of the main OLLJ characteristics by the CMIP5 and CMP6 models used: region C3.4 (black), vertical cross-section (black dashed), Tropical North Atlantic (orange), Orinoco (red) and Andes-Amazon transition (blue).

allows the reduction of the number of variables to classify the models (Rencher, 2003; Sierra et al., 2018). Finally, we use cluster analysis to obtain a grouping of the CMIP5/CMIP6 models from the factors selected by the factor analysis. In this sense, cluster analysis is a statistical technique that allows defining groups of a set of individuals, thus the individuals within a cluster are similar while they tend to differ from those classified in other groups (Wilks, 2006). After obtaining the groups, we focus on how each cluster represents the main characteristics of the OLLJ. The models within each cluster are gridded to a common grid size of 2°X2° by bilinear interpolation to obtain the multi-model mean of the horizontal wind patterns, the vertical structure of the jet, and the OLLJ index for each cluster of GCMs.

On the other hand, we evaluate the monthly variation of the gradients of mean sea level pressure (MSLP) and near-surface air temperature between the Tropical North Atlantic and the Amazon, since the contrast in pressure and heating between these regions is related to the activation of the OLLJ (Builes-Jaramillo et al., 2022b; Martínez et al., 2022), as discussed in Chapter 1. In particular, these gradients play an important role in the interannual variability of the OLLJ intensity. For instance, Builes-Jaramillo et al. (2022b) highlight that the occurrence of stronger (weaker) MSLP gradients between these regions during La Niña (El Niño) years is associated with a stronger (weaker) OLLJ. These gradients are calculated as the difference between the spatial average of the MSLP and air temperature in the Tropical North Atlantic (orange rectangle in Figure 2.1) and the Andes-Amazon transition (blue rectangle in Figure 2.1; Martínez et al., 2022) from the multi-model mean of the clusters. This analysis is relevant because it can relate the performance of the different clusters with their simulation of the low-level circulation and the land surface patterns that enhance the OLLJ.

Finally, this chapter analyzes the representation of the MSLP, Surface Sensible Heat Flux (SSHF), and near-surface air temperature gradients between the Orinoco and the Andes-Amazon transition regions (red and blue rectangles in Figure 2.1, respectively; Martínez et al., 2022) according to the GCMs considered. The above acquires relevance as these regional gradients between the jet entrance and exit regions are important for interannual variations of the OLLJ intensity (see section 1.3.5). Fol-

lowing the methodology used in Chapter 1, we consider the long-term anomaly time series of the OLLJ index during DJF, to identify the years of strong and weak jet events. Identifying these particular years with marked fluctuations in a strengthening of the OLLJ allows for assessing the characteristic patterns of MSLP, SSHF, and air temperature gradients during strong and weak OLLJ events and the ability of GCMs to simulate these links.

2.3 Results

2.3.1 The Orinoco low-level jet index in CMIP5/CMIP6 models

Following Chapter 1, to estimate the OLLJ index in region C3.4 we use the wind magnitude because the orientation of the flow at the exit of the jet has important contributions from both the zonal and meridional components (Figure 1.4). However, we compare how CMIP5/CMIP6 models represent the OLLJ index in region C3.4 while considering the zonal and meridional wind components individually as well as the wind magnitude, to identify if the main biases in the representation of the low-level circulation arise from difficulties in the representation of a particular component. Figure 2.2 shows the multimodel mean of the annual cycle of the OLLJ index at region C3.4 for CMIP5/CMIP6 models during the historical period. The OLLJ index estimated using the zonal wind (orange line) exhibits lower variations throughout the year, with little differences between the wind speed in DJF, which corresponds to the activation period of the jet, and JJA, which corresponds to its weakening period. In contrast, the OLLJ index from the meridional wind (blue line) displays marked changes during the year, allowing better identification of the strengthening and weakening periods of the jet. In terms of the wind magnitude (green line), it loses some variability as the contrast between DJF and JJA decreases as it combines both zonal and meridional wind. As analyzed in Chapter 1, the OLLJ index in region C3.4 is influenced by both zonal and meridional components of the wind field. However, CMIP5/CMIP6 simulations of the zonal wind in region

C3.4 differ from that depicted by ERA5, where the estimates of the models (orange line) do not exhibit the monthly variability obtained from ERA5 (dotted black line), suggesting biases of the CMIP models simulating the mean zonal flow in the region.

The estimations of CMIP5/CMIP6 models using meridional wind show greater agreement with that obtained from ERA5 (black line), as both CMIP models and ERA5 exhibit contrasts of up to 7 m/s between DJF and JJA. The above suggests that as GCMs tend to have difficulties simulating zonal wind in the region, the OLLJ index at region C3.4 estimated from the wind magnitude may not present the best variation of the wind field at the jet exit. Hence, in this chapter and hereafter, we estimate the OLLJ index from the spatial average of the meridional wind component between 825 and 950 hPa in region C3.4 for ERA5 and CMIP5/CMIP6 models. We acknowledge that the C3.4 region is located in complex terrain, between the Andes Mountain range and the Guiana highlands, which can also add uncertainties to the model estimates.

2.3.2 Factor analysis and cluster analysis of the CMIP5/CMIP6 models

As explained in section 2.2, we classify the CMIP5/CMIP6 models in terms of their representation of the seasonal characteristics of the OLLJ focusing on the RMSE and PCC estimates of the horizontal wind, vertical structure, and monthly OLLJ index. Based on these metrics, we perform a factor analysis to reduce the multicollinearity between these estimates and the number of observed variables to be considered in the cluster analysis. Figure 2.3 shows the scree plots of the factor analysis for CMIP5 and CMIP6 models. The scree plot indicates the number of factors to keep the largest amount of information of the original variables with the minimum number of factors. According to Figure 2.3, the number of factors to be retained from the estimates of the CMIP5 models is four, while for CMIP6 is three, retaining 93% and 91% of the original variance, respectively. We selected the factors with eigenvalues greater than one; therefore, each factor selected may explain more information than one of the original variables.

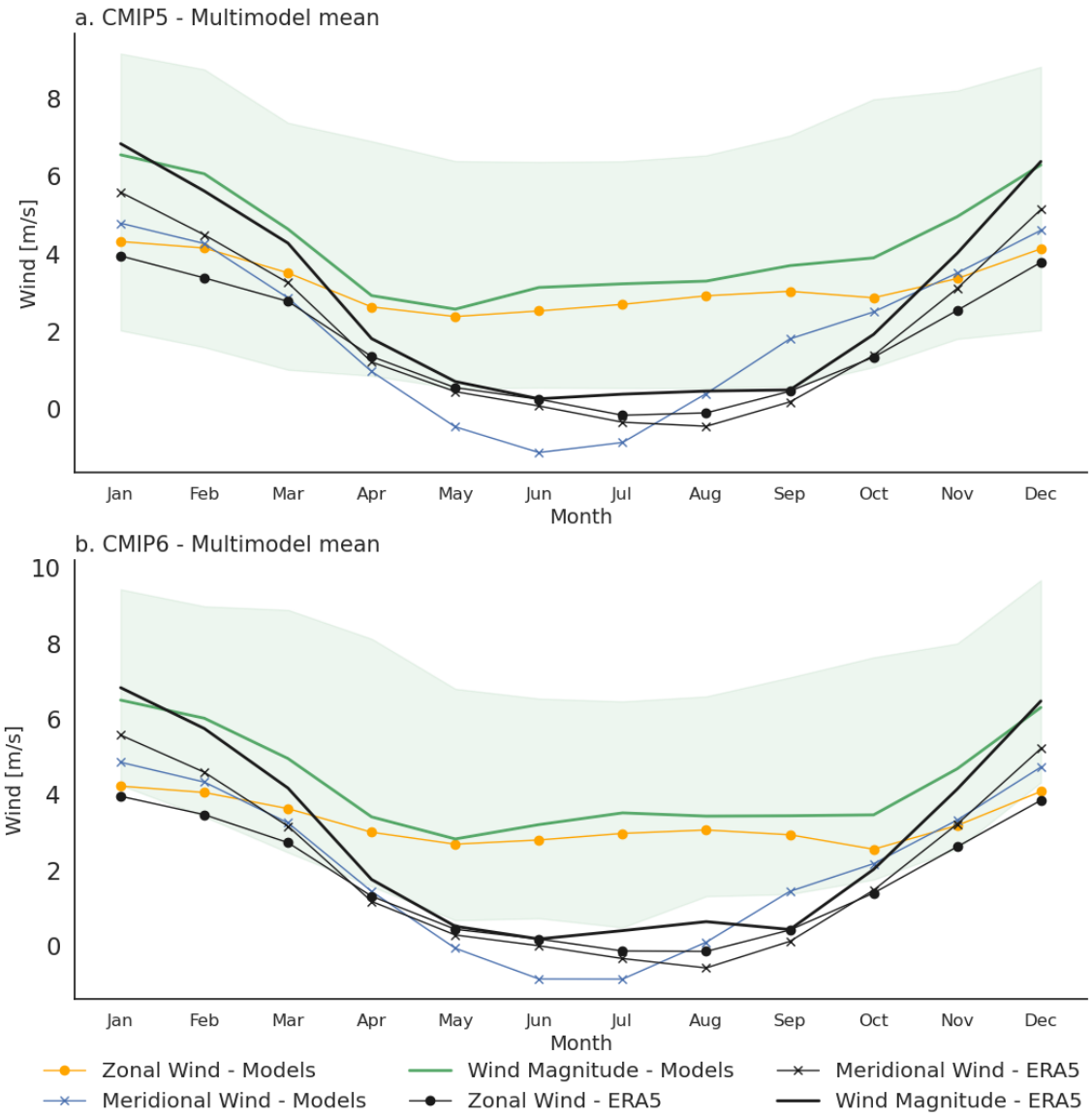

Figure 2.2: Multi-model means of CMIP5/CMIP6 simulations of the OLLJ index in region C3.4 during the historical period, as a function of: zonal (orange line) and meridional (blue line) wind components, and the wind magnitude (green line). The black line represents the OLLJ index from ERA5 wind magnitude (see Chapter 1), and the green shading corresponds to the envelope of the model estimates of the OLLJ index from wind magnitude. The black lines with dots and crosses represent the OLLJ index from zonal and meridional wind components from ERA5, respectively.

The factors associated with each CMIP phase are the inputs for the cluster analysis based on Ward's minimum variance method (Ward, 1963). As the cluster analysis requires the number of clusters (k) to perform the classification, we focus on two methods to select the optimal number of clusters to be retained: the elbow method and the silhouette analysis. The elbow method calculates the sum of the squared distances of each point to its associated centroid, which is estimated for different values of k. The silhouette analysis focuses on the silhouette score that indicates if a sample is far from other clusters (closest to 1) or if the sample is close to other clusters (closest to 0), indicating a deficient differentiation among some clusters (Kodinariya et al., 2013). Figure 2.4 presents the elbow plot for a set of k clusters for CMIP5 and CMIP6 models, showing that an inflection point in the curve occurs near k=4 in CMIP5 models, and k=3 and k=4 in CMIP6 models. These results suggest that a possible optimal number of clusters for CMIP5 and CMIP6 models may be k=4 and k=3 or 4, respectively.

On the other hand, Figures 2.5 and 2.6 show the silhouette plots for different k clusters from the CMIP5 and CMIP6 performance metric-based factors, including the average silhouette coefficient of the clusters and the size of the silhouette plots. A set of k clusters in which not all clusters' silhouette coefficients are greater than the average (red line) is not an adequate selection. At the same time, it is also relevant to consider the thickness of the silhouette plot of each cluster as thicker silhouette plots may suggest the merge of different clusters into one, influencing the differentiation of specific clusters (Rousseeuw, 1987).

For CMIP5, some k clusters such as 5, 6, and 7 (Figure 2.5) are not the optimal selection as there are clusters with a silhouette score lower than average. On the other hand, the size of the silhouette plots suggests that k=2 clusters may not be adequate as they may contain independent clusters. The above suggests that an optimal k for CMIP5 information may be 3 or 4. Regarding the classification of CMIP6 models, k clusters 2, 5, 6, and 7 are not optimal because the silhouette scores of some groups are either lower than the average or there is no associated score (Figure 2.6). Again, the silhouette analysis for CMIP6 models suggests an

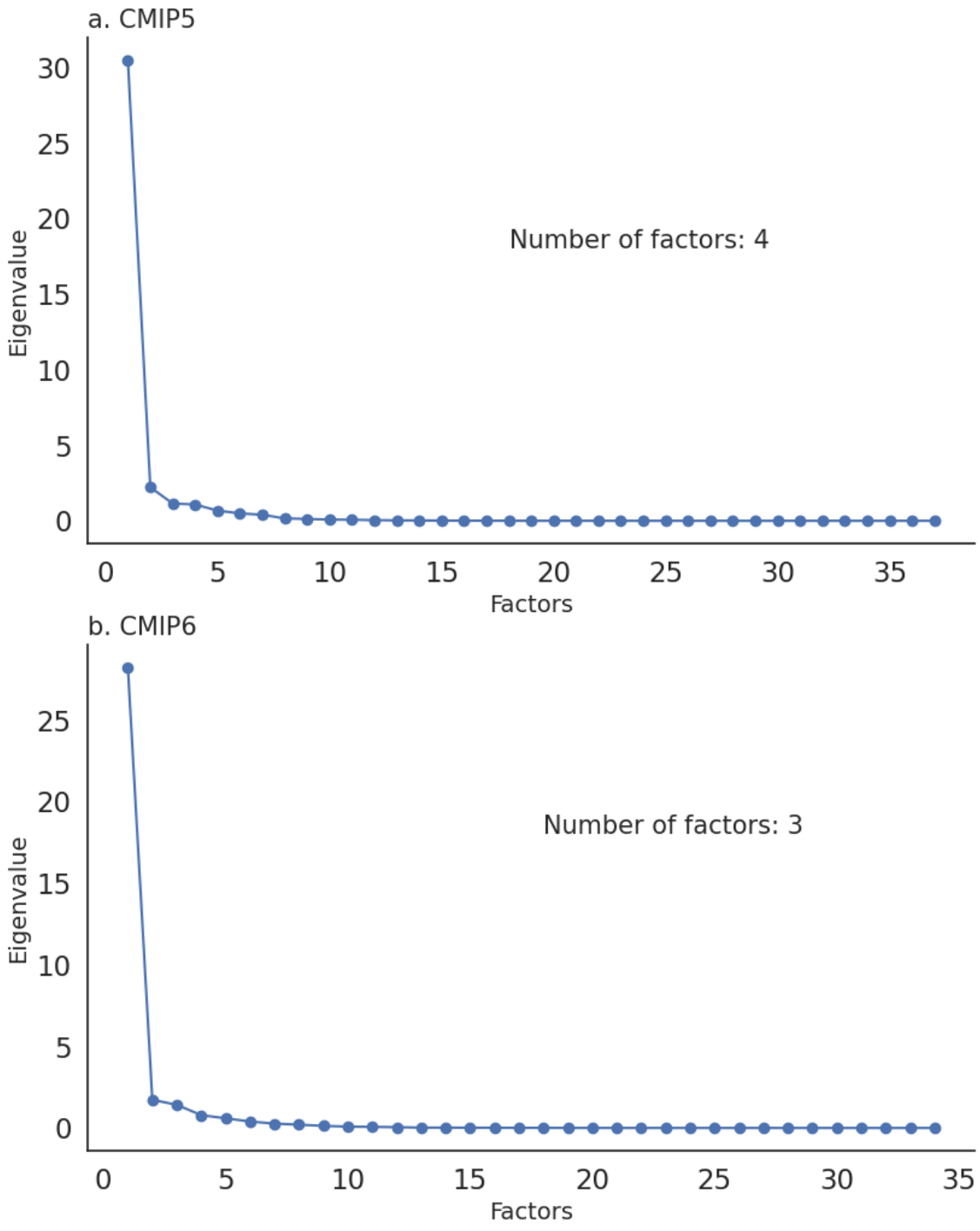

Figure 2.3: Scree plot of the factor analysis for metrics of the OLLJ main features from a) CMIP5 and b) CMIP6 models.

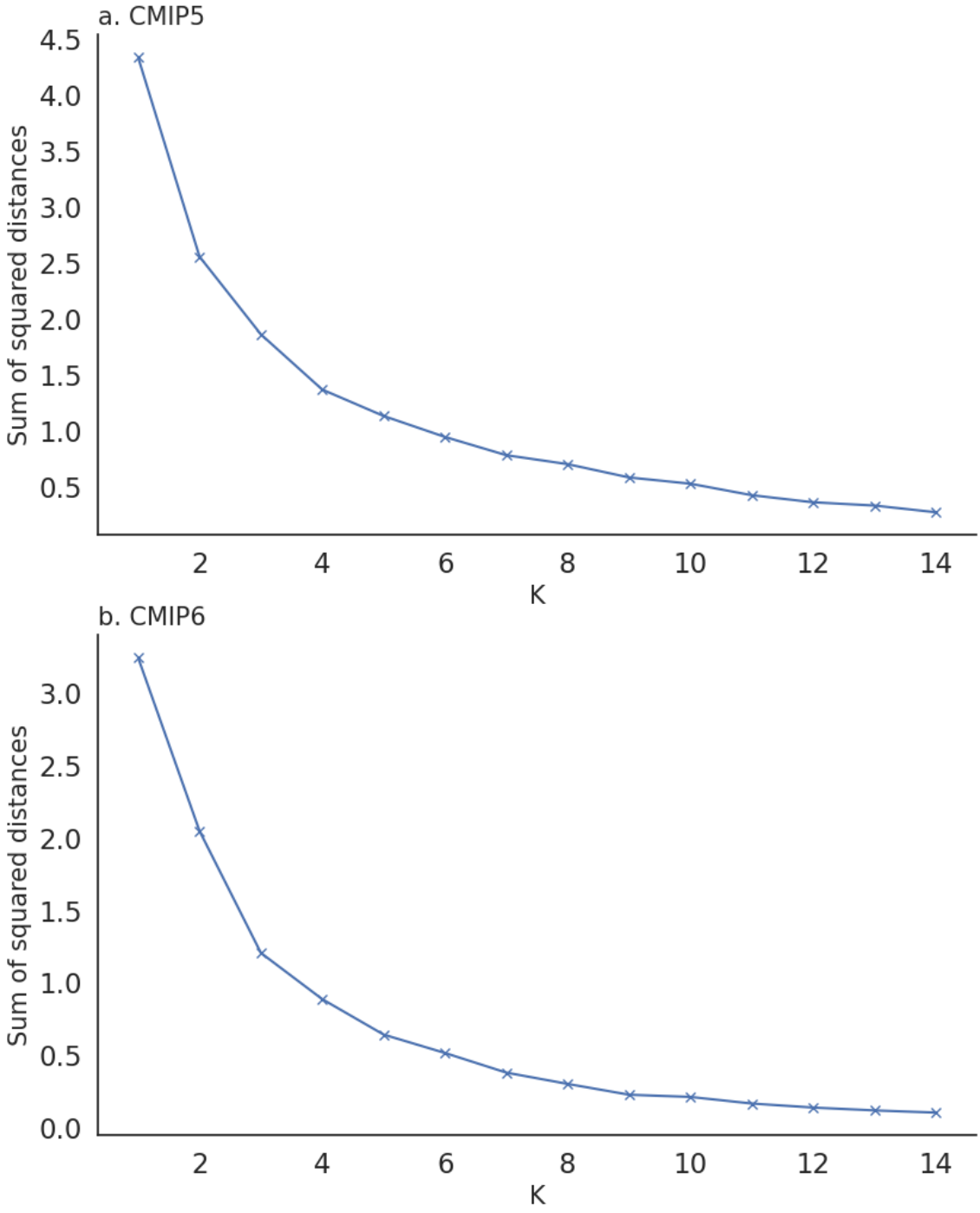

Figure 2.4: The elbow plot of the sum of squared distances for different k clusters from a) CMIP5 and b) CMIP6 factors.

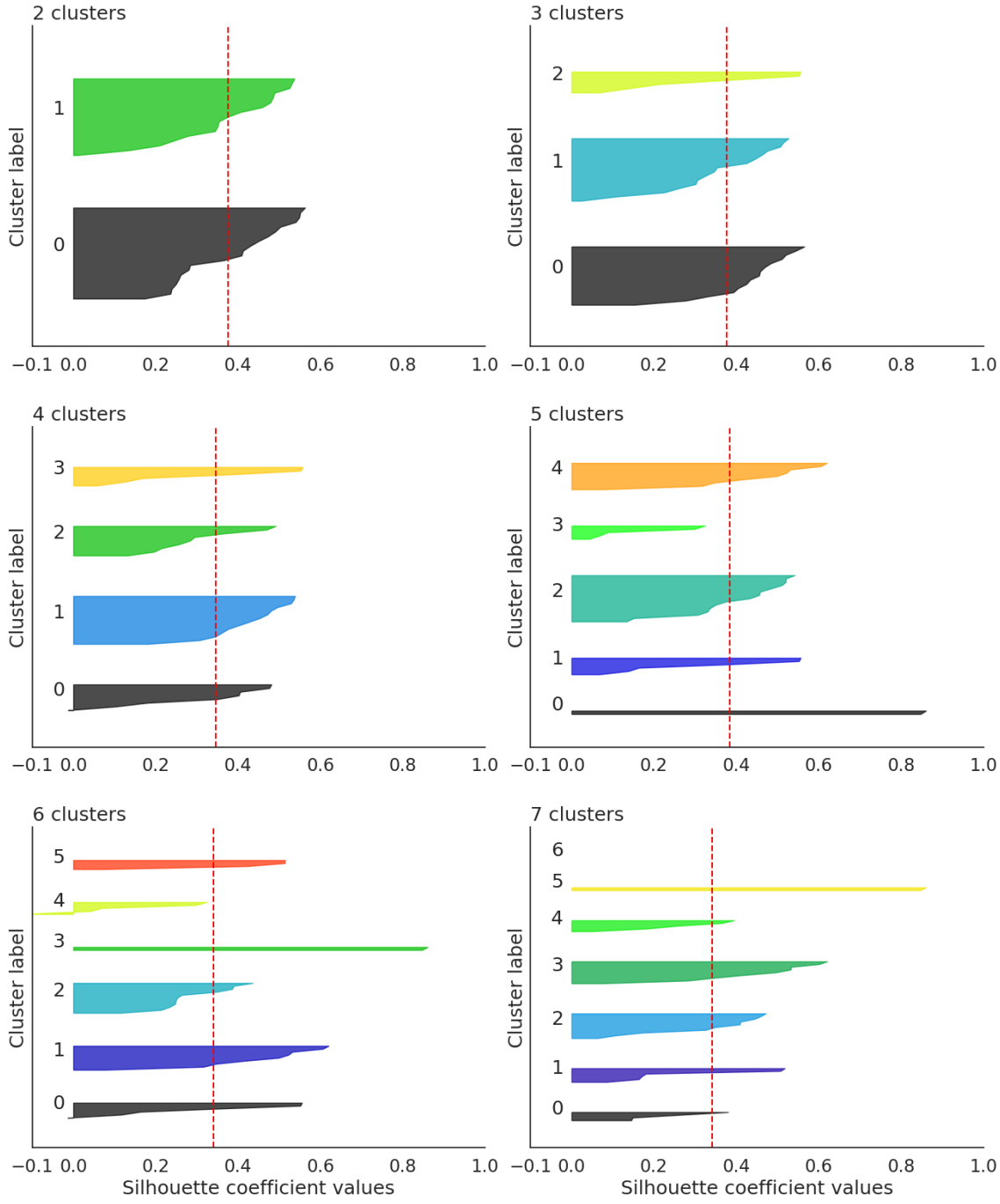

Figure 2.5: Silhouette analysis from CMIP5 factors considering different k clusters. Red dashed lines represent the average silhouette coefficient of the set of k clusters.

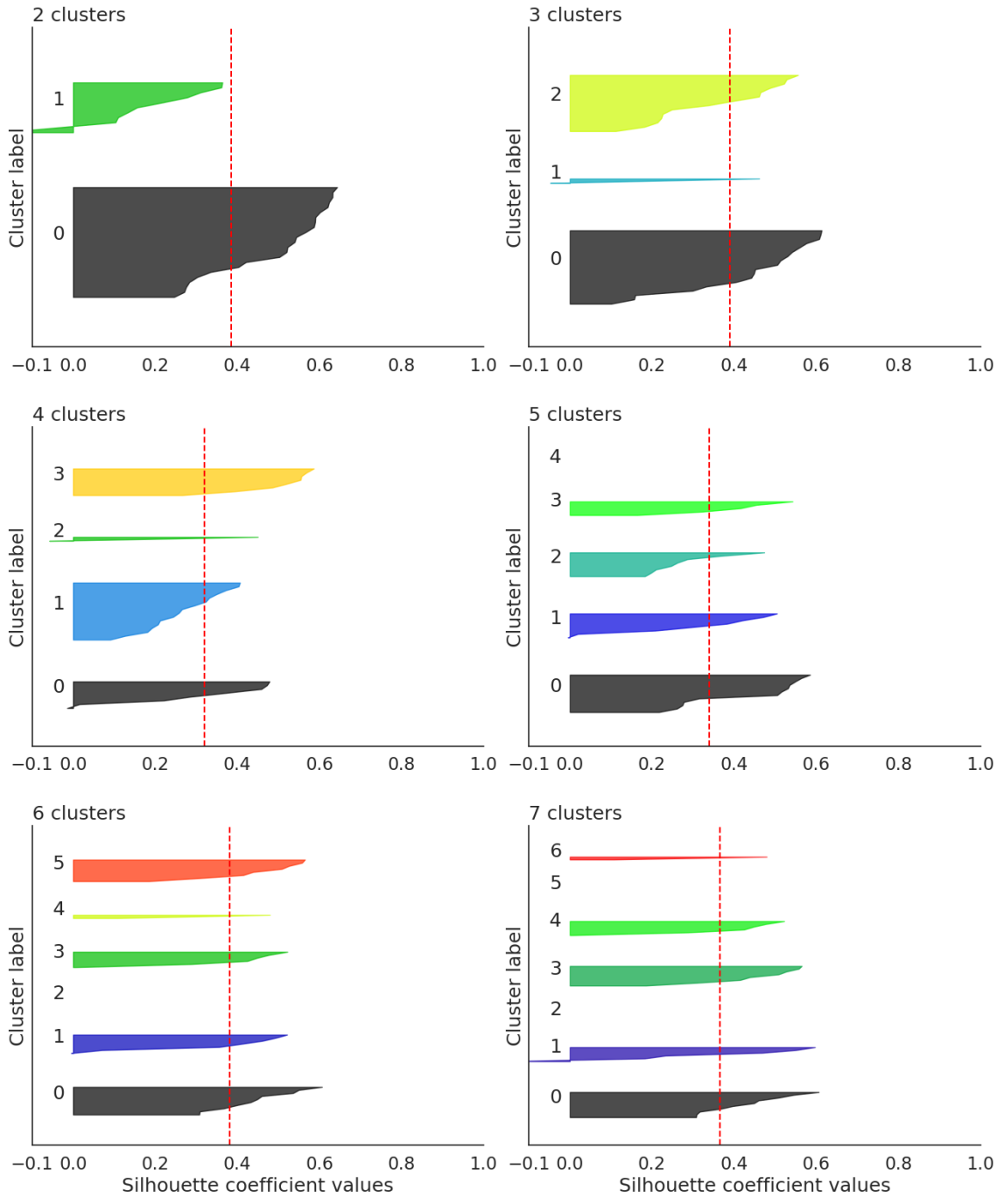

Figure 2.6: As in Figure 2.5 but for the factor of CMIP6 models.

optimal k of 3 or 4 clusters; however, k=4 gets a more uniform size distribution of the silhouette of the clusters, in comparison to what is obtained with 3 clusters.

Considering this analysis, we use k=4 clusters for both CMIP5 and CMIP6 models. The left panel of Figure 2.7 shows the grouping of the CMIP5 and CMIP6 models after performing a cluster analysis with the Ward's distance method. Additionally, the right panel in Figure 2.7 shows the scatter plots of the three factors that represent 77% of the total variance in CMIP5, while they contain 91% of the original variance in CMIP6.

We named the CMIP5 and CMIP6 clusters considered Group 1 to Group 4, according to the grouping given by the method. The number of models included in each group contrasts in both CMIP phases: in CMIP5, 18 models are included in Group 1, 11 in Group 2, and 4 in Group 3 and Group 4. In contrast, in CMIP6, Group 1 contains 19 models, Group 2 contains 6 models, Group 3 contains 1 model, and Group 4 contains 8 models. Some clusters tend to group models from the same institute, such as models from the Met Office, the NOAA Geophysical Fluid Dynamics Laboratory, and NASA, indicating the prevalence of similarities between models of the same institute, which suggests a similar performance in terms of their simulations of the main characteristics of the OLLJ. However, there are also noticeable contrasts between models of the same institute. For instance, the model MPI-ESM-1-2-HR from CMIP6 is not classified alongside other models, suggesting marked differences in the performance of this GCM compared to the others. The MPI-ESM-1-2-HR model participates in the High-Resolution Model Intercomparison Project (HighResMIP), which is based on GCMs with finer grid size. However, other models such as CMCC-CM2-HR4 are also included on the HighResMIP, and specifically, this model is classified next to several models of lower horizontal resolution. The above suggests that contrasts in horizontal grid size do not modulate the grouping of GCMs, and thus their skill in simulating the OLLJ.

It is not possible to relate the grid size of the different GCMs with their performance since models with finer and coarser horizontal resolutions are grouped in the same cluster. This pattern is shared for both CMIP phases. Tables S2.1 and S2.2

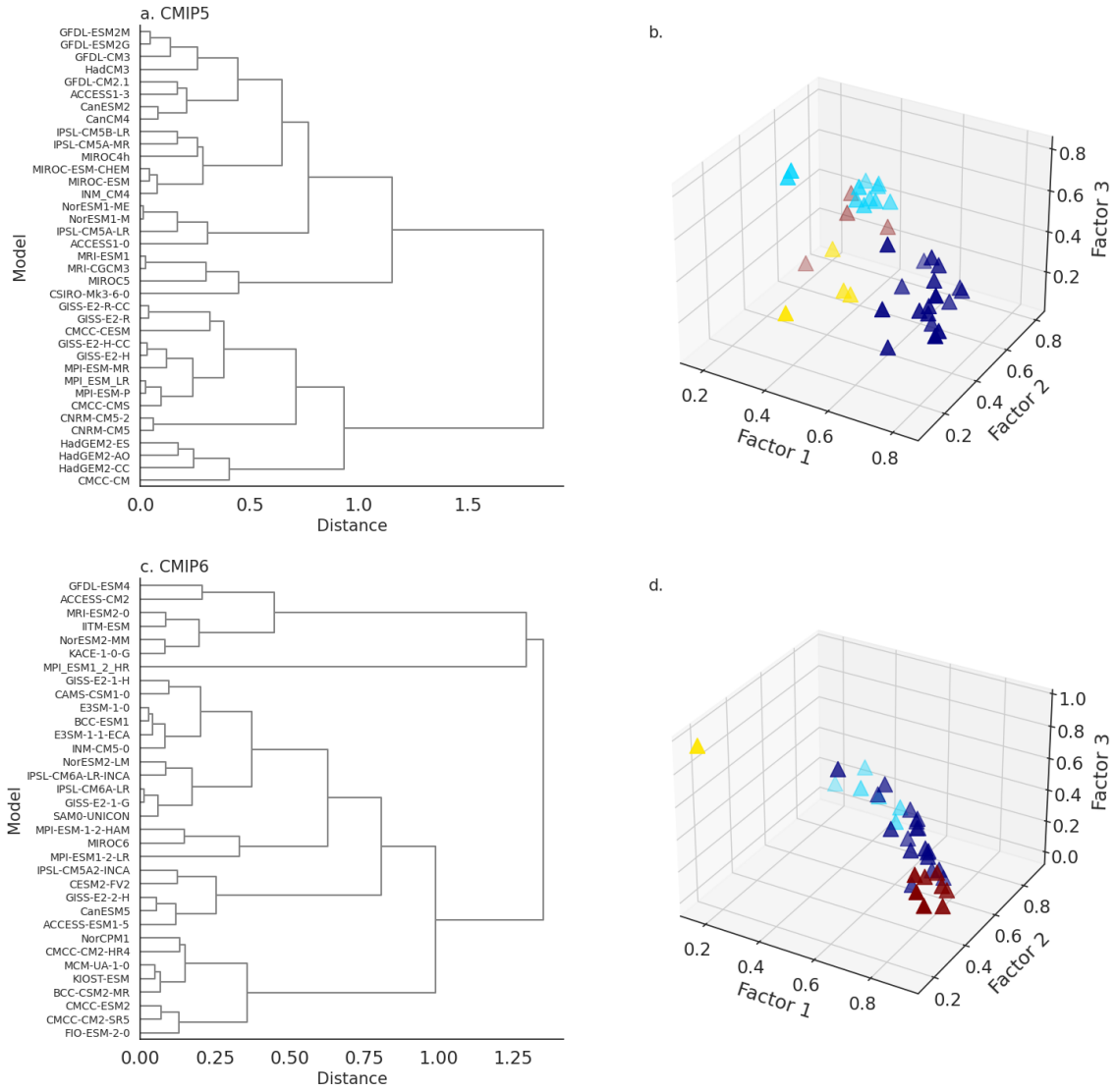

Figure 2.7: Dendrogram of the cluster analysis from CMIP5 and CMIP6 models (a, c), and the scatter plot of the three factors considered (b, d).

contain the CMIP5 and CMIP6 models included in each group, and following this classification, we evaluate how these GCMs represent the main characteristics of the OLLJ.

2.3.3 Performance of CMIP5/CMIP6 models in the simulation of the annual cycle of the Orinoco low-level jet

This subsection analyzes the simulation of the OLLJ index, the pattern of horizontal winds, and the vertical structure of the OLLJ from the multimodel mean of each group presented in Tables S.1 and S.2. It is relevant to notice that, as previously discussed, the classification of the available CMIP models is based on two performance metrics for each season of the year; however, we focus on the DJF season as it corresponds to the activation period of the OLLJ.

Figure 2.8 presents the simulation of the horizontal wind and the vertical structure of the OLLJ during DJF according to the four groups of CMIP5 models. Groups 1 and 2 (Figure 2.8a, c) do not exhibit an accurate simulation of the OLLJ activation, as they do not represent a clear low-level circulation through the Orinoco basin, which is strongly modulated by the regional topography. Regarding the vertical structure, Group 1 tends to misrepresent the location where the jet typically develops as well as its vertical structure, with no marked contrast between the flow associated with the OLLJ and the one from the wind field that enters the continent over Guiana (Figure 2.8b). On the other hand, Group 2 simulates the effect of the regional topography in the wind field but, similar to the estimates of Group 1, the vertical structure of the jet is not fully represented as it lacks a marked jet core (Figure 2.8d). Group 3 simulates the curving of the wind field between the Los Andes mountain range and the Guiana Highlands, which is an outstanding feature of the OLLJ during its activation period (Figure 2.8 e). In the cross-section shown in Figure 2.8f, this cluster represents the strengthening of the OLLJ at lower pressure levels; however, it tends to locate the jet to the west of its climatological position with high wind velocities at the east of the Guiana Highlands. Finally, Group 4 can simulate the activation of

the OLLJ in the Orinoco basin and the vertical structure of the jet, with a defined core of higher 850hPa wind velocities between 73°W and 69°W, differentiating the jet from the wind circulation through the atmospheric column (Figure 2.8g, h).

The simulated fields show that the CMIP5 GCMs tend to underestimate the wind magnitude reached by the OLLJ during its activation period and overestimate the wind field around the OLLJ corridor, suggesting the simulation of a weaker jet by the CMIP5 clusters considered (Figure S2.1). The above does not suggest that all CMIP5 models simulate a weaker OLLJ, but the broad agreement among models suggests the underestimation of the jet intensity by this generation of GCMs.

Regarding the OLLJ index estimated from the meridional wind by the CMIP5 clusters (Figure 2.9), Groups 1, 2, and 3 underestimate the wind speed during DJF. In contrast, Group 4 has a more accurate representation of the jet intensity in that period. All groups simulate the jet minimum intensity in June and July, while the wind field reaches its minimum in August in ERA5. Group 4 shows higher consistency with the reference ERA5 estimates, suggesting a more adequate representation of the seasonal fluctuation of the wind field over the region. Even though Groups 1, 2, and 3 overestimate the OLLJ index during SON, this pattern is more marked in Group 1, which may be due to the lack of differentiation of the OLLJ from the surrounding surface circulation over northern South America depicted by this group (Figure 2.8a). Group 2 shows greater differences with ERA5 during JJA, which may be influenced by the weaker-than-normal OLLJ simulated by this cluster (Figures 2.8b and 2.9). It is relevant to highlight the spread of each cluster, as Group 1 exhibits the most prominent differences among the estimates from each model, particularly during SON. On the contrary, the spread of Group 4 is the lowest among the clusters, indicating more consistency and similarities among the models included in this group. This suggests that Group 4 contains models with a better simulation of the spatial and temporal characteristics of the OLLJ, while Group 1 performance is the lowest among the CMIP5 groups.

Table 2.2 presents the PCC and RMSE metrics of the horizontal wind fields and the jet vertical structure for DJF and the monthly OLLJ index for the four CMIP5

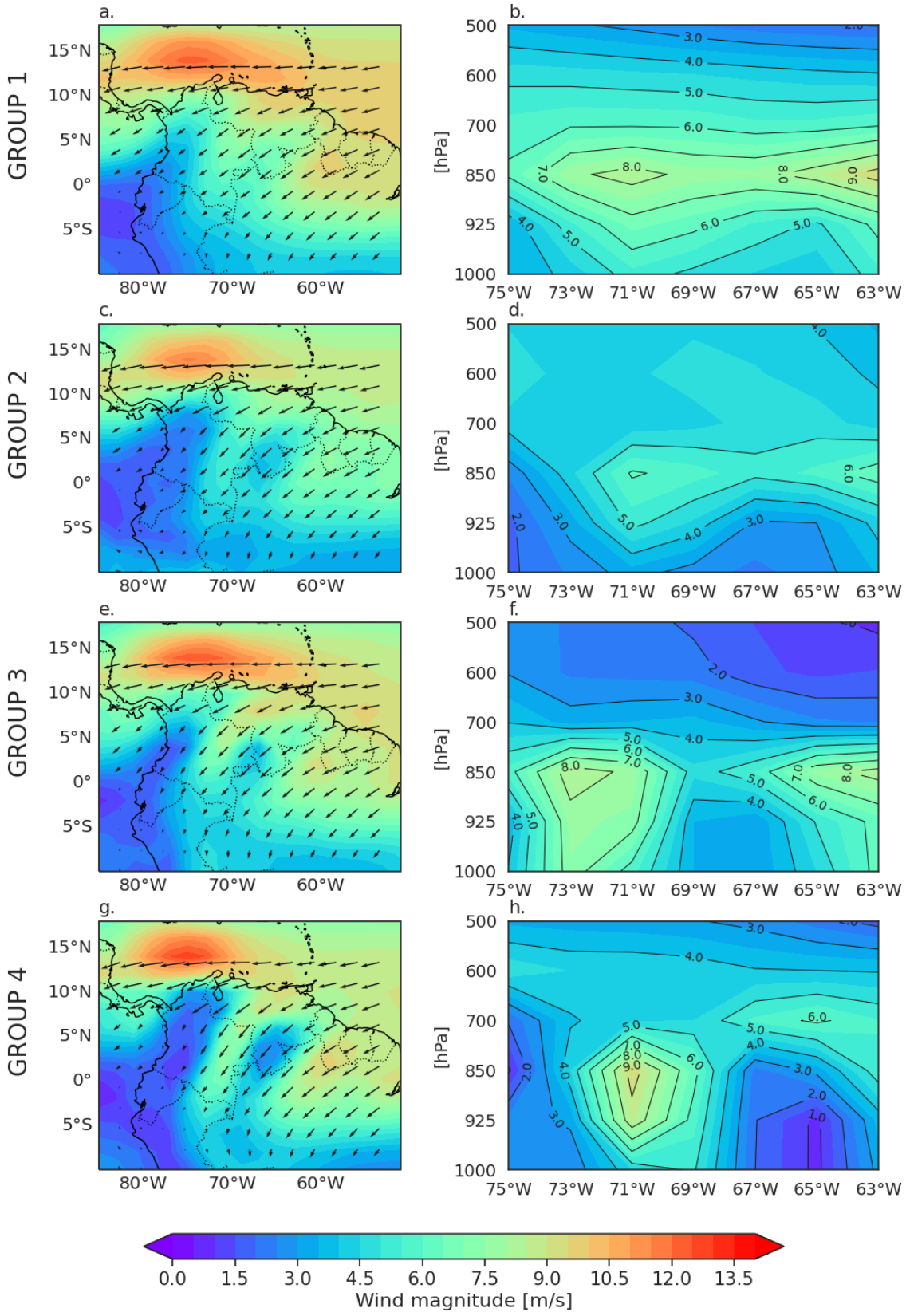

Figure 2.8: Multimodel mean of the horizontal winds between 825 and 950 hPa and the vertical structure of the OLLJ during 1979-2005 from the four clusters of CMIP5 models considered (Table S2.1).

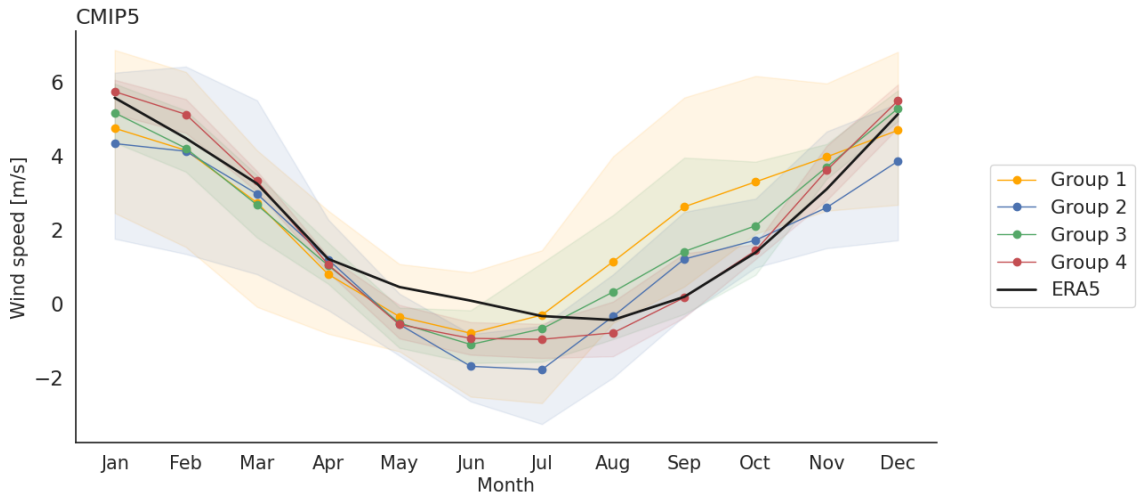

Figure 2.9: Multimodel means of the OLLJ index from meridional wind at region C3.4 (Figure 2.1) for the four clusters of CMIP5 models considered (Table S2.1). Shading corresponds to the spread of the set of models included in each cluster.

clusters considered. The bold metrics represent the best value of the metric in each characteristic (lower RMSE and higher PCC). As indicated by Figures 2.8 and 2.9, Group 1 tends to have the worst representation of the seasonal characteristics of the OLLJ as it exhibits the lowest PCC and highest RMSE among almost all characteristics. On the contrary, the performance of Group 4 is the best among CMIP5 clusters, with an outstanding simulation of the main features of the OLLJ in comparison to the other groups. Groups 2 and 3 exhibit an intermediate performance of these characteristics among the CMIP5 clusters.

Regarding the performance of the CMIP6 models, Figure 2.10 shows the multimodel mean of the wind field and the cross-section for the set of GCMs in each cluster. Different from what is observed for the CMIP5 clusters, all groups in CMIP6 simulate both the change in direction of the surface wind field modulated by the topography and the formation of the jet core at lower pressure levels. The above contrasts with the estimates from CMIP5 models, which show marked differences in the performance of the different clusters. In general, these results suggest that CMIP6 models tend to simulate the activation of the jet in DJF, as they exhibit the main spatial features of the jet, distinguishing this low-level circulation over northern South America. As all CMIP6 clusters can simulate the OLLJ, we focus on how well each group performs. Groups 1 and 4 reach lower wind magnitudes at the jet exit and, even

Table 2.2: Performance metrics of the multimodel mean of the four clusters of the CMIP5 models considered, in terms of their simulation of the main characteristics of the OLLJ (Table S2.1). Metrics in bold correspond to the best value of the metric: higher PCC and lower RMSE.

	Group 1	**Group 2**	**Group 3**	**Group 4**
Horizontal Wind PCC	0.86	0.87	**0.9046**	0.90
Horizontal Wind RMSE	2.03	1.44	1.52	**1.35**
Vertical structure PCC	0.59	0.70	0.33	**0.78**
Vertical structure RMSE	2.61	1.74	2.58	**1.45**
OLLJ index PCC	0.85	0.93	0.94	**0.99**
OLLJ index RMSE	1.14	0.96	0.71	**0.54**

though the cross-section for these groups shows the development of the jet core, its wind magnitude is surpassed by the wind field at the east of the Guiana Highlands (Figure 2.10b, h). On the other hand, Groups 2 and 3 simulate the jet location near 71°W, which tends to be consistent with ERA5 (Figure 2.10d, f). These groups distinguish the OLLJ in the Orinoco basin from the surface flow over the Guianas.

Differences between the estimates from the clusters and ERA5 indicate that CMIP6 clusters tend to underestimate the wind magnitude of the jet, indicating the simulation of a weaker jet by the CMIP6 GCMs (Figure S2.2). However, as these results focus on the multimodel mean, the pattern of underestimation of the wind intensity should not be generalized for all the CMIP6 models considered in this study.

The simulation of the temporal variations along the year of the OLLJ index is similar among CMIP6 clusters. Figure 2.11 presents the annual cycle of the OLLJ index. It can be noticed that the estimates from the CMIP6 groups are consistent among them and tend to be similar to ERA5, except in Group 3 during JJA. Groups 1, 2, and 4 maintain the overestimation of the wind speed from August to October. Also, all clusters simulate the period of minimum activity of the jet in June and July, similarly to the CMIP5 clusters. The spread of the models included in each group does not exhibit significant fluctuations throughout the year, and, in contrast to

the CMIP5 groups, it does not show marked differences among clusters. In general, CMIP6 clusters show small differences with ERA5 estimates, suggesting a better representation of the OLLJ index by CMIP6 models in comparison to CMIP5.

The performance metrics of the CMIP6 clusters for the main characteristics of the OLLJ suggest that Groups 2 and 3 are the best among all clusters since they exhibit higher PCC and lower RMSE for all the characteristics analyzed here (Table 2.3). It is relevant to notice that clusters may have a high performance either in the spatial pattern or the error of the estimates of a particular characteristic but can have an inaccurate simulation of other OLLJ features. For instance, Groups 1 and 4 misrepresent the vertical structure of the jet (PCC of 0.52 and 0.56, respectively, and RMSE of 2.03 for both Groups) but are more accurate in the simulation of the annual variation of the wind field at the jet exit region (PCC of 0.96 and 0.89, and RMSE of 0.66 and 0.99, respectively), supporting the importance of the analysis of different characteristics of this LLJ when analyzing CMIP models.

These results confirm that there are more considerable differences in the performance of the simulation of the seasonal characteristics of the OLLJ among CMIP5 models than among CMIP6, resulting in the classification of the set of CMIP5 GCMs into groups with marked differences among them. On the contrary, most of the CMIP6 models can simulate the temporal and spatial features of the jet, and thus there is not much contrast among the performance of the clusters. The above suggests the improvement of CMIP6 models from the previous CMIP phase in terms of the simulation of the observed features of the low-level horizontal wind field in northern South America. On the other hand, this initial evaluation suggests that the representation of the regional topography by GCMs is relevant when simulating the OLLJ as a distinguishable feature of the surface circulation in northern South America.

According to the literature, CMIP5 and CMIP6 models differ not only on their spatial resolution but also on their response to the aerosol concentration in the atmosphere, among other factors (e.g., Grose et al., 2020; Zelinka et al., 2020; Zhao et al., 2022). As some CMIP6 models maintain coarser spatial resolutions, similar to their previous versions (for instance, INM-CM4.0 of CMIP5 and INM-CM5.0 of

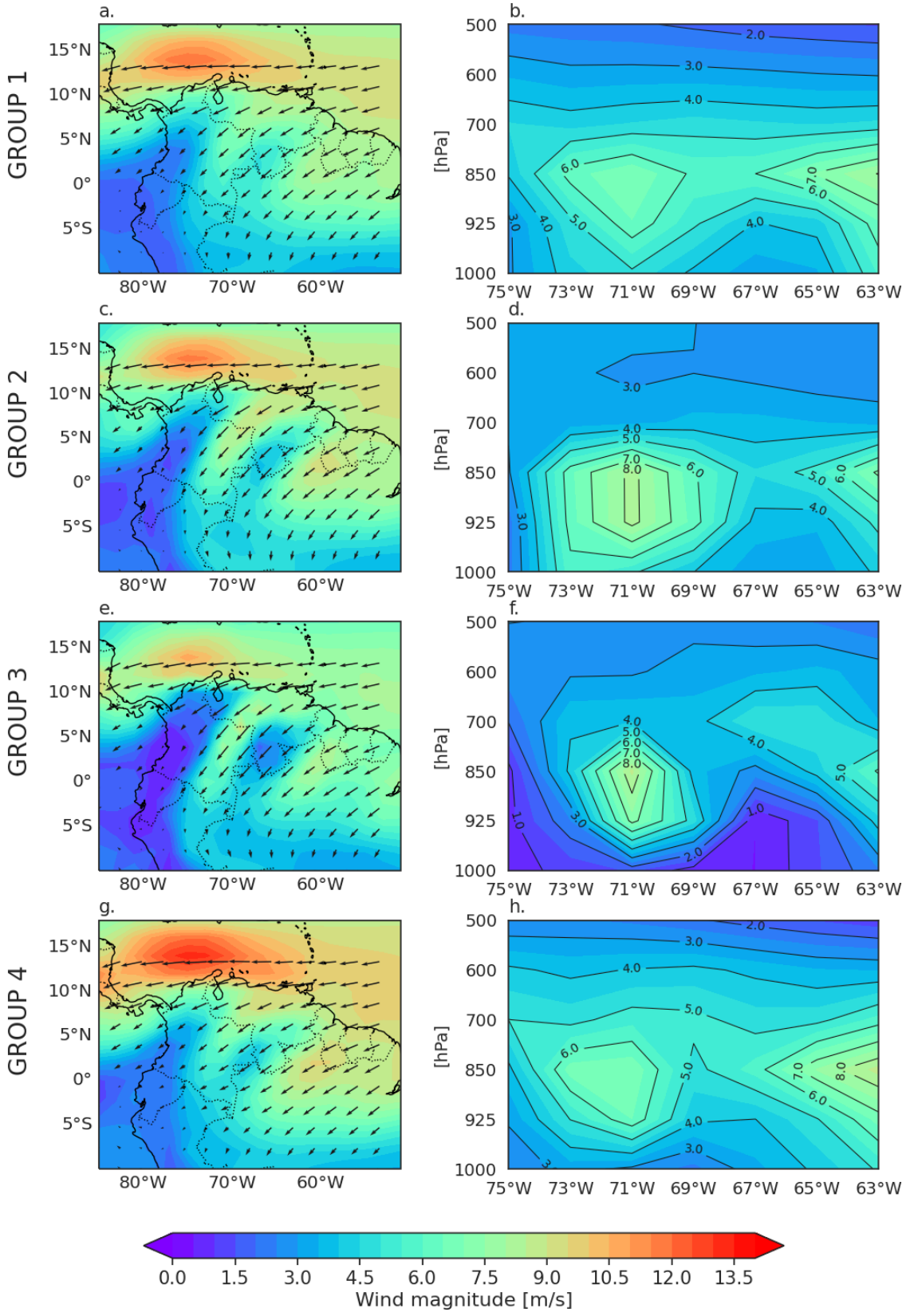

Figure 2.10: As in Figure 2.8 but for the four clusters of the CMIP6 models (Table S2.2) during 1979-2014.

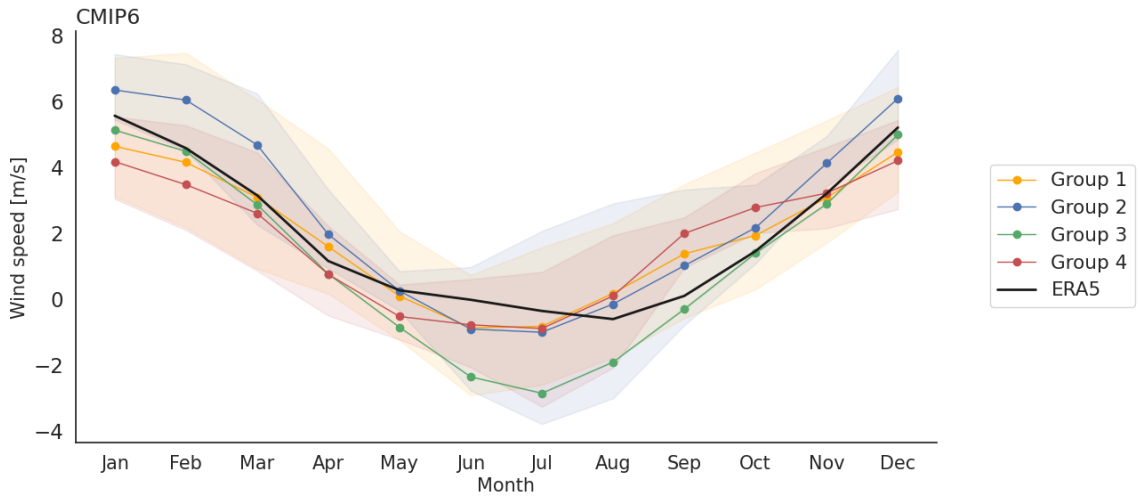

Figure 2.11: As in Figure 2.9 but for the four clusters of the CMIP6 models (Table S2.2).

CMIP6), the observed improvements in the simulation of the OLLJ should not be only restricted to a finer grid size of the model. However, it is relevant to evaluate if this better performance of the CMIP6 models is related to how the GCMs represent the regional patterns that allow the activation and strengthening of the OLLJ. This connection will be further evaluated in section 2.3.4.

Table 2.3: As for Table 2.2 but for the clusters of the CMIP6 models (Table S2.2). Metrics in bold correspond to the best value of the metric: higher PCC and lower RMSE.

	Group 1	**Group 2**	**Group 3**	**Group 4**
Horizontal Wind PCC	0.88	**0.92**	0.91	0.88
Horizontal Wind RMSE	1.54	**1.25**	1.28	1.94
Vertical structure PCC	0.52	0.64	**0.85**	0.56
Vertical structure RMSE	2.03	1.77	**1.13**	2.03
OLLJ index PCC	0.96	**0.98**	0.97	0.89
OLLJ index RMSE	**0.66**	0.92	1.13	0.99

2.3.4 Links between the gradients of mean sea level pressure, surface sensible heat flux and near-surface air temperature and the simulation of the Orinoco low-level jet

Multiple studies state that the meridional pressure gradients between the North Atlantic Subtropical High (NASH) and the Intertropical Convergence Zone (ITCZ) modulate the strengthening of the northeastern trade winds and their southward shift, which in turn, enables the activation of the OLLJ (Builes-Jaramillo et al., 2022b; Martínez et al., 2022). Due to the role of these gradients in the activation of the jet, it is relevant to assess their simulation from GCMs, as it allows to relate variations in the representation of these patterns to the simulation of the OLLJ.

The climatology of MSLP and near-surface air temperature during DJF simulated by clusters (a, b, d, e, g, h, j, k of Figures 2.12 and 2.13) show that models capture the gradients of MSLP and temperature between the tropical North Atlantic (orange rectangle) and the Andes-Amazon transition region (blue rectangle), with higher (lower) MSLP and lower (higher) near-surface air temperature over the tropical North Atlantic (transition region). These patterns are consistent with the strengthening of the wind field and its consequent orientation into the continent. All groups simulate those patterns, independently of their performance in the representation of the main features of the OLLJ, suggesting some accuracy in the simulation of the seasonal characteristics, in terms of the location of higher and lower MSLP centers and their coupling with the spatial distribution of near-surface air temperature.

Figure 2.14 shows the horizontal gradients of MSLP and near-surface air temperature between the Tropical North Atlantic and the Andes-Amazon transition region (orange and blue rectangles in Figure 2.1, respectively) estimated from the CMIP5 clusters. Solid dotted lines represent the best group identified in subsection 2.3.3 (Group 4) and dashed-dotted lines represent the worst group among all CMIP5 clusters (Group 1). All CMIP5 groups simulate higher MSLP gradients throughout the year than the estimates from ERA5 (black line). The above indicates that

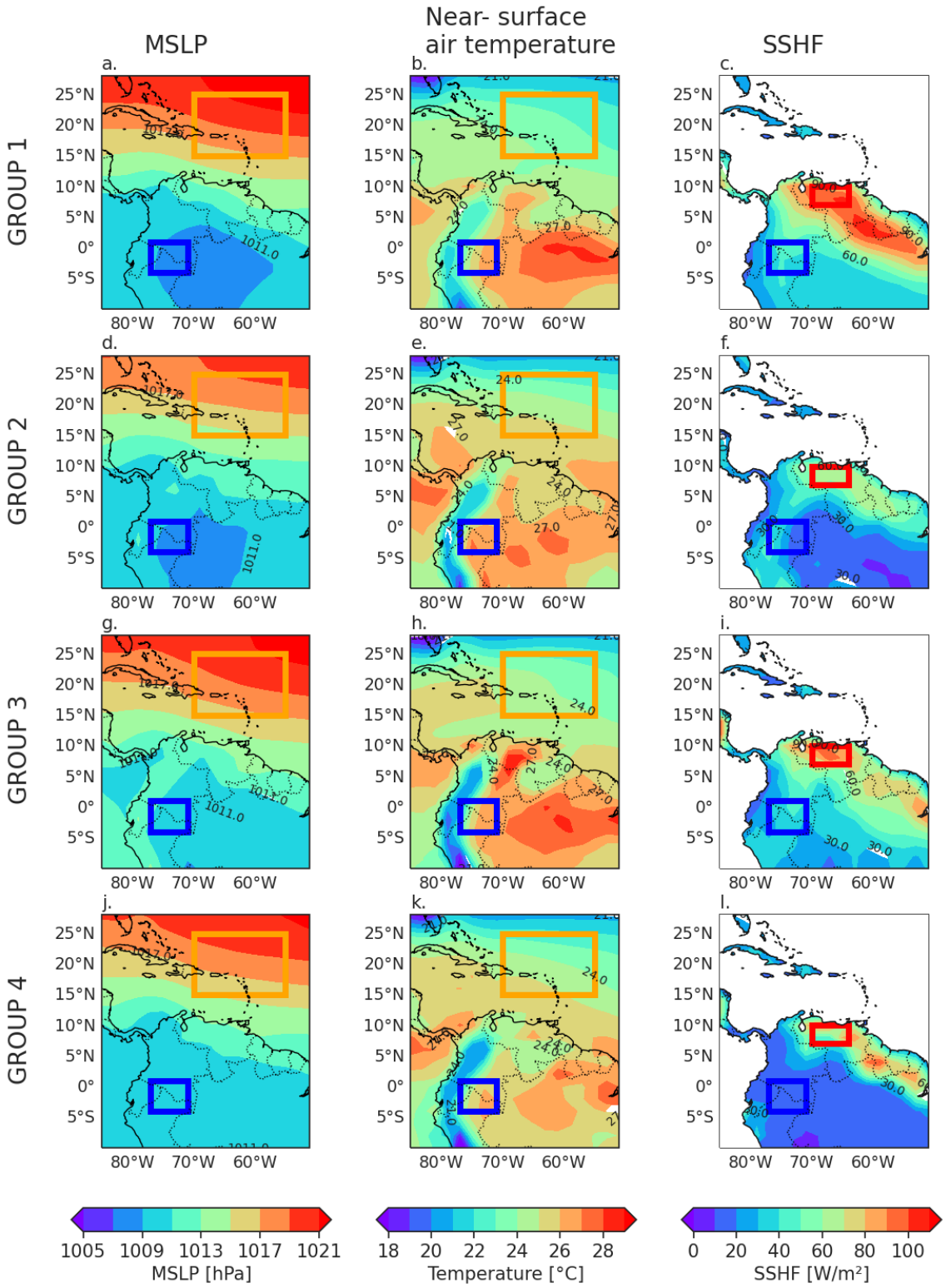

Figure 2.12: Climatology of MSLP (a, d, g, j), near-surface air temperature (b, e, h, k) and SSHF (c, f, i ,l) for DJF from CMIP5 models during 1979-2005. Rectangles represent the regions used for the estimation of the horizontal gradients: Tropical North Atlantic (orange), Orinoco (red), and Andes-Amazon transition (blue).

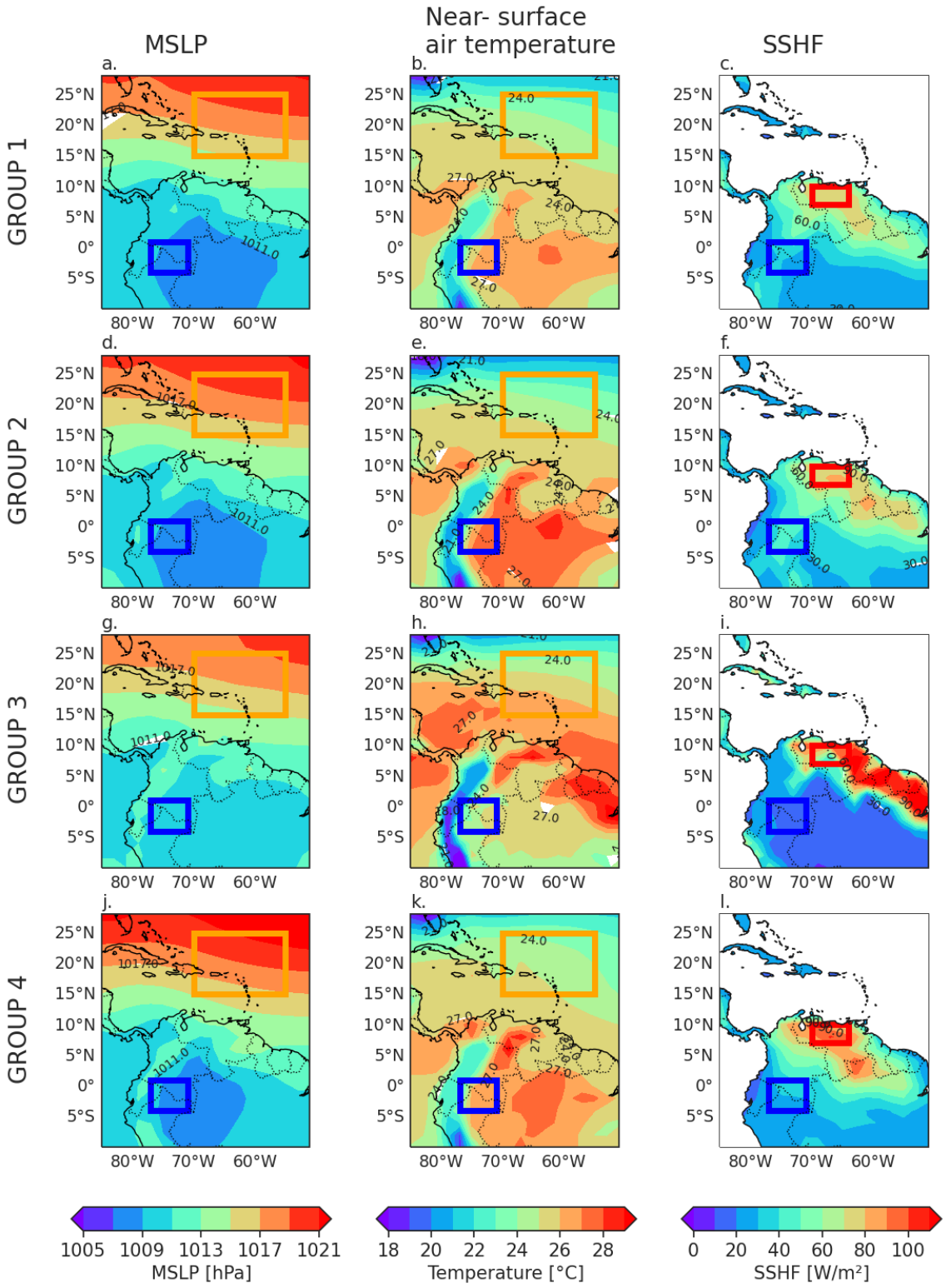

Figure 2.13: As in Figure 2.12 but for the CMIP6 models.

CMIP5 models represent higher MSLP over the Tropical North Atlantic during the year than the reference dataset, as it can be seen for DJF from the biases of the MSLP and near-surface air temperature fields (Figure S2.3). Among all the CMIP5 clusters, Group 1 exhibits the lowest correlation and higher RMSE (0.89 and 3.62, respectively) while Group 4 has the highest correlation (0.98) and one of the lowest RMSE (1.22). On the other hand, the simulated temperature gradients by the CMIP5 clusters are negative during DJF, suggesting that the Tropical North Atlantic reaches lower near-surface temperatures during this period, which is consistent with the meridional migration of the ITCZ associated with higher surface temperatures over the South American landmass. Group 4, which exhibits the best performance in the simulation of the OLLJ (Table 2.2), reaches the highest correlation and the lowest RMSE among the clusters (0.98 and 0.35). Group 1, identified as the worst cluster of CMIP5 models (Table 2.2), has a high correlation with the reference dataset (0.93) but does not exhibit the highest RMSE.

The MSLP and temperature gradients from the CMIP6 clusters (Figure 2.15) are similar to those obtained from CMIP5. Group 3 has more similar values to ERA5 in comparison to other groups as it does not overestimate the MSLP gradients throughout the year. Also, Group 3 is the only cluster that simulates higher air temperatures in the Tropical North Atlantic during DJF (positive temperature gradient). It is relevant to note that this group contains a single model (MPI-ESM1-2-HR), so it may explain the contrasting results with the other groups.

When considering the CMIP6 models, the clusters do not show marked differences in their performance in the simulation of the OLLJ. Once again, the differences among clusters in the representation of the MSLP and air temperature gradients are not clear. Groups 2 and 3 have the highest correlation with ERA5 for both gradients but they do not exhibit the lowest RMSE in all cases. On the other hand, Group 4 has the most prominent differences with ERA5 for the MSLP gradient (correlation of 0.88 and RMSE of 3.62) but it improves its performance to simulate the near-surface temperature gradient (correlation of 0.94 and RMSE of 0.96).

As discussed in section 2.3.3, the performance of the CMIP5 models may have a link

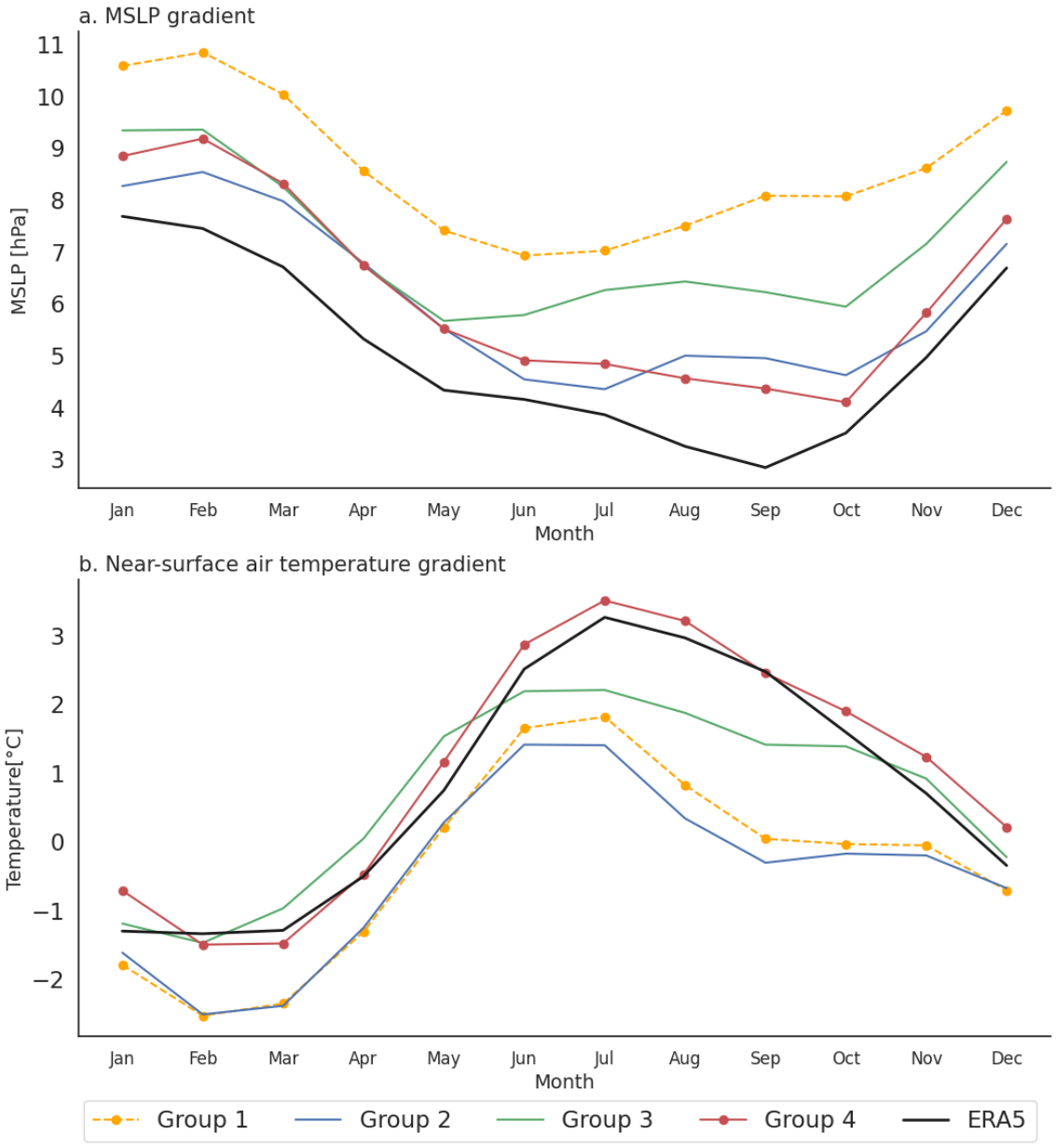

Figure 2.14: Annual cycle of the horizontal gradients of (a) MSLP and (b) near-surface temperature from the four clusters of CMIP5 models (Table S2.1). The gradients are calculated as the difference between the Tropical North Atlantic and the Andes-Amazon transition region during 1979-2005. The solid dotted line represents the best CMIP5 cluster (Group 4), and the dashed-dotted line represents the worst group (Group 1).

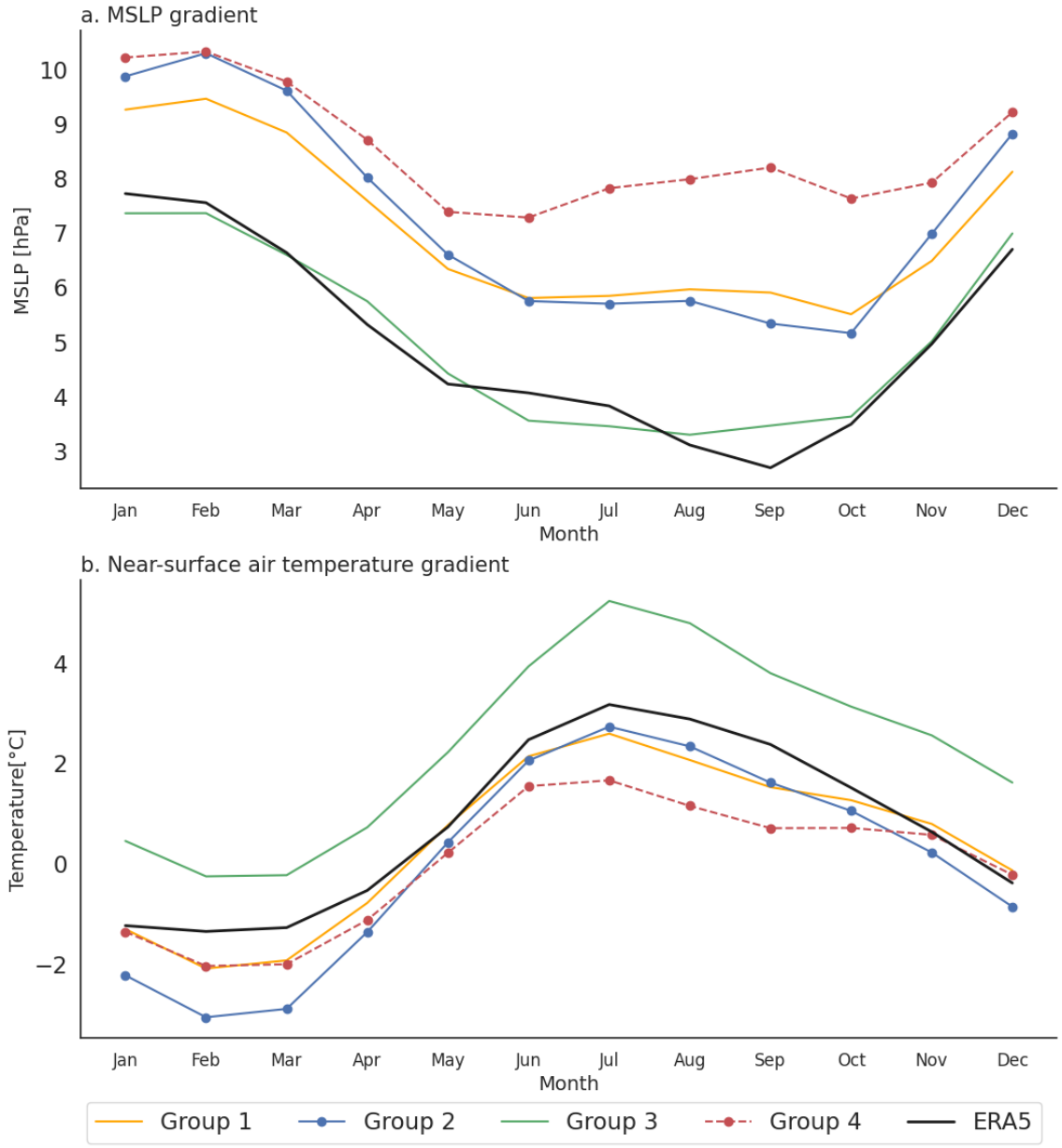

Figure 2.15: As in Figure 2.14 but for the four CMIP6 clusters considered (Table S2.2). The solid dotted line represents the best CMIP6 group (Group 2), and the dashed-dotted line represents the worst group (Group 4).

with their simulation of the activation mechanisms of the jet, as Group 4 tends to exhibit a better simulation of the main OLLJ characteristics and the MSLP gradients between the Tropical North Atlantic and the Andes-Amazon transition region. However, this linkage is not so clear for the CMIP6 models since there is no specific group with an outstanding representation of these gradients and the main features of the jet. The clusters of CMIP5 and CMIP6 models can simulate the strengthening of the wind field into northern South America during DJF associated with the OLLJ, however it is relevant to consider other factors that may influence the model performance in the simulation of this jet. For instance, the representation of the regional topography can have an essential role in how GCMs represent this LLJ, such as the simulation of the OLLJ index in region C3.4, mainly when the spatial features of the OLLJ are strongly influenced by the Andes mountain range and the Guiana Highlands.

Chapter 1 links the OLLJ intensity with regional gradients of MSLP, near-surface air temperature, and sensible surface heat flux (SSHF) between the entrance and exit regions of the jet. As these regional gradients influence the strengthening of the OLLJ, it is relevant to evaluate how they are represented in the GCM simulations, focusing on the northern (Orinoco) and southern (Andes-Amazon transition) regions of the jet corridor (red and blue rectangles in Figure 2.1, respectively). As discussed in Chapter 1 (section 1.3.5), the activation of the jet is accompanied by positive MSLP, air temperature, and SSHF gradients, suggesting higher values of the variables at the jet entrance. On the other hand, a more intense jet is associated with higher MSLP and lower SSHF and air temperature gradients, suggesting that a lower SSHF at the jet entrance is linked to a decrease in air temperature and a higher MSLP in the Orinoco region. Hence, it is important to analyze the performance of the GCMs simulating these variables.

The multimodel mean of the SSHF climatology (Figures 2.12c, f, i, l , 2.13c, f, i, l) indicates that CMIP5 and CMIP6 models simulate higher SSHF over northeastern South America and lower values of SSHF on the transition region, which is consistent with higher (lower) near-surface temperatures over the Orinoco (Andes-Amazon transition). As stated previously, those differences are strongly influenced by the

climatological features of those regions as the Orinoco exhibits a drier climate that modulates a more arid regime over the region, in comparison to the Andes-Amazon transition that represents a shift into a more humid regime.

When assessing the regional pattern of MSLP, near-surface air temperature, and SSHF during DJF, following Martínez et al. (2022), our results suggest that GCMs from CMIP5 and CMIP6 accompany the activation and intensification of the OLLJ alongside higher SSHF and MSLP over the Orinoco region (red square in Figures 2.12 and 2.13) and lower SSHF and MSLP on the Andes-Amazon transition region (blue square in Figures 2.12 and 2.13), which explains the direction of the low-level wind flow to the Amazon in DJF. On the other hand, the climatological simulation by GCMs exhibits the most prominent differences among the gradients, as some groups locate higher near-surface temperatures over the Orinoco (e.g., Figure 2.12h, Figure 2.13h) while other groups do not simulate marked differences between the Orinoco and the transition region (e.g., Figure 2.12e, Figure 2.13b). This suggests that some models do not adequately simulate the regional contrasts of temperature between the Orinoco and the transition regions. Therefore, the greatest differences in near-surface temperature are obtained between the ocean and the land surface.

Section 1.3.5 analyzes the response of the jet intensity and the regional gradients of MSLP, SSHF, and near-surface air temperature to the occurrence of higher-than-normal and lower-than-normal wind magnitudes at the OLLJ exit during DJF. To assess if the set of models used in this study capture the relationship of the OLLJ intensity with variations in the regional gradients of MSLP, near-surface air temperature, and SSHF, Figures 2.16 to 2.19 show the composites of the anomalies of MSLP (panels a, d, g, j), near-surface air temperature (panels b, e, h, k) and SSHF (panels c, f, i, l) during strong and weak OLLJ events for CMIP5 and CMIP6 models. The composites are calculated considering the stronger and weaker OLLJ events during the DJF season, selected for each model from its long-term monthly anomalies of the OLLJ index. The results suggest that strong jet events (Figures 2.16 and 2.18) are associated with higher MSLP and lower SSHF and near-surface air temperature over the Orinoco, while the opposite occurs during weak jet events (Figures 2.17 and

2.19), in which the Orinoco region exhibits negative MSLP anomalies and positive near-surface air temperature and SSHF anomalies.

During strong OLLJ events (Figures 2.16 and 2.18), the anomalies over the transition region (blue rectangle) are positive, suggesting that GCMs in CMIP5 and CMIP6 simulate rises in the SSHF over the Andes-Amazon alongside decreases over the Orinoco. Even though the fluctuations of MSLP and near-surface air temperature in the transition region also indicate lower MSLP and higher air temperature during strong OLLJ events, the magnitude of those anomalies is smaller. The above might suggest that during strong OLLJ events in the transition region, SSHF is the variable that experiences major fluctuations while MSLP and near-surface air temperature do not evidence a significant deviation from their climatology. These contrasts are not observed during weaker OLLJ events when fluctuations in the Orinoco are more predominant.

The Orinoco experiences the greatest fluctuations during strong and weak OLLJ events, therefore interannual variations of the climatic conditions over this region strongly influence the features of the LLJ as those variations modulate changes in the regional gradients between the northern and southern parts of the jet corridor. More generally, high SSHF over the Orinoco rises near-surface air temperature, that in turn locally decreases the MSLP, weakening the regional gradient of MSLP through the Orinoco basin and reducing the intensity of the OLLJ. On the contrary, decreasing SSHF in the Orinoco reduces near-surface air temperature while MSLP increases, strengthening the regional gradient, and therefore the low-level wind flow related to the OLLJ.

The relationship between the OLLJ intensity and fluctuation in regional gradients is observed for both CMIP5 and CMIP6 models, independently of their performance of the OLLJ main features. The above suggests the robustness of the relationship between the jet strengthening and the gradients of MSLP, SSHF, and near-surface air temperature between the Orinoco and the Andes-Amazon transition regions, which are strongly influenced by the fluxes from the land surface, as proposed by Martinez et al. (2022).

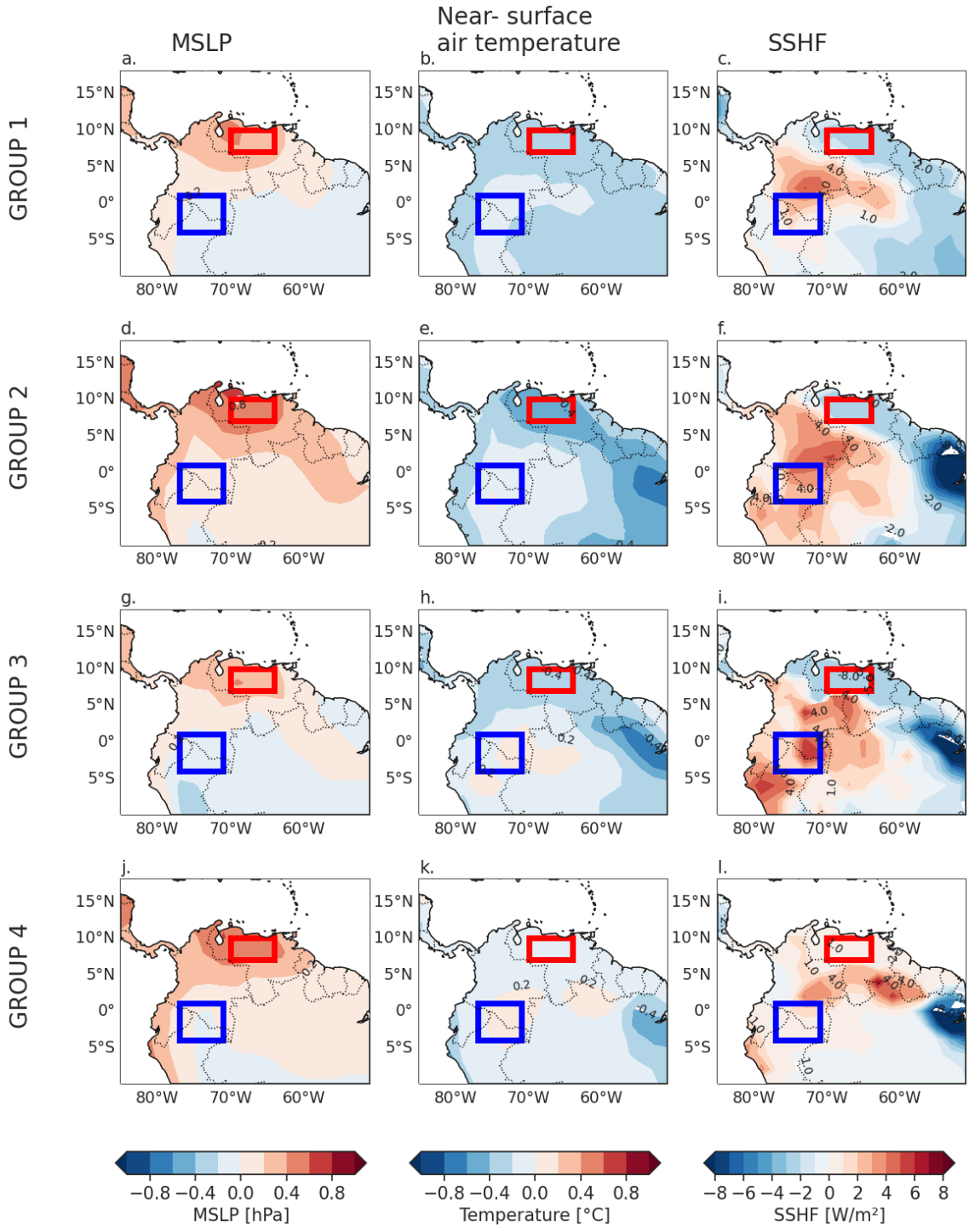

Figure 2.16: Composites of the anomalies of MSLP (a, d, g, j), near-surface air temperature (b, e, h, k), and SSHF (c, f, i, l) in DJF for the CMIP5 clusters during strong OLLJ events.

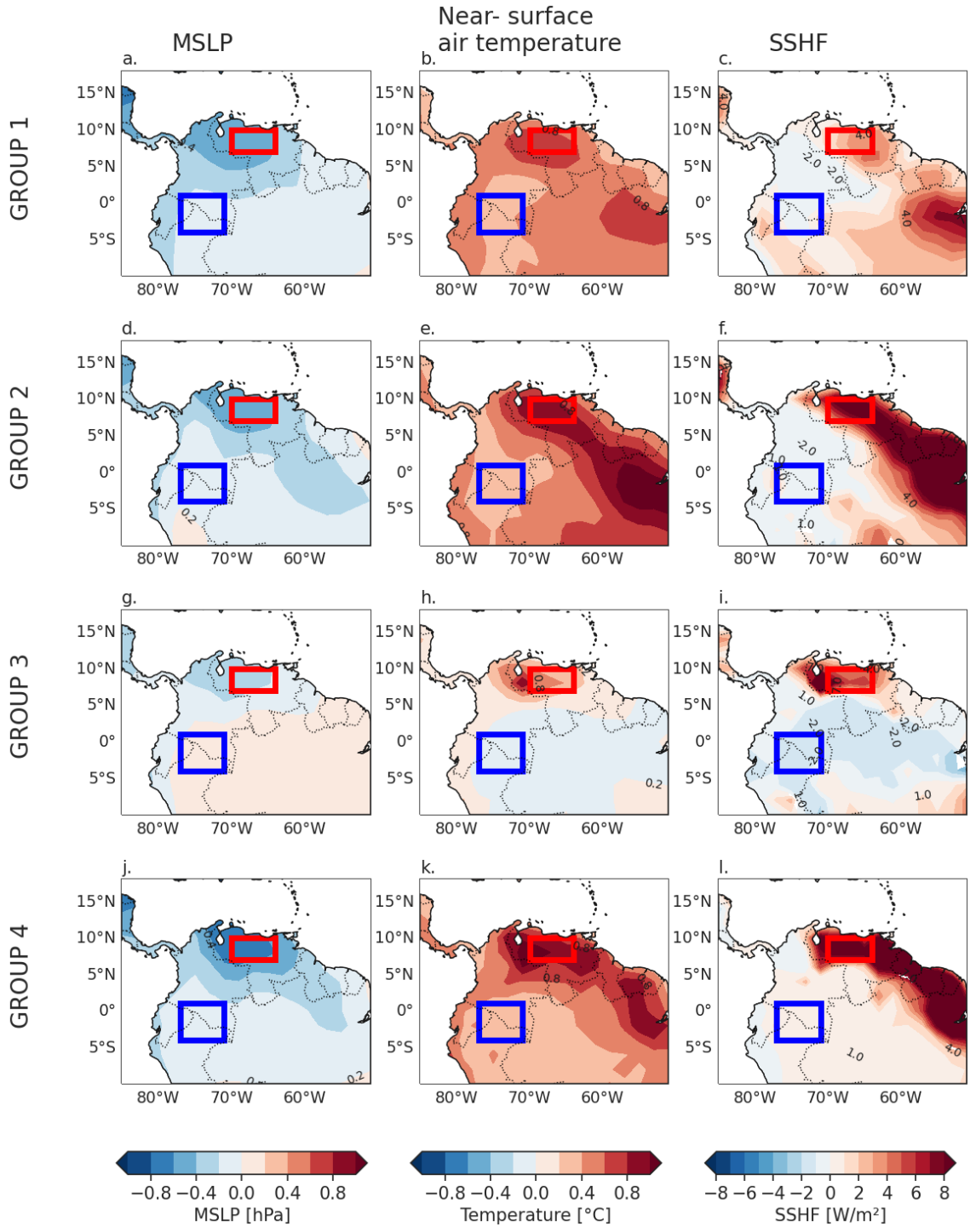

Figure 2.17: Composites of the anomalies of MSLP (a, d, g, j), near-surface air temperature (b, e, h, k), and SSHF (c, f, i, l) in DJF for the CMIP5 clusters during weak OLLJ events.

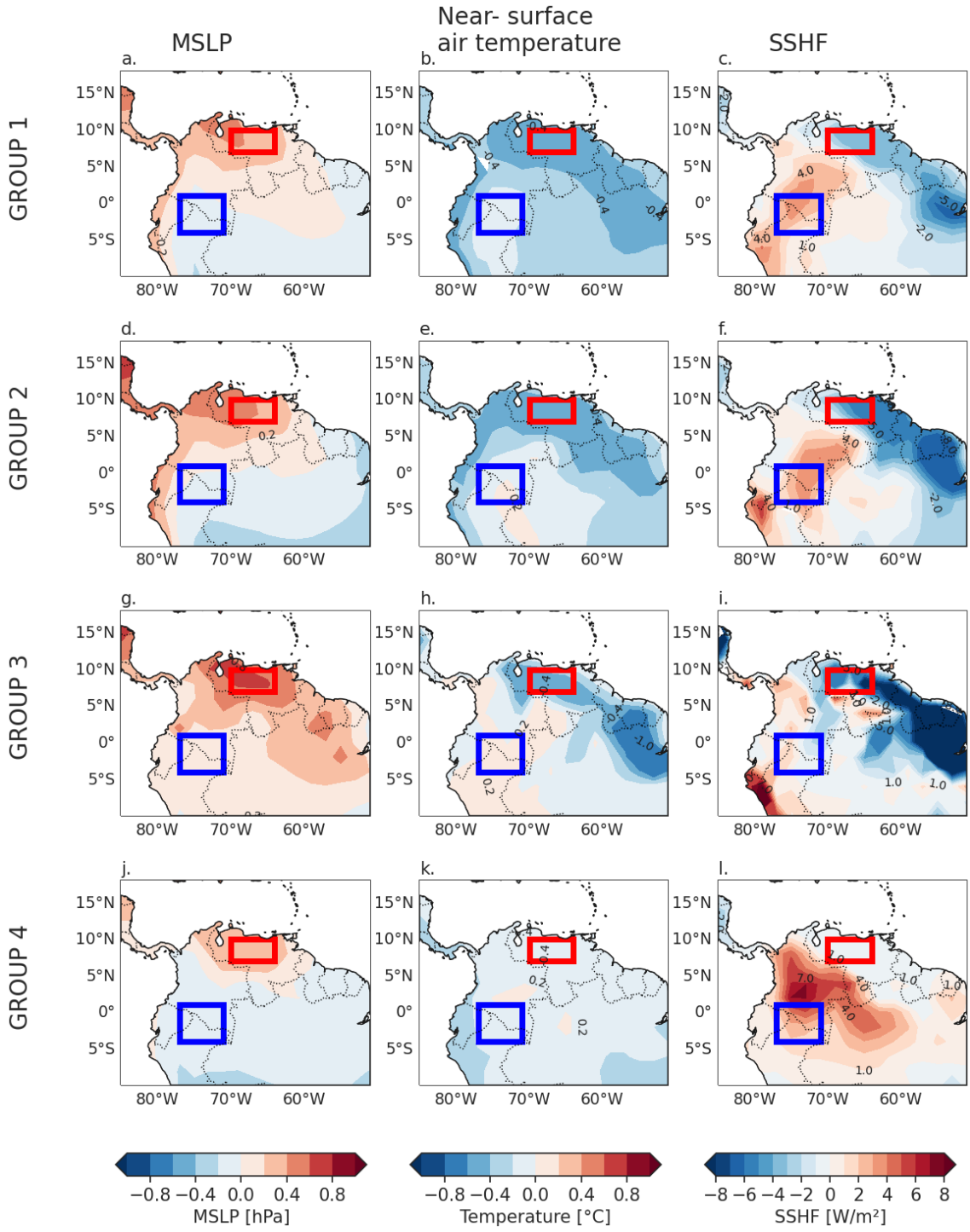

Figure 2.18: As in Figure 2.16 but for the CMIP6 clusters during strong OLLJ events.

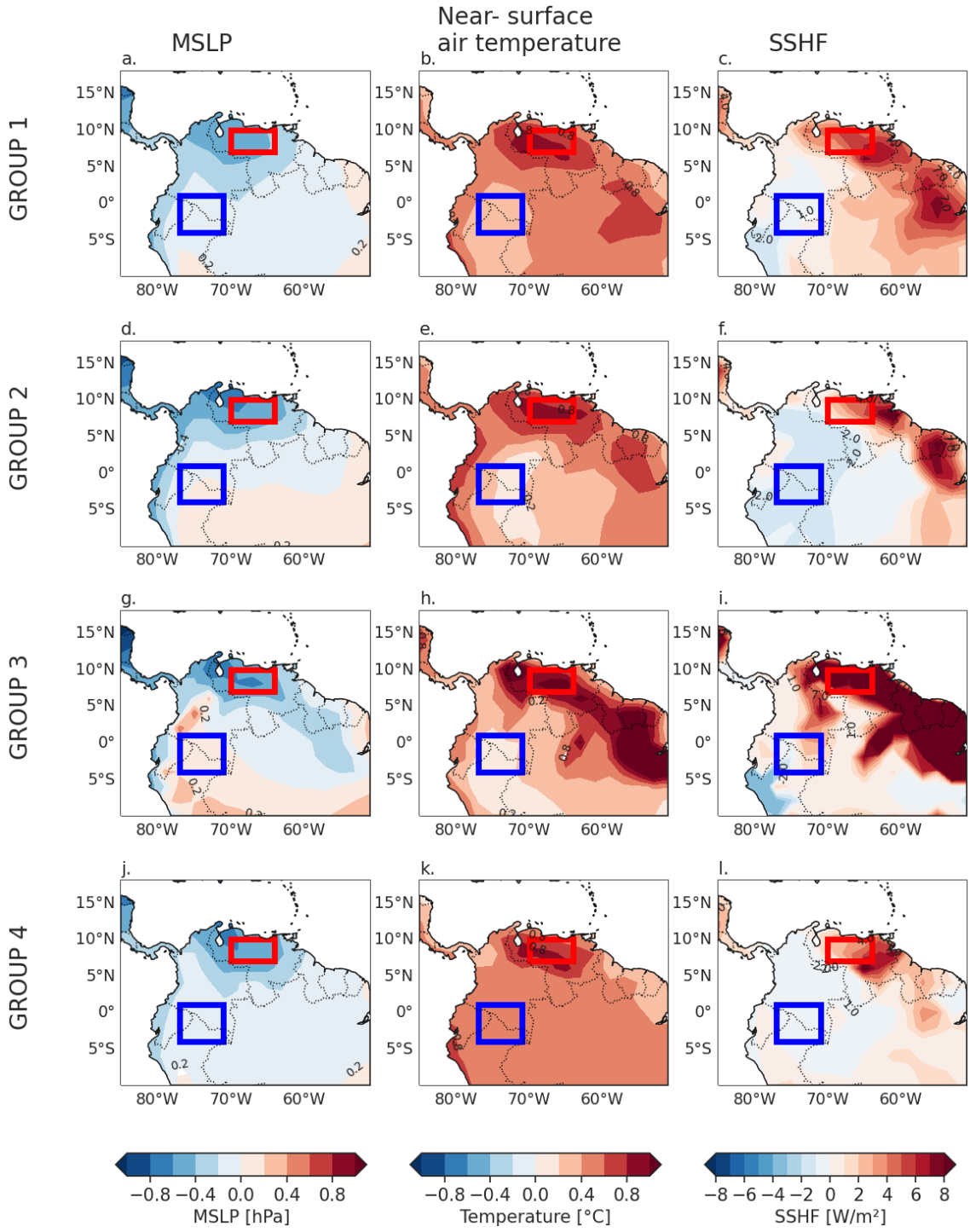

Figure 2.19: As in Figure 2.17 but for the CMIP6 clusters during weak OLLJ events.

2.3.5 Atmospheric moisture transport and mid-level circulation in northern South America simulated by the CMIP5/CMIP6 models

Section 1.3.4 assesses the link between atmospheric moisture transport in northern South America and the activity of the OLLJ. Our findings suggest that the role of the OLLJ in moisture transport in lower levels (825-950 hPa) varies depending on the location along the jet corridor. Specifically, at the exit of the jet, the OLLJ potentiates atmospheric moisture transport through the Orinoco basin and the northern Amazon (Figure 1.8). Therefore, the observed role of the OLLJ over moisture transport in northern South America implies the relevance of evaluating if the GCMs can adequately reproduce such a link in their historical simulations, and subsequently in their climate projections.

In order to assess if the atmospheric circulation at mid levels is connected to regional patterns in the surface, Figure 2.20 presents the multimodel mean of the fields of wind velocity and specific humidity at 500 hPa during DJF for the CMIP5 and CMIP6 clusters. During DJF, the wind field at 500 hPa is characterized by a strong easterly flow over northern Colombia, which corresponds to the NASH, characterized by an anticyclonic pattern over the Caribbean Sea. All CMIP5 and CMIP6 groups reproduce the anticyclone over the Caribbean Sea, however, the strengthening of the wind pattern varies from group to group. Among all groups, Groups 2 and 4 of CMIP5 simulate the highest wind velocities associated with the anticyclonic circulation, while CMIP5 Group 1 strongly overestimates the wind magnitude over Ecuador, northern Peru, southern Colombia and northern Brazil (Figure S2.4a, e, i, m).

Regarding the specific humidity at 500 hPa, models simulate higher values over the Amazon and lower values over the Tropical North Atlantic Ocean, Caribbean Sea, and northern South America. These patterns are consistent with the southward location of the ITCZ and the occurrence of the South American Monsoon System (SAMS) during DJF when the highest values of specific humidity are expected to

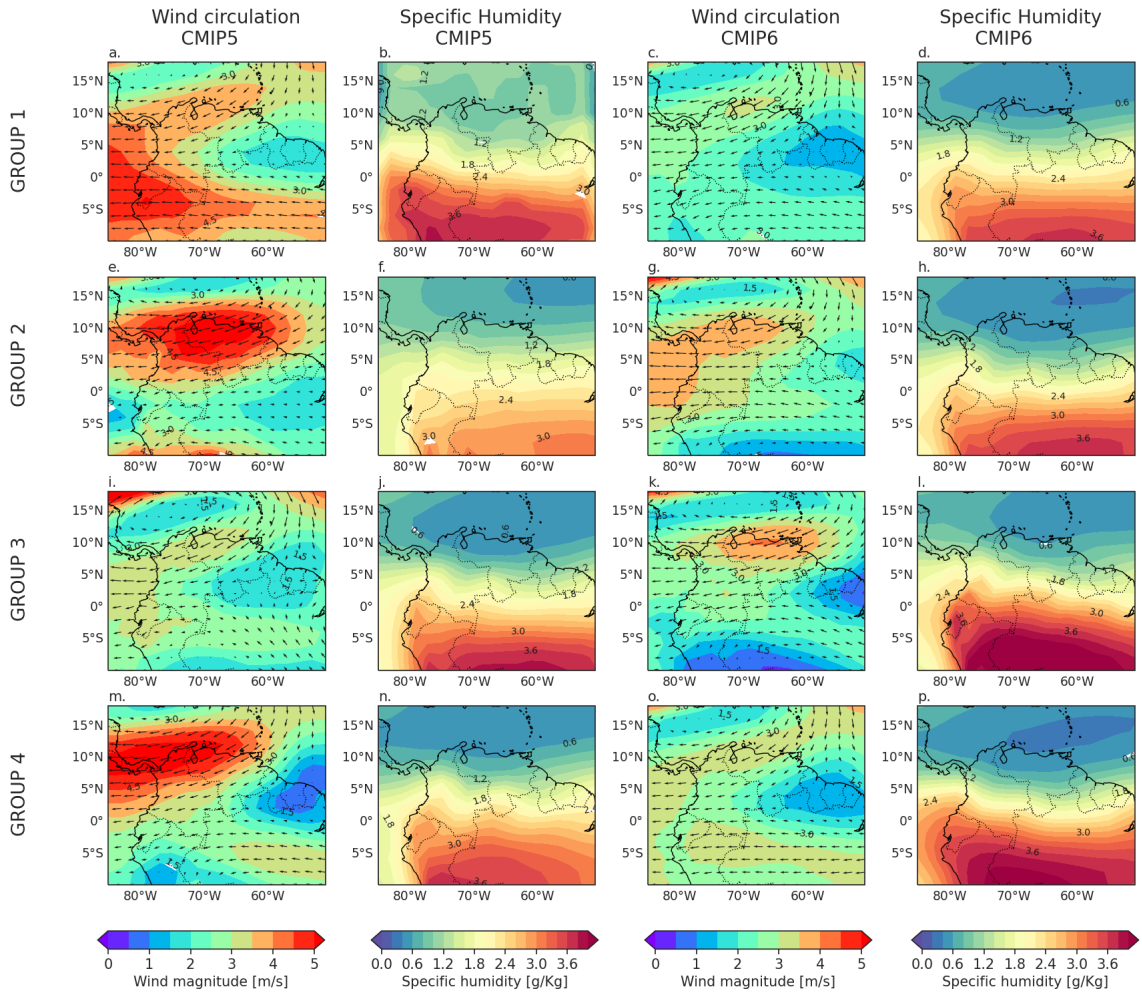

Figure 2.20: Climatology of the wind and specific humidity fields at 500 hPa during DJF from the clusters of CMIP5 (a, b, e, f, i, j, m, n) and CMIP6 (c, d, g, h, k, l, o, p) models for the historical period.

occur in the Amazon. On the other hand, models simulate drier conditions (low specific humidity) over northern South America and the tropical Atlantic, consistent with an anticyclonic circulation. Even though the CMIP5/CMIP6 models capture the spatial patterns of humidity at mid-levels of the troposphere, the average bias of each cluster shows that models tend to underestimate the humidity in the tropical North Atlantic and northern South America (Figure S2.4).

These results suggest that high SSHF and air-temperature at surface, which tend to be located over the Orinoco region (red rectangle in Figure 2.1), are accompanied by northeasterly flow and low specific humidity at mid levels, inducing drier conditions in the region. Different patterns occur over the Andes-Amazon transition region (blue rectangle in Figure 2.1), where wind circulation at 500 hPa is characterized by the convergence of northeasterly and easterly flow, while the specific humidity increases, which can be related to more humid conditions at the exit of the jet, as obtained by Segura et al. (2020) when analyzing rainfall in the Amazon. There does not seem to be a marked relationship between fluctuations in the simulation of wind circulation and specific humidity at mid levels and surface patterns, particularly of SSHF and air-temperature (Figures 2.12 and 2.13). This is based on the fact that the CMIP5 and CMIP6 clusters tend to exhibit similar biases in the simulation of these features at 500 hPa while they do not show a clear signal on the surface.

The vertically-integrated moisture flux (VIMF) between 800 and 1000 hPa simulated from the clusters of CMIP5 (Figure 2.21a, e, i, m) and CMIP6 (Figure 2.21c, g, k, o) for DJF indicates lower VIMF in western Colombia, Ecuador and Peru, while the highest values of moisture flux in the atmospheric column are located in the Caribbean Sea and northern Brazil. Some clusters properly simulate the VIMF into the Orinoco basin, with values around 120 kg/ms. However, although a better simulation of the VIMF can be related to a better simulation of the OLLJ since both focus on lower pressure levels, it is relevant to consider that some biases may be added according to the simulation of the specific humidity at lower pressure levels. The mean bias (Figure 2.21b, f, j, n for CMIP5 and Figure 2.21d, h, l, p for CMIP6) suggests that models tend to underestimate the VIMF along the OLLJ corridor,

and most of the clusters in both CMIP phases overestimate the moisture flux in the western slope of Los Andes mountain range and northern Amazon.

As an additional assessment necessary to understand how GCMs simulate the OLLJ and its links with moisture transport in northern South America, we perform a simple linear regression between the anomalies of the OLLJ index and the anomalies of the VIMF in each grid cell, similar to the analysis presented in section 1.3.4 from ERA5. For this analysis, we focus on the VIMF between 825 and 950 hPa Here, we show the regression patterns for the HadGEM2-AO model from CMIP5 and the MPI-ESM1-2-HR model from CMIP6, which tend to have a high mean PCC and a low mean RMSE in all the main features of the jet (i.e. they show a better simulation of the low-level wind circulation in northern South America), and the IPSL-CM5A-LR model from CMIP5 and the KIOST-ESM model from CMIP6, which have a low PCC and a high RMSE (i.e. they have a more biased simulation of the low-level wind circulation in northern South America). Figure 2.22 shows the simple linear regression for the CMIP5 (Figure 2.22a, c) and CMIP6 (Figure 2.22b, d) models. Colored cells indicate statistically significant relationships between the activity of the OLLJ (the OLLJ index) and the series of VIMF, with red colors indicating a positive relationship and blue colors the opposite.

The results from ERA5 (Figure 1.8d) suggest a positive relationship between the OLLJ intensity and the VIMF along the OLLJ corridor, with negative relationships in limited regions over the Andes and Brazil. This analysis indicates that a strengthening of the OLLJ is associated with high VIMF in the Orinoco basin and northern Amazon, and low VIMF in northern Brazil (the opposite when the OLLJ is weak). Models with a better performance simulating the main features of the OLLJ (Figure 2.22a, b) capture the positive relationship between the intensity of the OLLJ and the VIMF in the Orinoco basin and the northern Amazon, as observed from ERA5 (Figure 1.8d). Also, MPI-ESM1-2-HR can simulate the negative link between the OLLJ index and VIMF in northern Brazil and the Andes, as the reference database suggests (Figure 1.8d). Models with the worst representation of the low-level wind circulation in northern South America also tend to misrepresent the links between the OLLJ intensity and the atmospheric moisture flux in the region (compare Figure

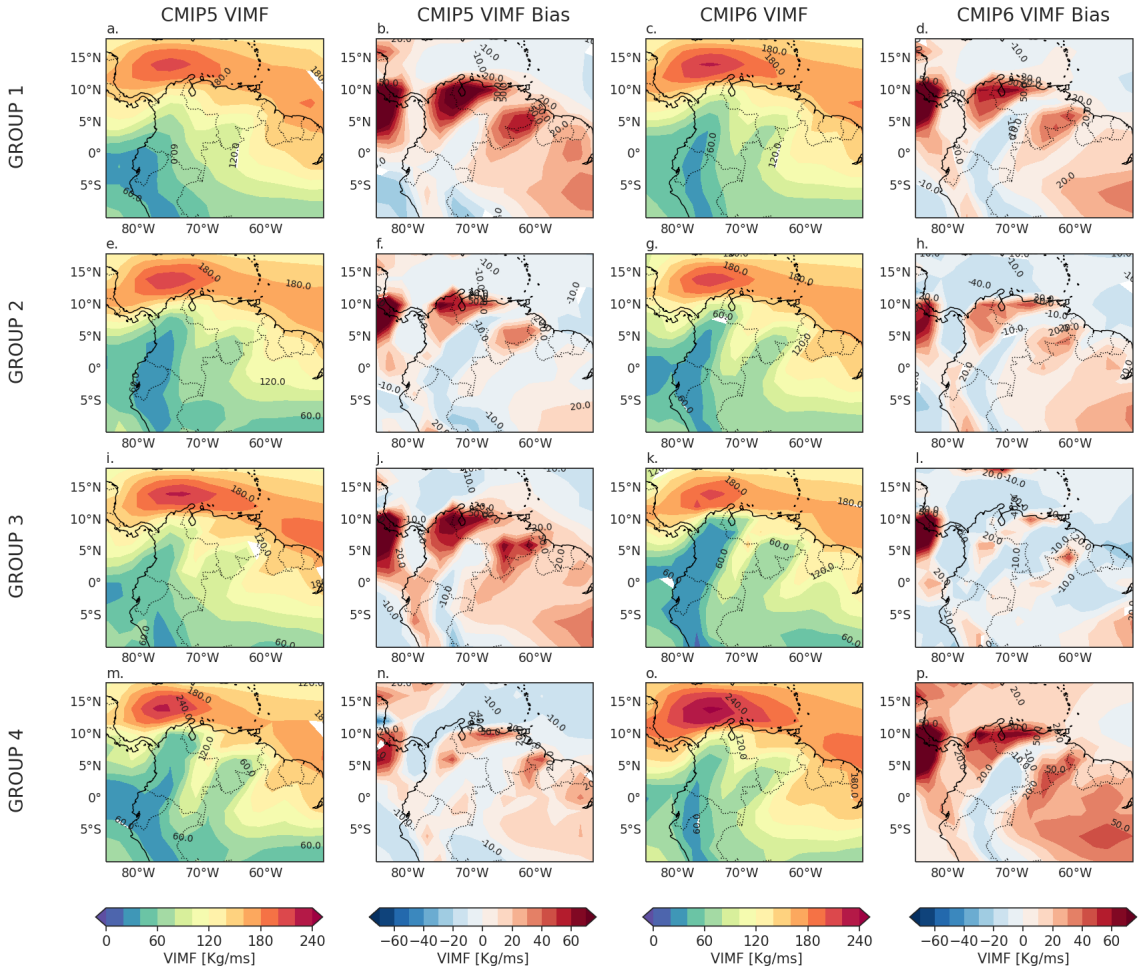

Figure 2.21: Climatology and bias of the VIMF during DJF from the clusters of the CMIP5 (a, b, e, f, I, j, m, n) and CMIP6 (c, d, g, h, k, l, o, p) models for the historical period.

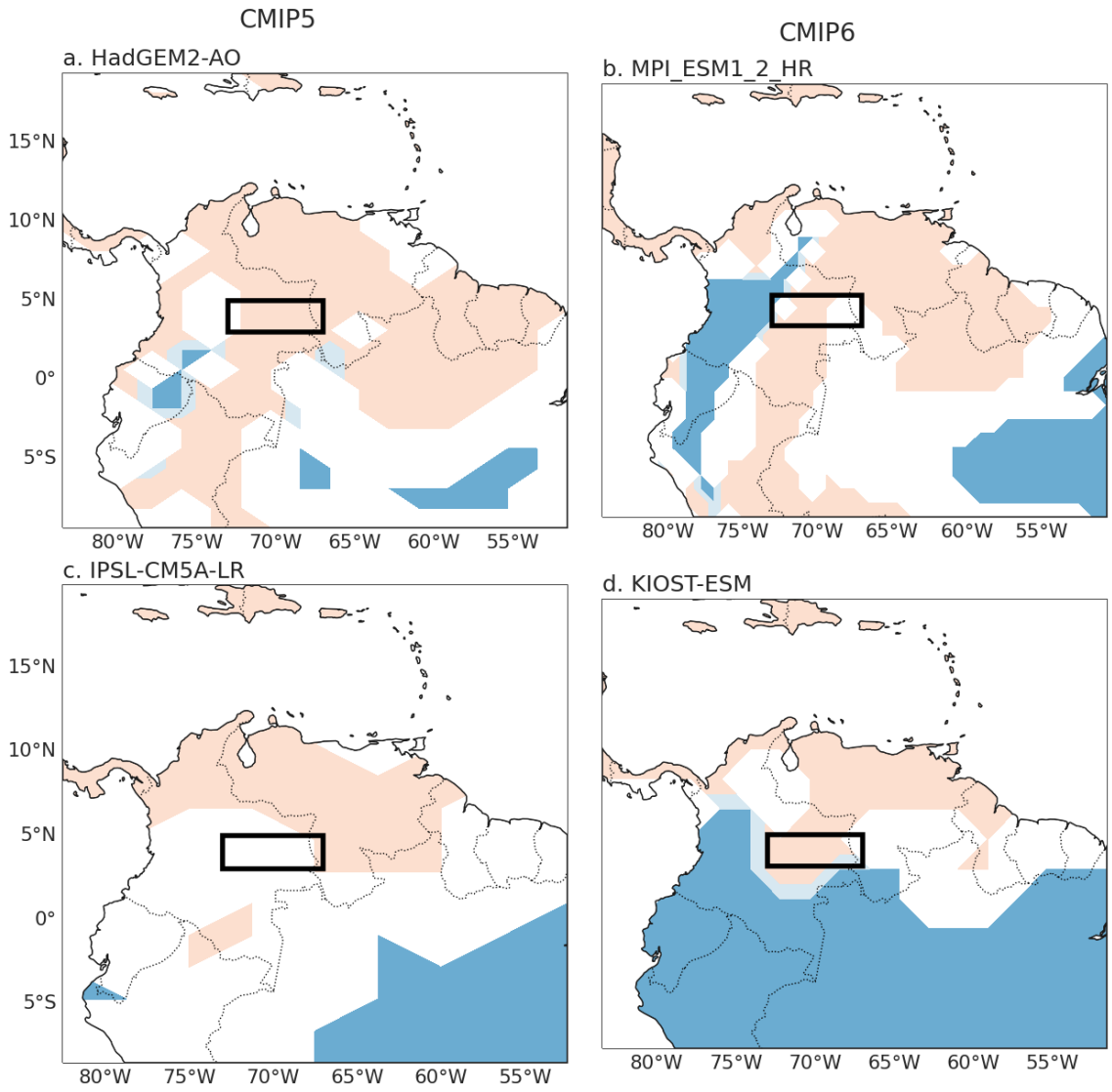

Figure 2.22: Simple linear regression between the anomalies of the OLLJ index estimated in region C3.4 (black rectangle) and the anomalies of VIMF in each cell for the historical experiment of four selected models: (a) HadGEM2-AO and (c) IPSL-CM5A-LR for CMIP5, and (b) MPI-ESM1-2-HR and (d) KIOST-ESM for CMIP6. Colored cells represent a statistically significant relationship with an alpha of 0.05. Red colors represent a positive slope and blue colors represent a negative slope.

2.22c, d with Figure 1.8d), as they do not simulate the positive link along the jet corridor either because of the lack of statistically significant relationship (no color) or because they show a negative slope (blue colors).

The above suggests that the CMIP5/CMIP6 models are able to capture the spatial linkages between the jet activity and the VIMF in northern South America; however, their performance in simulating this link seems to be strongly related to their ability to simulate the low-level wind circulation in the region.

2.4 Conclusions

This chapter analyzes the simulation of the OLLJ by a set of GCMs included in CMIP5 and CMIP6. We used PCC and RMSE as the metrics to evaluate the model performance in the simulation of the seasonal horizontal wind in northern South America, the vertical structure of this LLJ, and the OLLJ index, in comparison with the estimates from ERA5. To identify groups of models with a similar representation of these features, we applied a factor analysis and cluster analysis, showing that models from the same institute tend to group into the same cluster (Figure 2.7). This behavior is observed for both CMIP5 and CMIP6 groups, suggesting significant differences among the models of different institutes.

The results from CMIP5 models, shown in Figures 2.8 and 2.9, suggest marked differences among the GCMs, as not all clusters can represent the spatial characteristics of the OLLJ. Even though the CMIP5 groups simulate the strengthening of the wind field in northern South America during DJF, some of them are not able to differentiate the OLLJ from the surrounding wind circulation in the region. This result indicates that an accurate simulation of some regional features, such as topography, may be relevant when evaluating the OLLJ from GCM simulations. Specifically, Group 4, which contains the models from the Met Office, has the best performance among the clusters, while Group 1, which encompasses models from different institutes, exhibits the worst performance among CMIP5 models (Table 2.2). The above does not imply that all models included in Group 1 cannot capture the main characteristics of the OLLJ. However, they can fail in an accurate simulation of the seasonal

variations of the wind field in northern South America, for instance, exhibiting an overestimation of the wind magnitudes during other periods.

On the other hand, all clusters from CMIP6 models can represent the spatial patterns of the OLLJ as the four clusters considered simulate the change of direction of the surface wind field in the Orinoco basin and the formation of the jet core in its vertical structure (Figures 2.10 and 2.11). This indicates an improvement in CMIP6 models compared to CMIP5, for which the groups of models exhibit significant contrasts in their simulations. In terms of the OLLJ characteristics, our results suggest that even though CMIP6 Groups 2 and 3 perform better overall, the differences with the other clusters are not as contrasting as in CMIP5 models. It is relevant to notice that the MPI-ESM1-2-HR model displays the most prominent differences among CMIP6 since it is not grouped with other models by cluster analysis.

The simulation of MSLP and near-surface air temperature between the Tropical North Atlantic and the Andes-Amazon transition region shown in Figures 2.14 and 2.15 can influence how CMIP5 models represent the OLLJ; however, the linkage is not very clear for the CMIP6 models, which may be in part due to a more similar performance in the simulation of the OLLJ by the CMIP6 clusters. On the other hand, other factors like the topography may influence the simulation of important spatial features of the OLLJ, such as the change of direction of the surface wind along the Orinoco basin and the formation of the OLLJ vertical structure. However, an accurate representation of these gradients is not always related to a better performance of the CMIP5 and CMIP6 models in their simulation of the OLLJ.

Besides, the groups of both CMIP phases with a better and worse representation of the OLLJ can associate changes in the jet intensity with variations in the gradients of MSLP, SSHF, and near-surface air temperature between the northern and southern regions of the jet corridor (Figures 2.16, 2.17, 2.18 and 2.19). As analyzed in Chapter 1, the strengthening or weakening of the OLLJ may be influenced by these regional patterns. In particular, stronger (weaker) jet events are associated with increasing (decreasing) MSLP and decreasing (increasing) SSHF and near-surface air temperature in the Orinoco region, as also observed from ERA5 data (section 1.3.5, Figure

1.13) and Martínez et al. (2022). Thus, an accurate linkage of changes in the jet intensity with the gradients between the Orinoco and the Andes-Amazon transition region can improve the simulation of variations in the OLLJ intensity that may not be modulated by the gradients between the oceanic and the landmass regions.

Finally, regarding the moisture patterns in northern South America, CMIP5/CMIP6 models capture the increase of VIMF during DJF associated with the activation of the OLLJ (Figure 2.21). However, the accuracy of their simulation of these patterns in the Orinoco basin is linked to how GCMS represent the OLLJ; therefore, clusters with a better simulation of the OLLJ tend to have an accurate simulation of the spatial distribution of VIMF in northern South America (Figure 2.21g, m). In contrast, the opposite pattern is found in the worst groups (Figure 2.21a, o). The above is also shared when evaluating the linear regression between the OLLJ activity and VIMF in lower pressure levels from a set of specific models (Figure 2.22), where models with an accurate simulation of northern South America circulation tend to link the strengthening of the OLLJ with high VIMF in the Orinoco basin and northern Amazon, as it is obtained from ERA5.

2.5 Supplementary material

Table S2.1: Classification of the CMIP5 models after the factor analysis and the cluster analysis.

Group 1	**Group 2**	**Group 3**	**Group 4**
HadCM3	CMCC-CESM	CSIRO-Mk3-6-0	CMCC-CM
ACCESS1	CMCC-CMS	MIROC5	HadGEM2-AO
ACCESS1-3	CNRM-CM5	MRI-CGCM3	HadGEM2-CC
CanCM4	CNRM-CM5-2	MRI-ESM1	HadGEM2-ES
CanESM2	GISS-E2-H		
GFDL-CM2.1	GISS-E2-H-CC		
GFDL-CM3	GISS-E2-R		
GFDL-ESM2G	GISS-E2-R-CC		
GFDL-ESM2M	MPI-ESM-MR		
INM_CM4	MPI-ESM-P		
IPSL-CM5A-LR	MPI_ESM_LR		
IPSL-CM5A-MR			
IPSL-CM5B-LR			
MIROC-ESM			
MIROC-ESM-CHEM			
MIROC4h			
NorESM1-M			
NorESM1-ME			

Table S2.2: Classification of the CMIP6 models after the factor analysis and the cluster analysis.

Group 1	**Group 2**	**Group 3**	**Group 4**
ACCESS-ESM1-5	ACCESS-CM2	MPI_ESM1_2_HR	BCC-CSM2-MR
BCC-ESM1	GFDL-ESM4		CMCC-CM2-HR4
CAMS-CSM1-0	IITM-ESM		CMCC-CM2-SR5
CanESM5	KACE-1-0-G		CMCC-ESM2
CESM2-FV2	MRI-ESM2-0		FIO-ESM-2-0
E3SM-1-0	NorESM2-MM		KIOST-ESM
E3SM-1-1-ECA			MCM-UA-1-0
GISS-E2-1-G			NorCPM1
GISS-E2-1-H			
GISS-E2-2-H			
INM-CM5-0			
IPSL-CM5A2-INCA			
IPSL-CM6A-LR			
IPSL-CM6A-LR-INCA			
MIROC6			
MPI-ESM-1-2-HAM			
MPI-ESM1-2-LR			
NorESM2-LM			
SAM0-UNICON			

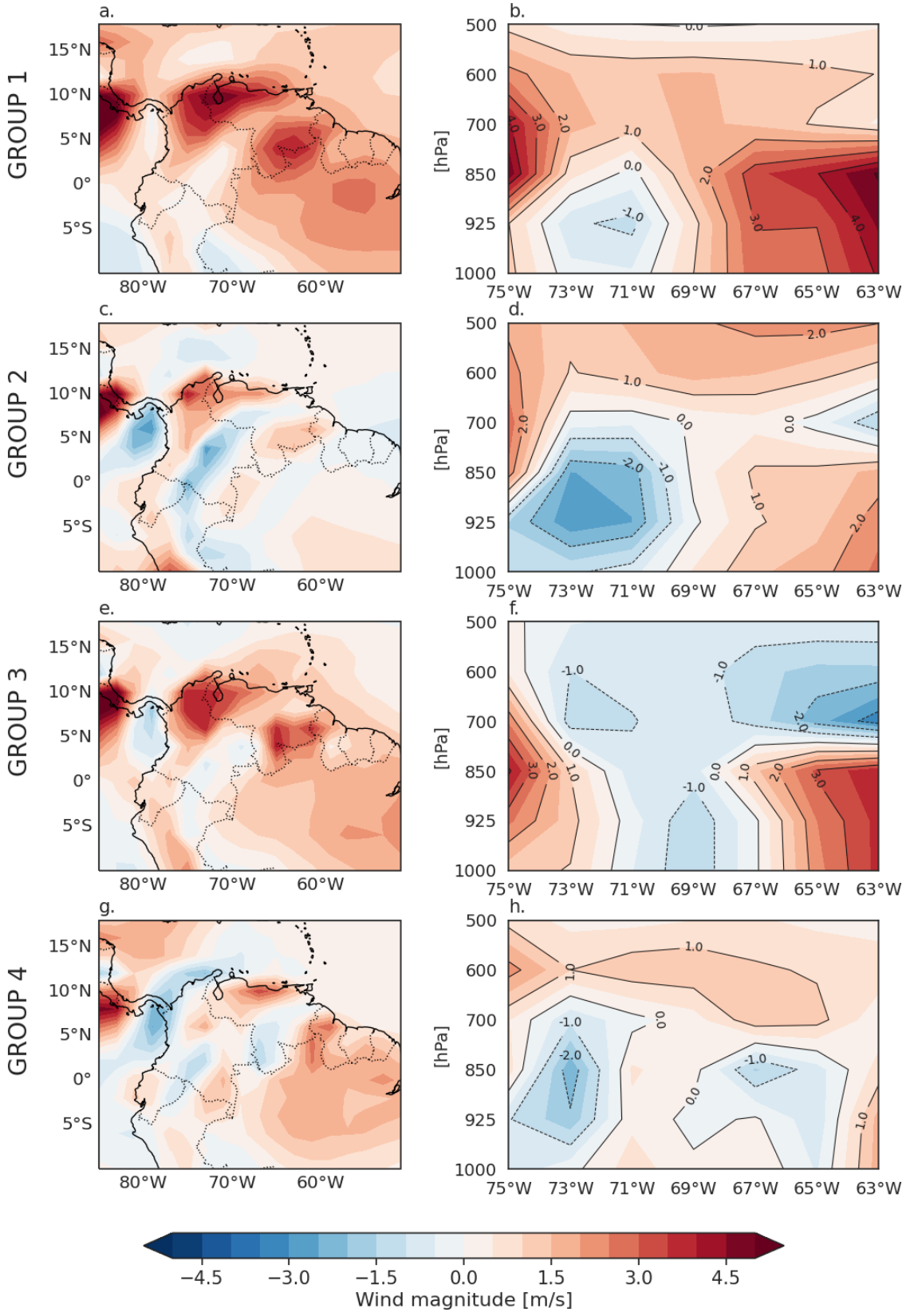

Figure S2.1: Multimodel mean bias of the horizontal winds between 825 and 950 hPa and the vertical structure of the OLLJ from the four clusters of CMIP5 models (Table S2.1) during 1979-2005. The bias is calculated as the multimodel mean of the difference between the estimates from each GCM and the estimates from ERA5 during the same period.

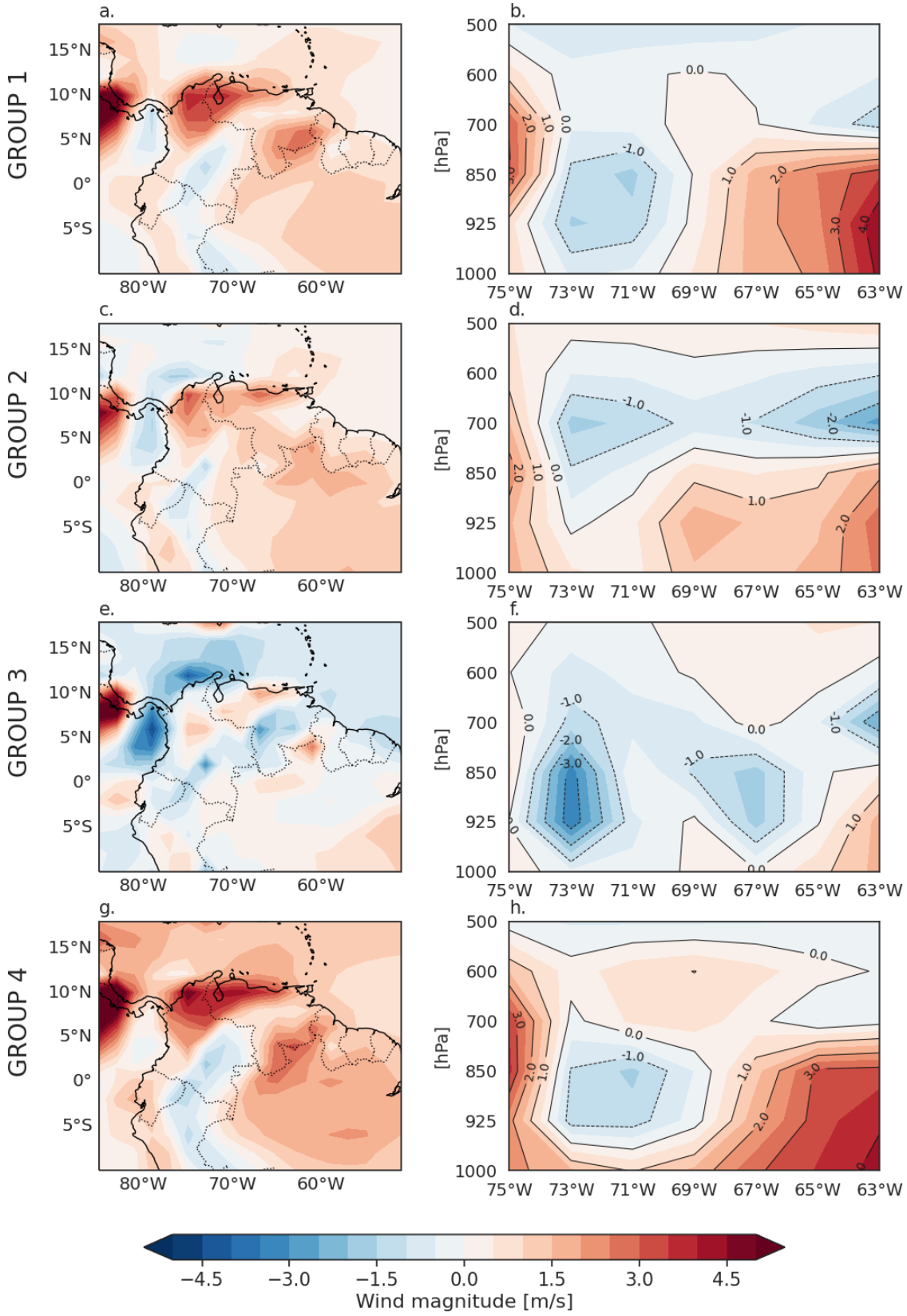

Figure S2.2: As in Figure S2.1 but for the CMIP6 clusters considered (Table S2.2) during 1979-2014.

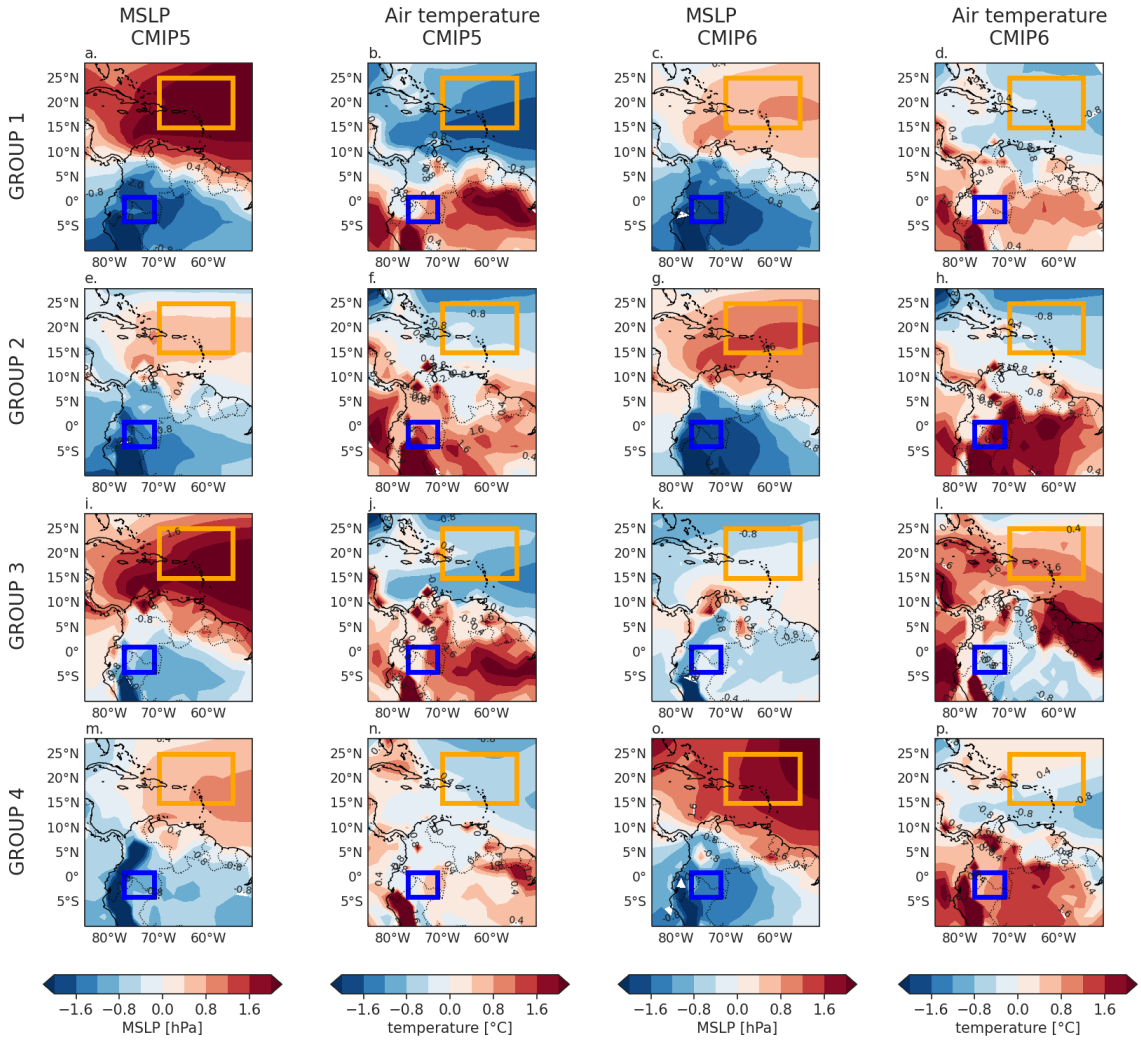

Figure S2.3: Multimodel mean bias of the MSLP and near-surface air temperature for CMIP5 (a, b, e, f, i, j, m, n) and CMIP6 (c, d, g, h, k, l, o, p) groups. The bias is calculated as a multimodel mean of the difference between the estimates from each GCM and the estimates from ERA5. Rectangles represent the regions used for the estimation of the horizontal gradients: Tropical North Atlantic (orange), and Andes-Amazon transition (blue).

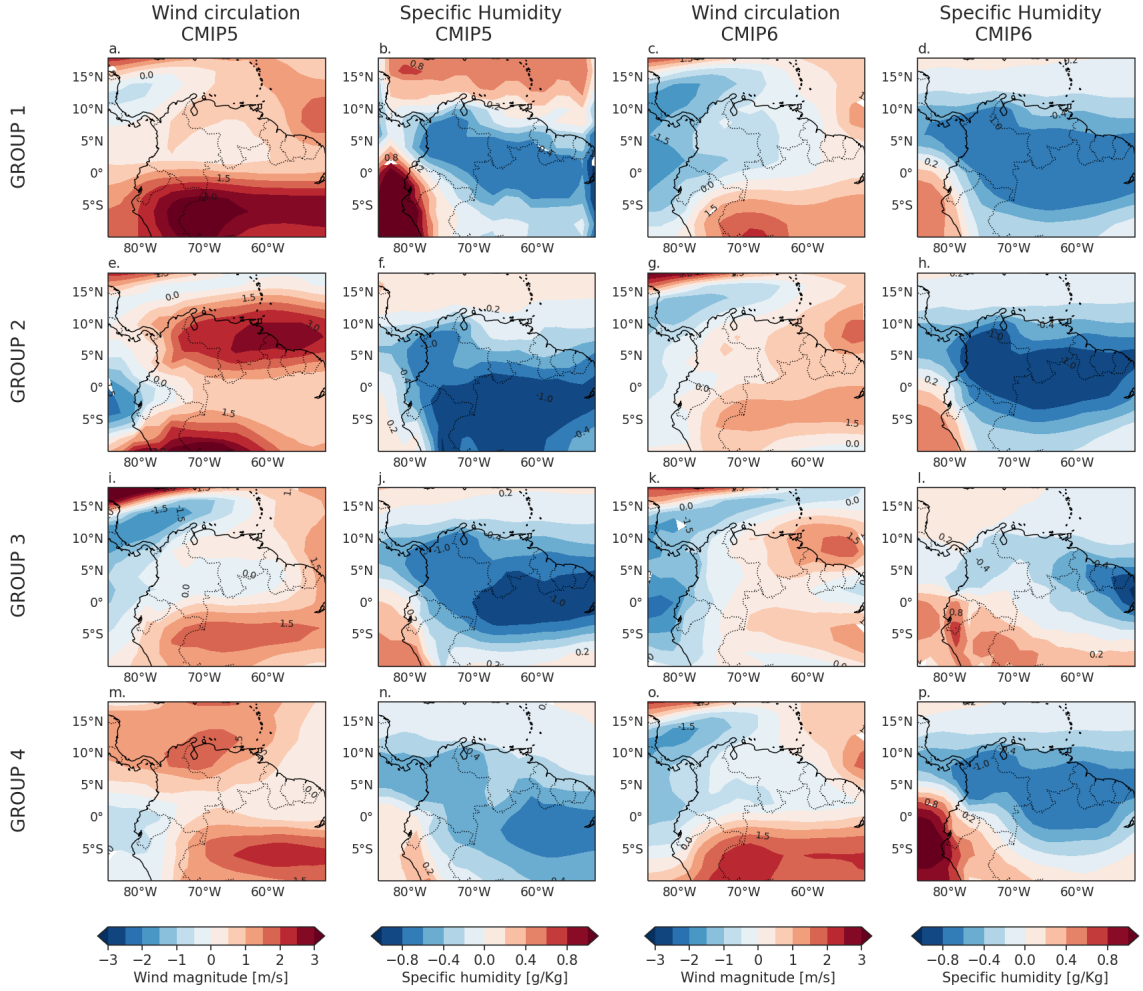

Figure S2.4: Multimodel mean bias of the wind speed and specific humidity at 500 hPa for CMIP5 (a, b, e, f, i, j, m, n) and CMIP6 (c, d, g, h, k, l, o, p) groups. The bias is calculated as a multimodel mean of the difference between the estimates from each GCM and the estimates from ERA5.

Chapter 3

Assessment of the possible future changes of the Orinoco low-level jet under different climate change scenarios

3.1 Introduction

Like other regions worldwide, South America, specifically northern South America, has experienced relevant changes in its climatological characteristics that lead to variations in the structure of regional ecosystems and human systems over the region (Castellanos et al., 2022). Some climatological shifts, such as increasing temperatures in the Andes mountain range or decreasing precipitation in the Amazon, have led to relevant variations like reductions of the Paramos area or the intensification of the aridity through the continent, among other impacts (Beck et al., 2018; Pabón-Caicedo et al., 2020; Correa et al., 2020; Castellanos et al., 2022). In addition, observed human-induced changes in land cover, like deforestation, exert additional variations in the regional climate, resulting in marked changes in the hydrological cycle and the ecosystem dynamics of northern South America and other key regions over the continent (e.g., Bovolo et al., 2018; Ruiz-Vásquez et al., 2020; Zeng et al, 2021; Sierra et al., 2022).

The atmospheric dynamics in the region, alongside interaction processes of the atmo-

sphere with land and ocean, encompasses multiple phenomena with diverse temporal and spatial scales, which have experienced and are expected to suffer variations due to climate change and other anthropic influences. This in turn modulates the observed and projected variations of meteorological events and climatological processes over the region. For instance, Chai et al. (2021) identify drier conditions in central South America after analyzing aridity trends during 1965-2014. Mesa et al. (2021) show an intensification of the hydrological cycle in Colombia. The most recent assessment report of the Intergovernmental Panel on Climate Change (IPCC) shows that heavy precipitation events have increased in frequency and intensity over southeastern South America while agricultural and ecological droughts have become more frequent in northeastern South America (Arias et al., 2021a; IPCC, 2021; Seneviratne et al., 2021). These conditions may become more severe under future climate change induced by increasing greenhouse gas (GHG) concentrations (IPCC, 2021). In particular, the changes in atmospheric moisture transport toward and within the region are particularly relevant to understand the projected changes in the hydrological cycle. Other kinds of drivers, such as variations in vegetation cover, influence the atmospheric moisture recycling in the region, therefore, inducing changes in precipitation and moisture regimes (e.g., Ruiz-Vásquez et al., 2020; O'Connor et al., 2021; Wierik et al., 2021; Sierra et al., 2022).

Low and mid-level atmospheric circulation is essential to understand the mechanisms of atmospheric moisture transport. Particularly, low-level jets (LLJ) are relevant mechanisms for moisture advection toward continental regions (Gimeno et al., 2016). Wind circulation in South America and its related atmospheric moisture transport has experienced changes during the recent decades. For instance, fluctuations in the intensity of the South American low-level jet (SALLJ) in key regions along its spatial extent (Jones, 2019) or the increase in northwesterly moisture flux to southern Brazil linked to the SALLJ activity (Montini et al., 2019) are some of the regional low-level circulation changes in South America observed during the recent decades.

General Circulation Models (GCM) are a useful tool to evaluate possible future changes in global but also regional climate. In particular, they have been used to understand possible changes in low-level circulations over South America through-

out the 21st century. Specifically, the analysis of climate projections from GCMs for South America suggests shifts in the location and strengthening of the Choco LLJ during September-October-November, as a result of changes in the temperature and pressure gradients between the eastern tropical Pacific Ocean and the Colombian landmass (Sierra et al., 2021), which can also influence regional precipitation (Valencia and Mejía, 2022). Other projections include increases in the moisture flux due to the influence of the SALLJ and the northeasterly trade winds (Thaler et al., 2021), and the westward expansion of the SALLJ and the Caribbean LLJ, partially explained by the dynamics of the subtropical anticyclones (Torres-Alavez et al., 2021).

These projected changes can differ among studies because they are strongly attached to a specific climate scenario. For instance, the GCMs included in the fifth and sixth phases of the Coupled Model Intercomparison Project (CMIP5 and CMIP6, respectively) provide projections of the evolution of the climate system throughout the 21st century considering different sets of forcings in terms of future GHG and aerosol emissions, land use change, or policies and development patterns of the societies (Collins et al., 2013; Lee et al., 2021). For climate projections, CMIP5 uses the Representative Concentration Pathways (RCPs) focused on the amount of GHG emissions and their concentrations in the atmosphere (Meinshausen et al., 2011), while CMIP6 uses the Shared Socio-Economic Pathways (SSPs) that are defined from the initiatives in the adaptation and mitigation of climate change (O'Neill et al., 2016). Both types of pathways encompass different levels of radiative forcing and raise in the global temperature, that is, scenarios with different levels of adversity. The projections under different RCPs and SSPs are usually considered when assessing possible future changes in specific aspects of the climate system.

As stated in Chapters 1 and 2, the Orinoco LLJ (OLLJ) plays an important role in the atmospheric moisture transport along the Orinoco basin to the northern Amazon (section 1.3.4) and its seasonal activation and intensity depend on synoptic and regional patterns that modulate its spatial and temporal features (sections 1.3.5 and 2.3.4). This suggests that variations in these patterns can lead to changes in the OLLJ during the 21st century, which acquires relevance given the role of this LLJ

in the seasonal moisture transport through the Orinoco basin, affecting a set of processes connected to this humidity flux induced by the jet.

Recognizing the relevance of this LLJ in the climate and water exchanges in northern South America, this chapter focuses on the projected changes of the OLLJ during its activation period (December-January-February, DJF) using the projections under different RCPs and SSPs according to CMIP5 and CMIP6 models, respectively, considering the analysis discussed in Chapter 2. The above helps to evaluate the response of the OLLJ to climate change, and even though it is not part of the scope of this study, it can suggest the kind of impacts that could be expected in the region due to changes in this LLJ.

3.2 Data and methodology

This chapter uses a set of the CMIP5 and CMIP6 models considered in Chapter 2, as listed in Table 3.1. We apply the same model classification from cluster analysis discussed in Chapter 2 (Tables S2.1 and S2.2). The set of variables used in this chapter are zonal and meridional wind components, specific humidity, sea-level pressure, near-surface air temperature, and surface sensible heat flux (SSHF) . The models used in this chapter are also defined by the availability of these variables for the different RCPs and SSPs considered. To assess the projected changes of the OLLJ, we focus on the main features previously discussed in Chapters 1 and 2: horizontal wind, vertical structure, and the OLLJ index (section 1.2). The horizontal patterns of the jet and the OLLJ index use zonal and meridional wind between 825 and 950 hPa, while the vertical structure of the jet encompasses the atmospheric column from 1000 to 500 hPa in order to identify the core of the jet from the regional wind field. As in Chapter 2, the OLLJ index is defined as the spatial average of the meridional wind between 825 and 950 hPa in region C3.4 (3°N-5°N - 73°W-67°W: Figure 2.1) while the cross section to assess the vertical structure of the jet is centered at 3°N-5°N and 75°W-61°W, and is calculated from the average of the latitudes between 3°N and 5°N.

To assess the projected changes of the OLLJ, this study uses the RCP4.5 (Thomson

Table 3.1: Projections from CMIP5 and CMIP6 models used in this study under different GHG scenarios. RCP: Representative Concentration Pathway, CMIP5. SSP: Shared Socioeconomic Pathway, CMIP6.

Model	**CMIP phase**	**Experiment**
ACCESS1-0	CMIP5	RCP 4.5, RCP 8.5
ACCESS1-0	CMIP5	RCP 4.5, RCP 8.5
CanESM2	CMIP5	RCP 4.5, RCP 8.5
CMCC-CM	CMIP5	RCP 4.5, RCP 8.5
CMCC-CMS	CMIP5	RCP 4.5, RCP 8.5
CNRM-CM5	CMIP5	RCP 4.5, RCP 8.5
CSIRO-Mk3-6-0	CMIP5	RCP 4.5, RCP 8.5
GFDL-CM3	CMIP5	RCP 4.5, RCP 8.5
GFDL-ESM2G	CMIP5	RCP 4.5, RCP 8.5
GFDL-ESM2M	CMIP5	RCP 4.5, RCP 8.5
GISS-E2-H	CMIP5	RCP 4.5, RCP 8.5
GISS-E2-H-CC	CMIP5	RCP 4.5, RCP 8.5
GISS-E2-R	CMIP5	RCP 4.5, RCP 8.5
GISS-E2-R-C	CMIP5	RCP 4.5, RCP 8.5
HadGEM2-AO	CMIP5	RCP 4.5, RCP 8.5
HadGEM2-CC	CMIP5	RCP 4.5, RCP 8.5
HadGEM2-ES	CMIP5	RCP 4.5, RCP 8.5
INM_CM4	CMIP5	RCP 4.5, RCP 8.5
IPSL-CM5A-LR	CMIP5	RCP 4.5, RCP 8.5
IPSL-CM5A-MR	CMIP5	RCP 4.5, RCP 8.5
IPSL-CM5B-LR	CMIP5	RCP 4.5, RCP 8.5
MIROC5	CMIP5	RCP 4.5, RCP 8.5
MIROC-ESM	CMIP5	RCP 4.5, RCP 8.5
MIROC-ESM-CHEM	CMIP5	RCP 4.5, RCP 8.5
MPI_ESM_LR	CMIP5	RCP 4.5, RCP 8.5
MPI-ESM-MR	CMIP5	RCP 4.5, RCP 8.5
MRI-CGCM3	CMIP5	RCP 4.5, RCP 8.5
MRI-ESM1	CMIP5	RCP 4.5, RCP 8.5
NorESM1-M	CMIP5	RCP 8.5
NorESM1-ME	CMIP5	RCP 4.5, RCP 8.5
ACCESS-CM2	CMIP6	SSP2-4.5, SSP3-7.0, SSP5-8.5
ACCESS-ESM1-5	CMIP6	SSP2-4.5, SSP3-7.0, SSP5-8.5
BCC-CSM2-MR	CMIP6	SSP2-4.5, SSP3-7.0, SSP5-8.5
CAMS-CSM1-0	CMIP6	SSP2-4.5, SSP3-7.0, SSP5-8.5
CanESM5	CMIP6	SSP2-4.5, SSP3-7.0, SSP5-8.5
CMCC-CM2-SR5	CMIP6	SSP2-4.5, SSP3-7.0, SSP5-8.5
CMCC-ESM2	CMIP6	SSP2-4.5, SSP3-7.0, SSP5-8.5
FIO-ESM-2-0	CMIP6	SSP2-4.5, SSP5-8.5

Table 3.1: Continuation

Model	CMIP phase	Experiment
GFDL-ESM4	CMIP6	SSP2-4.5, SSP3-7.0, SSP5-8.5
IITM-ESM	CMIP6	SSP2-4.5, SSP3-7.0, SSP5-8.5
INM-CM5-0	CMIP6	SSP2-4.5, SSP3-7.0, SSP5-8.5
IPSL-CM6A-LR	CMIP6	SSP2-4.5, SSP3-7.0, SSP5-8.5
KACE-1-0-G	CMIP6	SSP2-4.5, SSP3-7.0, SSP5-8.5
KIOST-ESM	CMIP6	SSP2-4.5, SSP3-7.0, SSP5-8.5
MIROC6	CMIP6	SSP2-4.5, SSP3-7.0, SSP5-8.5
MPI-ESM1-2-LR	CMIP6	SSP2-4.5, SSP3-7.0, SSP5-8.5
MPI_ESM1_2_HR	CMIP6	SSP2-4.5, SSP3-7.0, SSP5-8.5
MRI-ESM2-0	CMIP6	SSP2-4.5, SSP3-7.0, SSP5-8.5
NorESM2-LM	CMIP6	SSP2-4.5, SSP3-7.0, SSP5-8.5
NorESM2-MM	CMIP6	SSP2-4.5, SSP3-7.0, SSP5-8.5

et al., 2011) and RCP8.5 (Riahi et al., 2011) scenarios for CMIP5 models, and the SSP2-4.5, SSP3-7.0 and SSP5-8.5 scenarios for CMIP6 models (Meinshausen et al., 2020). The projected changes of the horizontal wind and the vertical structure of the jet are evaluated using the differences between the multimodel mean for the future projections and the historical simulation during 1979-2005 for CMIP5 models and 1979-2014 for CMIP6 models. The future projections considered here focus on the long-term period that encompasses from 2081 to 2100, i.e. the end of the 21st century. On the other hand, the analysis of the projected changes in the OLLJ intensity using the OLLJ index aims to identify possible changes in the jet strength during its activation period (DJF) throughout the 21st century. The projected changes of this index are calculated from the historical climatology of the DJF index and trend analysis in the long-term series using the Mann-Kendall test (Mann, 1945; Kendall, 1948), which is a non-parametric test widely used in the detection of trends of meteorological variables.

On the other hand, as discussed in Chapter 2, GCMs within CMIP5 and CMIP6 can simulate the coupling between the activation of the OLLJ and the contrast of mean sea level pressure (MSLP) and near-surface air temperature between the Tropical North Atlantic and the Andes-Amazon transition region (orange and blue rectangles in Figure 2.1, respectively). Thus to explain possible changes in the OLLJ by the end of the 21st century, we evaluate the projected changes of the horizontal gradients

of MSLP and temperature between these regions during 2081-2100. On the other hand, as the strength of the OLLJ is also related to regional gradients of MSLP, SSHF, and near-surface air temperature between the northern and southern parts of the jet corridor (see Chapters 1 and 2), we evaluate the patterns of these gradients by the end of the century and how they are linked to changes in the intensity of the OLLJ. Here, the OLLJ intensity is defined as variations in the wind magnitude associated with the jet during DJF, and the regional gradients are calculated as the projected long-term changes of MSLP, air temperature, and SSHF gradients between the Orinoco and Andes-Amazon transition regions.

Finally, the mid-level circulation plays a relevant role in atmospheric moisture advection into northern South America, therefore this chapter also evaluates the projected changes of wind circulation and specific humidity at 500 hPa, which can link the changes in the regional patterns at the surface to changes in moisture in the atmospheric column. The projected changes for the mid-level circulation are obtained as the difference between the future projections for the long term and the historical simulation of each model. Thus, following the main findings of Chapters 1 and 2, we analyze the projected changes of the vertically-integrated moisture flux (VIMF) in the atmospheric column (1000 to 100 hPa) for the long term to assess variations in moisture flux in northern South America.

3.3 Results

3.3.1 Projected changes of the main features of the Orinoco low-level jet

Figure 3.1 presents the projected changes of the wind field between 825 and 950 hPa during DJF from the groups of CMIP5 and CMIP6 models for the long term (2081-2100) in different climate change (RCPs and SSPs) scenarios. Most of the groups in both CMIP5 and CMIP6 suggest negative projected changes, suggesting the weakening of the wind magnitude by the end of the century. The dots in Figure 3.1 represent grid cells where at least 80 percent of the models in the group agree in

the sign of the projected change, except for Group 3 in CMIP6 (Figure 3.1 k, o, s) that is composed by one single model. In all the groups, there is agreement by most of the models in the projected weakening of the wind magnitude during DJF by the end of the 21st century, particularly at the exit of the OLLJ.

Even though some groups in CMIP5 and CMIP6 project increases of wind magnitude at the entrance of the OLLJ located in the Venezuelan Llanos, the regions with greater agreement among models of the same group are located at the exit of the jet, where the future projections indicate a weakening of the circulation. These results are complemented in Figure 3.2 that shows the projected changes for the long-term of the vertical structure of the OLLJ at its exit region (dashed rectangle in Figure 2.1). Similarly, clusters in different scenarios suggest negative projected changes in lower pressure levels, which means a decrease in the wind magnitude at the exit of the jet, therefore a projected weakening of the OLLJ by the end of the century.

The projections suggest large changes in the OLLJ in its exit region, located over the Andes-Amazon transition region, thus the decreasing in wind magnitude of the OLLJ in this region suggests the shrinking of the LLJ along the Orinoco basin.

On the other hand, the projected changes of the OLLJ index during the 21st century shown in Figure 3.3 for the DJF season, that corresponds to the activation period of the OLLJ, indicate marked decreasing trends under all the scenarios and among most of the groups in CMIP5 (Figure 3.3a, b) and CMIP6 (Figure 3.3c, d, e). Asterisks in Figure 3.3 indicate statistically significant trends according to the non-parametric Mann-Kendall test with a significance level of 0.05. Our results suggest agreement among the clusters regarding the decrease of the OLLJ index intensity, pointing to a weakening of this LLJ. This pattern is observed for all the scenarios, indicating the robustness of the projections with respect to the main characteristics of the OLLJ under different possible emission trajectories. However, although most of the clusters in CMIP5/CMIP6 project the weakening of the OLLJ with a statistically significant trend, the range of wind speed variation throughout the 21st century presents values that oscillate by 0.05 m/s per decade, as shown in Table S3.1.

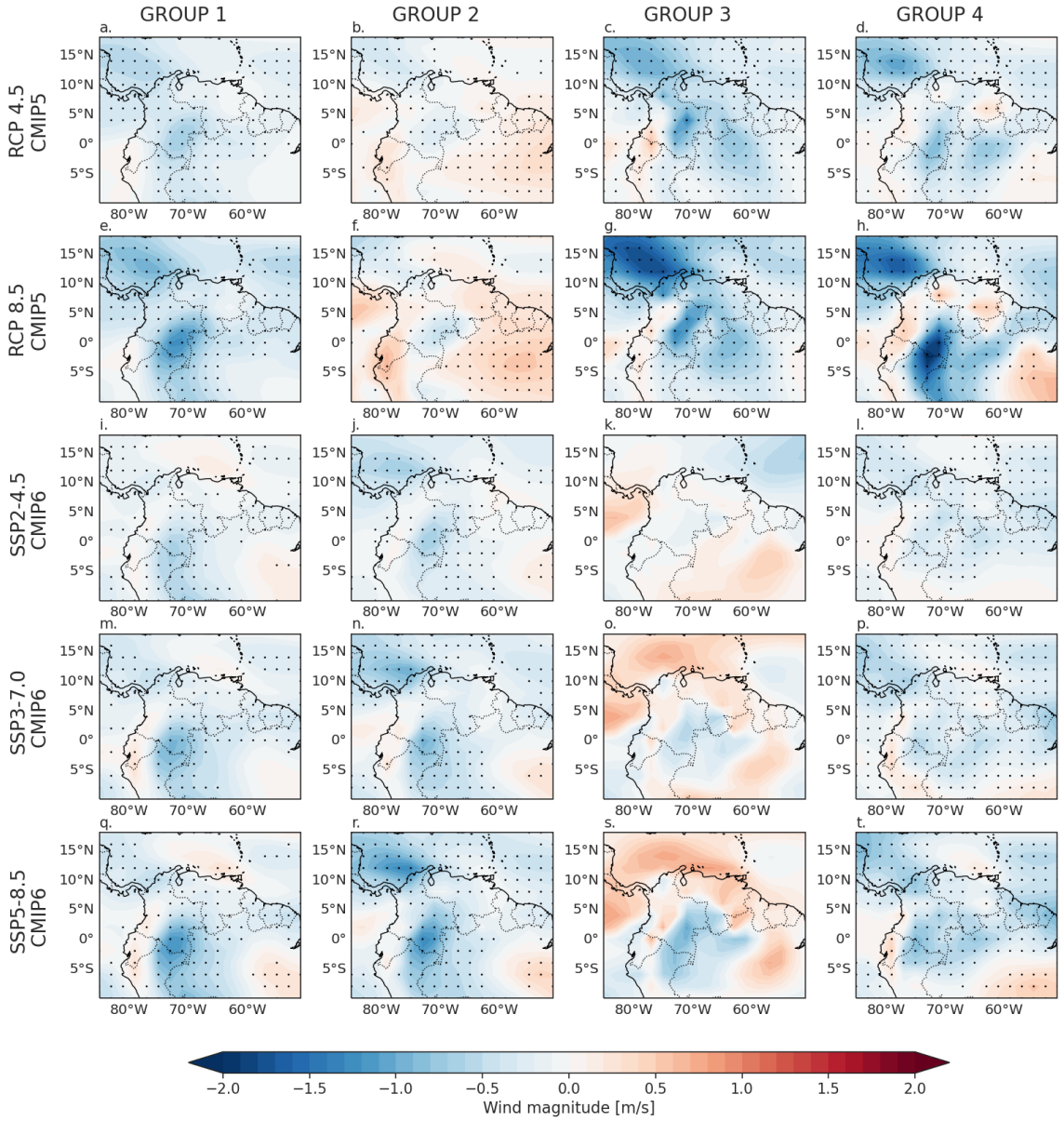

Figure 3.1: Projected changes of the DJF wind field between 825 and 950 hPa for the clusters from CMIP5 and CMIP6 models under different scenarios (RCPs for CMIP5 and SSPs for CMIP6) for the long-term (2081-2100). Dots represent the grid cells with agreement in the sign of change by at least 80% of the models within each cluster.

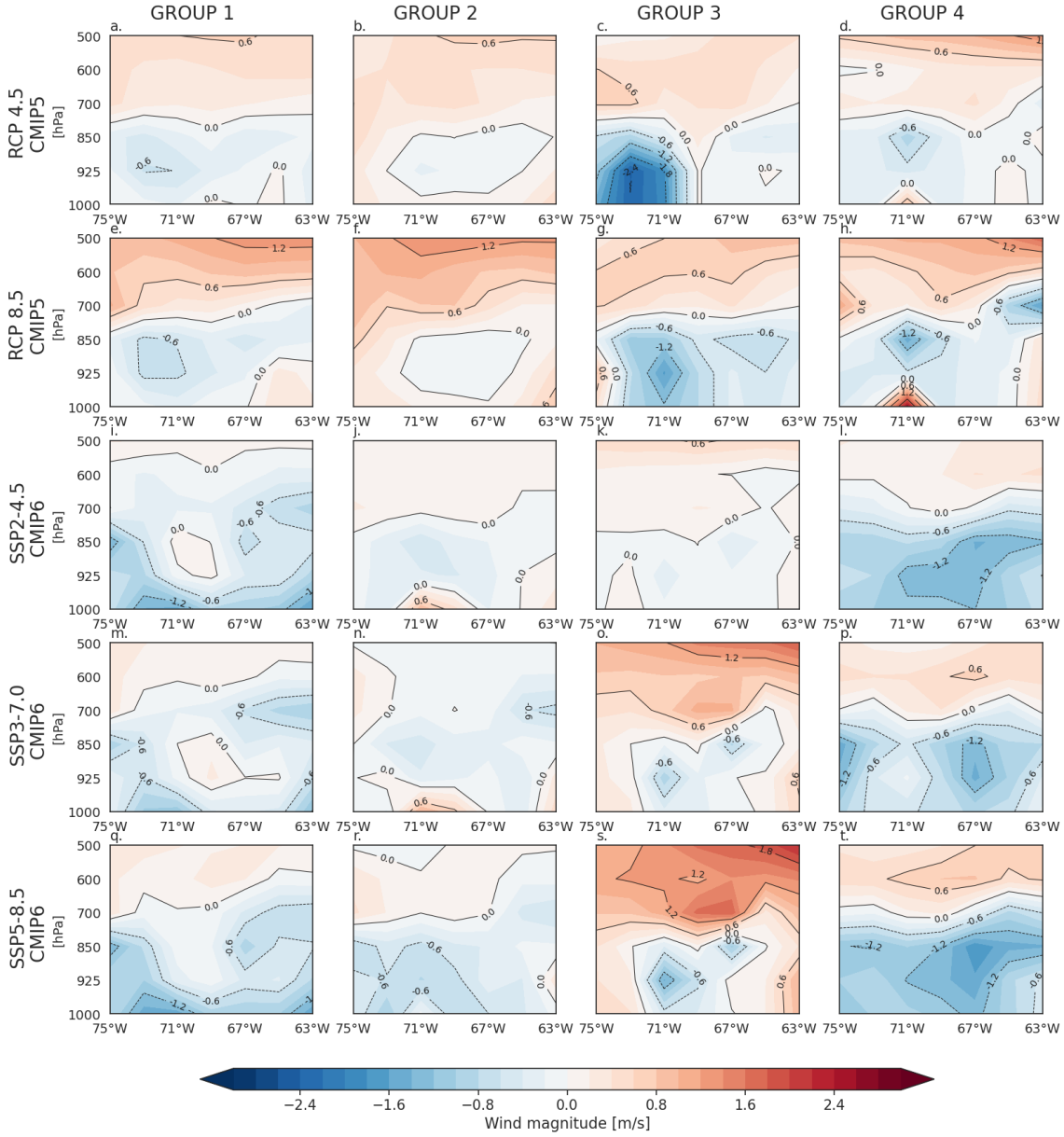

Figure 3.2: Projected changes of the DJF vertical structure of the OLLJ in the cross-section between 3°N-5°N and 75°W-61°W for the long-term (2081-2100) for the clusters from CMIP5 and CMIP6 models under different scenarios (RCPs for CMIP5 and SSPs for CMIP6).

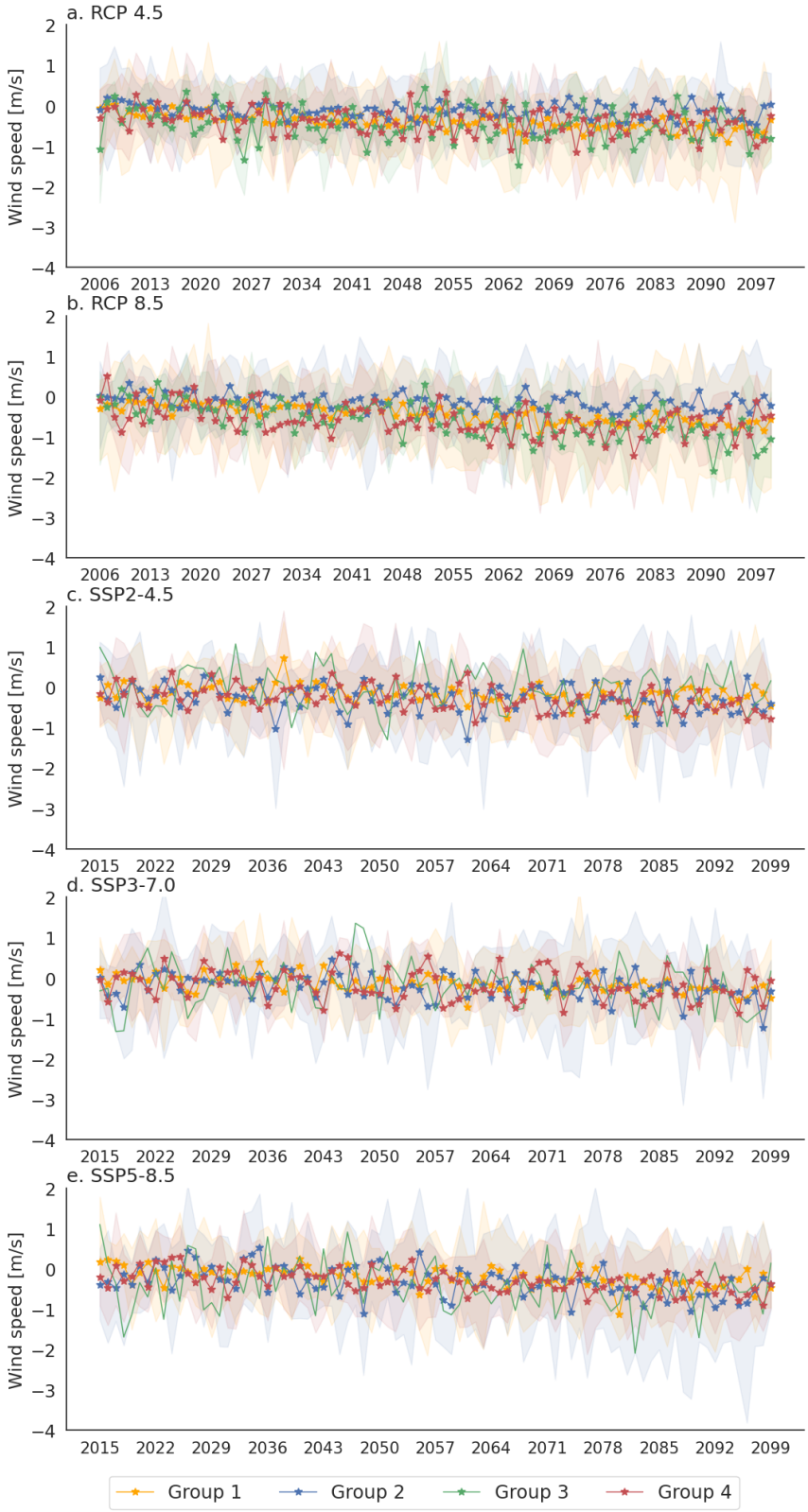

Figure 3.3: Long-term series of the changes of the OLLJ index for the DJF season for the clusters of CMIP5 and CMIP6 models under different scenarios: (a) RCP4.5, (b) RCP8.5, (c) SSP2-4.5, (d) SSP3-7.0, and (e) SSP5-8.5. The changes are estimated considering the historical simulation as the baseline (1979-2005 for CMIP5 and 1979-2014 for CMIP5). Asterisks indicate statistically significant trends according to the Mann-Kendall test.

3.3.2 Regional projected changes and their links to the projected changes of the main Orinoco low-level jet features

Possible future changes in the OLLJ features are assessed through this chapter, however, it is relevant to link those changes to variations in the regional circulation patterns that may influence the main features of the jet. Following this, Figure 3.4 shows the annual cycle of the gradients of MSLP and near-surface air temperature between the Tropical North Atlantic and the Andes-Amazon transition region. Dashed lines represent the historical simulations of the gradients, and solid lines represent the annual cycle for the long term (2081-2100) under different scenarios.

The results suggest that there are not marked projected changes in the gradients of MSLP in both CMIP5 and CMIP6 during DJF (Figure 3.4a, c, e, g, i). Besides, there is no agreement among clusters, independently of the scenario considered, in terms of variations of the gradients of MSLP between the ocean and the landmass, as some clusters project lower gradients of MSLP by the end of the century while others indicate the opposite pattern. However, when considering the gradients of near-surface air temperature (Figure 3.4b, d, f, h, j), the projected changes appear to be stronger than those of the MSLP. This is based on the fact that clusters of CMIP5 and CMIP6 models tend to exhibit lower near-surface air temperature gradients during 2081-2100 (solid lines), indicating major contrasts between the ocean and northern South American landmass. This is consistent with previous studies suggesting that increasing temperatures over land in northern South America are one of the most prominent projected changes in the region (e.g. Reyer et al., 2017; Almazroui et al., 2021; Arias et al., 2021a).

The increasing contrasts of air temperature between the Tropical North Atlantic and the Andes-Amazon transition region could strengthen the wind circulation into the continent, which is not consistent with the projected weakening and shrinking of the OLLJ observed in Figures 3.1 to 3.3. This suggests that other processes aside

from the thermal contrast between the ocean and the landmass may influence these variations of the jet.

Following Martinez et al. (2022) and section 2.3.4, we evaluate the projected changes of MSLP, near-surface air temperature, and SSHF in northern South America, to assess changes in the contrasts between the northern and southern regions in the OLLJ corridor. Figures 3.5, 3.6, and 3.7 show the multimodel mean of the projected changes in these variables over northern South America. Red and blue rectangles represent the Orinoco and the Andes-Amazon regions, respectively, as used in previous sections. The projected changes for all clusters in CMIP5 and CMIP6 indicate decreasing MSLP through the OLLJ corridor (Figure 3.5) while increasing near-surface air temperature and SSHF (Figures 3.6 and 3.7, respectively) are projected, mainly over the Orinoco region (red rectangle). The pattern of increasing SSHF and air temperature over the Orinoco region tends to exhibit greater agreement among most of the models of the clusters (represented by dots), which in turn may be related to the regional gradients that modulate the intensity of the OLLJ.

Projected changes of MSLP are not particularly confined to the Orinoco region in all clusters and scenarios. By contrast, projections of air temperature and SSHF show higher positive changes over the Orinoco region (red rectangle) in contrast to the Andes-Amazon region (blue rectangle). The above suggests that MSLP changes mainly respond to variations in the projected warming across South America (e.g., Reboita et al., 2014, Llopart et al., 2020) but do not tend to adequately capture the signal of regional contrasts.

The variations in SSHF and near-surface air temperature, especially over the Orinoco region, may explain the projected weakening of the OLLJ as increasing SSHF in the northern part of the jet corridor enhances the temperature rise over that region and consequently, the changes in the gradients between the northern and southern OLLJ corridor. When comparing the projected changes under different scenarios, it is observed that higher radiative forcing induces major changes in the regional patterns of MSLP, air temperature, and SSHF, particularly over the Orinoco region.

Regarding our results in the projections of the wind field, they are contrary to other

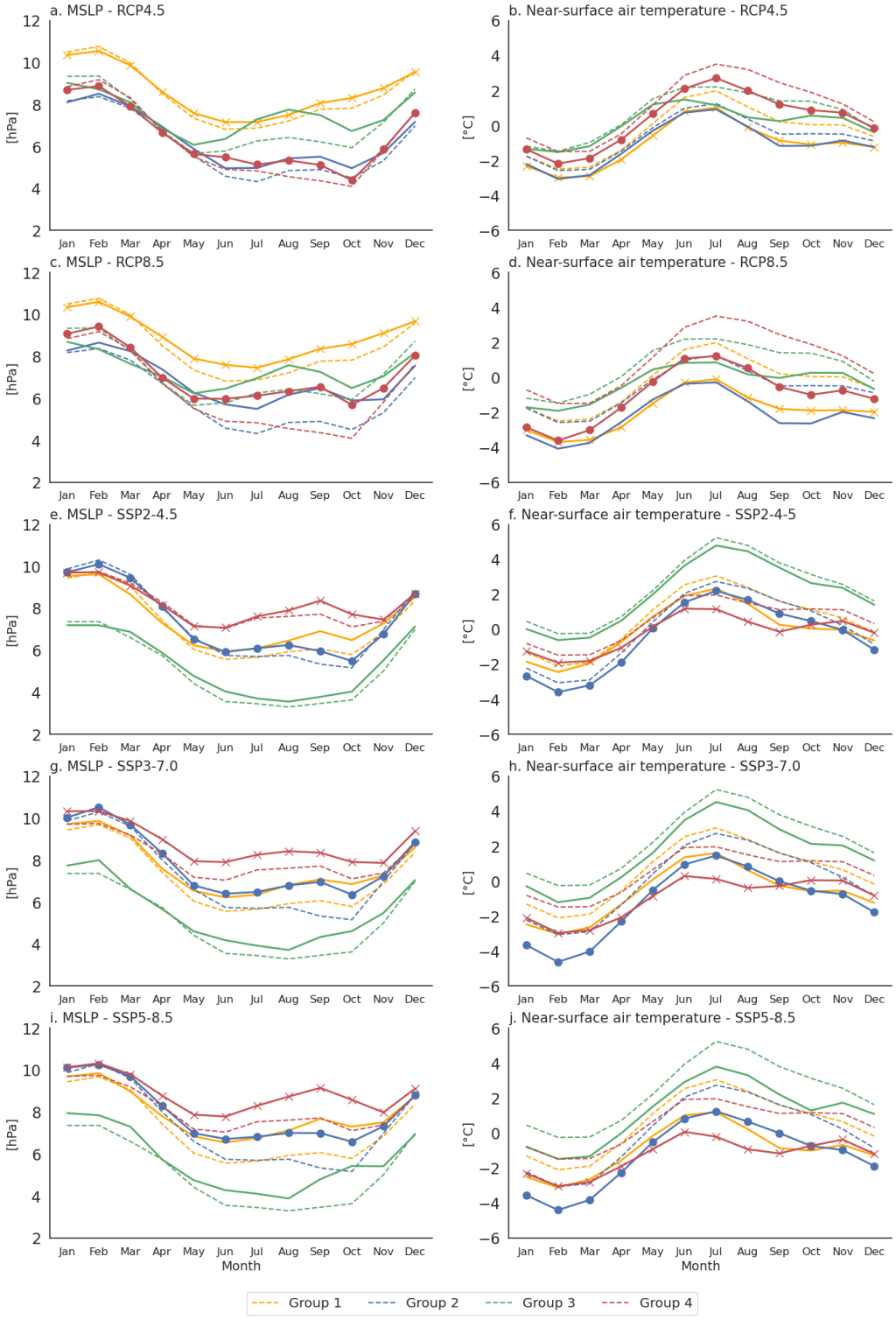

Figure 3.4: Annual cycle of the gradients of MSLP and near-surface air temperature for 2081-2100 (solid lines) and the historical simulations (dashed lines) under different scenarios: CMIP5 - RCP 4.5 (a, b), CMIP5 - RCP 8.5 (c, d), CMIP6 - SSP2-4.5 (e, f), CMIP6 - SSP3-7.0 (g, h) and CMIP6 - SSP5-8.5 (i, j). Dots represent the best group among the clusters of CMIP5 and CMIP6 models, and crosses represent the worst group.

studies that suggest a strengthening of the low-level wind circulation across South America (e.g., Torres-Alavez et al., 2021; Thaler et al., 2021). Such studies find this strengthening as a result of either the increasing air temperatures over South America that modulate ocean-continent gradients (Ortega and Arias, 2018; Thaler et al., 2021) or the changes in surface features that may influence its rugosity (Eiras-Barca et al., 2020). However, the differences between those studies and this work may be explained by the spatial scale of interests and the processes that lead to specific changes in more limited regions. Our results indicate that regional contrasts between the northern and southern regions of the OLLJ corridor can be more influential than the gradients between the ocean and the northern South American landmass when evaluating the projected changes in the features of the OLLJ.

3.3.3 Projected changes in atmospheric moisture transport and mid-level circulation

Section 2.3.5 analyzes the VIMF and wind circulation and specific humidity at 500 hPa fields simulated by the CMIP5 and CMIP6. Following this approach, this section focuses on the projected changes of the wind circulation and specific humidity patterns at 500 hPa under the different scenarios considered for the long term (2081-2100). It is considered that 500 hPa patterns could show moisture advection from the Atlantic Ocean, and changes in VIMF in northern South America during the activation period of the OLLJ. Figure 3.8 shows the projected changes of the 500 hPa wind field suggested by CMIP5 and CMIP6 models. Dots represent the agreement of the sign of the projected change by at least 80% of the models of each group. The projections suggest great contrasts among clusters in both CMIP5 and CMIP6. The predominant pattern in the projected changes in wind magnitude at 500 hPa is the increase in wind speed over northeastern South America, northern Amazon, Ecuador, and northern Peru, and decreases over the Caribbean Sea, northern Colombia, and northern Venezuela. A single cluster of CMIP5 models (Group 3) projects lower wind magnitude in mid-levels over the northern Amazon under both RCP4.5 and RCP8.5, however, the agreement among the models of the groups is limited to a small region. The above indicates that even though the projected patterns of

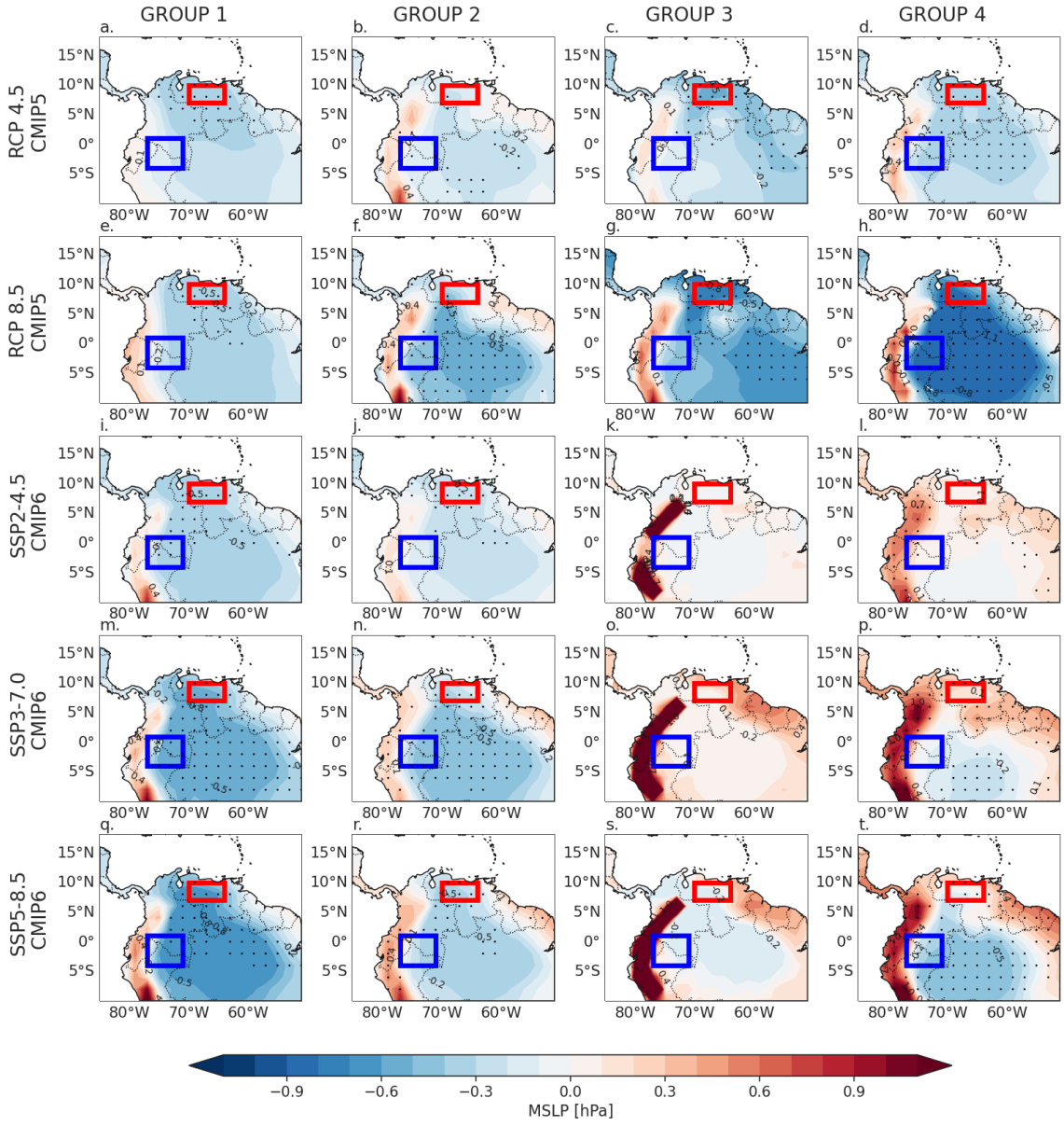

Figure 3.5: Projected changes of the MSLP during DJF for the long-term (2081-2100) under different scenarios: (a, b, c, d) RCP 4.5 and RCP 8.5 (e, f, g, h) for CMIP5, and SSP2-4.5 (i, j, k, l), SSP3-7.0 (m, n, o, p) and SSP 5-8.5 (q, r, s, t) for CMIP6. Dots represent grid cells where there is agreement on at least 80% of the models within each group in the sign of the projected change.Red and blue rectangles represent the Orinoco and the Andes-Amazon transition regions, respectively.

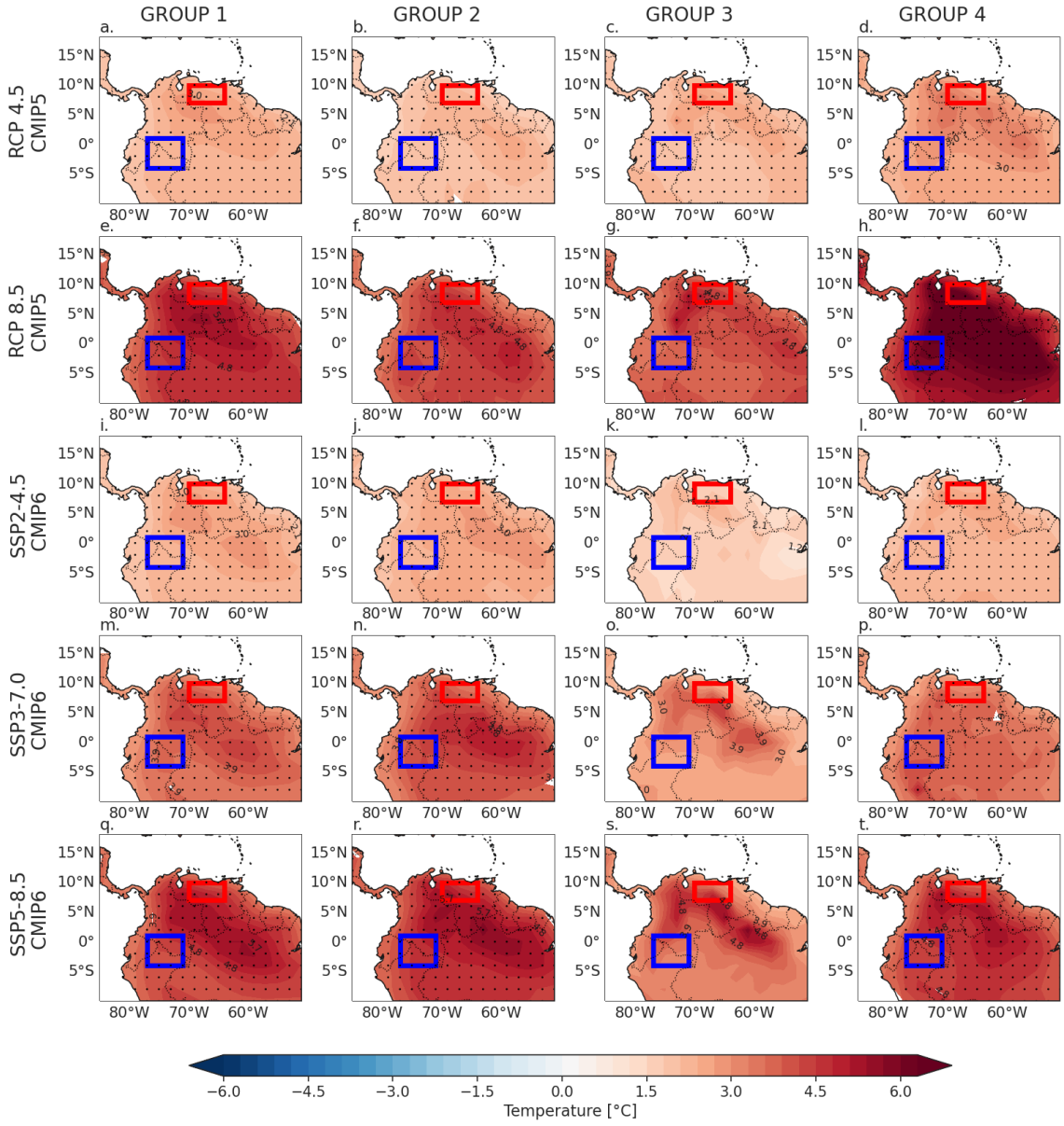

Figure 3.6: Projected changes of the near-surface air temperature during DJF for the long-term (2081-2100) under different scenarios: (a, b, c, d) RCP 4.5 and RCP 8.5 (e, f, g, h) for CMIP5, and SSP2-4.5 (i, j, k, l), SSP3-7.0 (m, n, o, p) and SSP 5-8.5 (q, r, s, t) for CMIP6. Dots represent grid cells where there is agreement on at least 80% of the models within each group in the sign of the projected change. Red and blue rectangles represent the Orinoco and the Andes-Amazon transition regions, respectively.

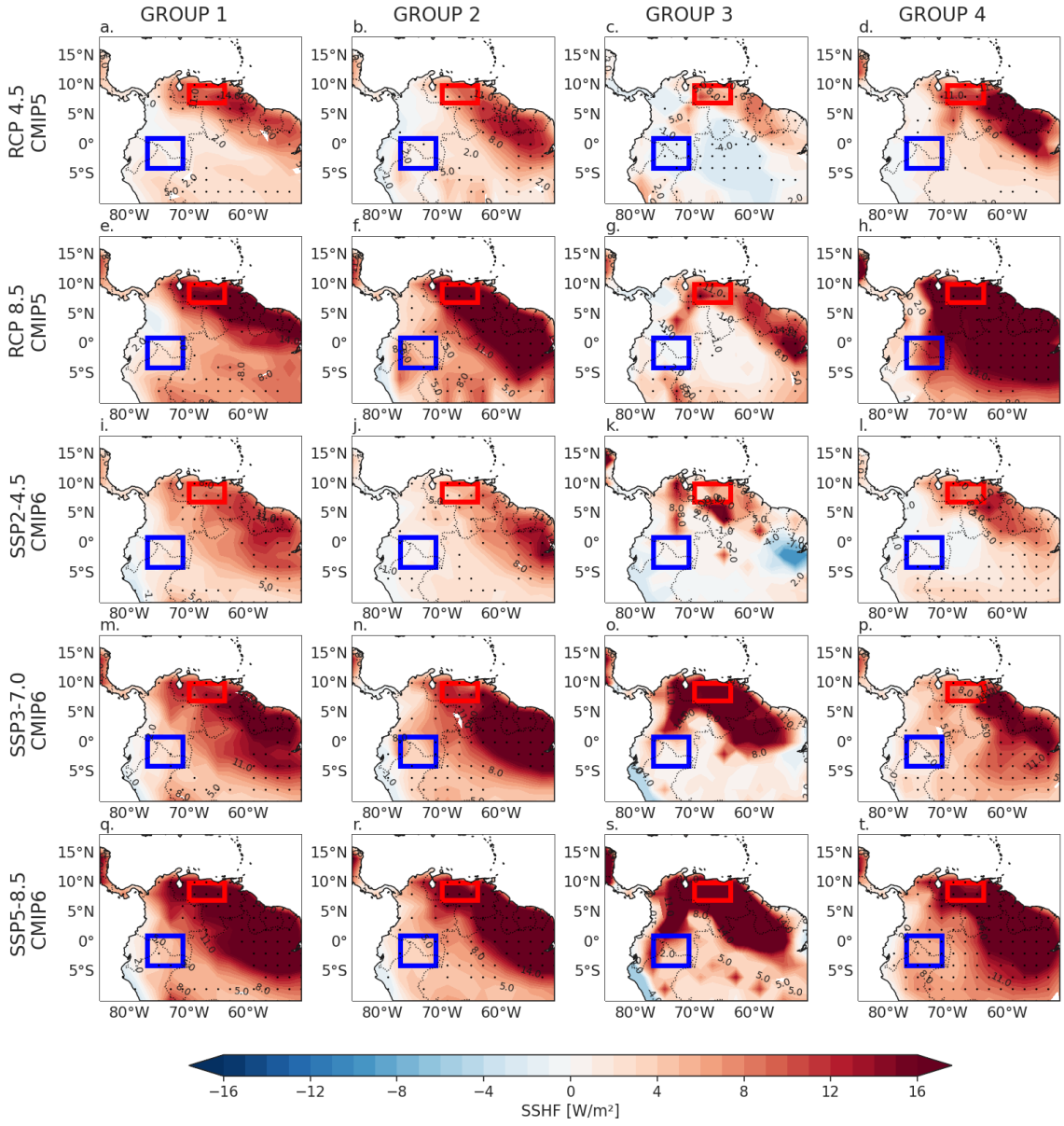

Figure 3.7: Projected changes of the SSHF during DJF for the long-term (2081-2100) under different scenarios: (a, b, c, d) RCP 4.5 and RCP 8.5 (e, f, g, h) for CMIP5, and SSP2-4.5 (i, j, k, l), SSP3-7.0 (m, n, o, p) and SSP 5-8.5 (q, r, s, t) for CMIP6. Dots represent grid cells where there is agreement on at least 80% of the models within each group in the sign of the projected change. Red and blue rectangles represent the Orinoco and the Andes-Amazon transition regions, respectively.

wind magnitude at mid-levels exhibit great variability among models, the increases of the wind magnitude over northeastern South America and northern Amazon and decreases over the Caribbean Sea are some of the predominant patterns shared by most of the clusters under all scenarios.

In terms of the specific humidity at 500 hPa (Figure 3.9), CMIP5 and CMIP6 models agree in the increase of the specific humidity in mid-levels for 2081-2100 over most of the northern South American landmass, independently of the scenario. The pattern of projected changes of 500 hPa specific humidity exhibits high agreement among models under different radiative forcing conditions, indicating the robustness of the results. Thus, these projections agree with previous studies that suggest the overall increase in specific humidity in the troposphere (Lee et al., 2021). The projected increase in specific humidity is stronger over the Amazon, while it exhibits lower projected changes over the Caribbean Sea. Models in Group 1 in CMIP5 (Figure 3.9a, e) suggest decreasing specific humidity over the Caribbean but without high agreement among the models.

The projections of the wind circulation and specific humidity at 500 hPa in northern South America, specifically over the northern part of the OLLJ corridor suggest increases in both wind magnitude and specific humidity at this level, although changes in the latter do not reach high values in comparison to the northern Amazon. The effect of enhanced wind speeds over the Orinoco region (red rectangle in Figure 2.1) can lead to increased moisture drag out of the region, which in turn can induce drier conditions at the surface, as previously identified in the analysis of precipitation projections over the region (Ortega and Arias, 2018; Zaninelli et al., 2018), thus enhancing the SSHF patterns over the Orinoco region (Figure 3.7).

Similar to the projections of specific humidity, the projected changes of the VIMF in northern South America, (Figure 3.10) suggest an increased VIMF (between 800 and 1000 hPa) during DJF by the end of the 21st century in most of the domain. This pattern is observed for both CMIP5 and CMIP6 models, with high agreement in the Caribbean sea and norteastern Brazil. However, some of the clusters project lower VIMF at the exit of the OLLJ (Figure 3.10h, i, m, q, r), which may be linked

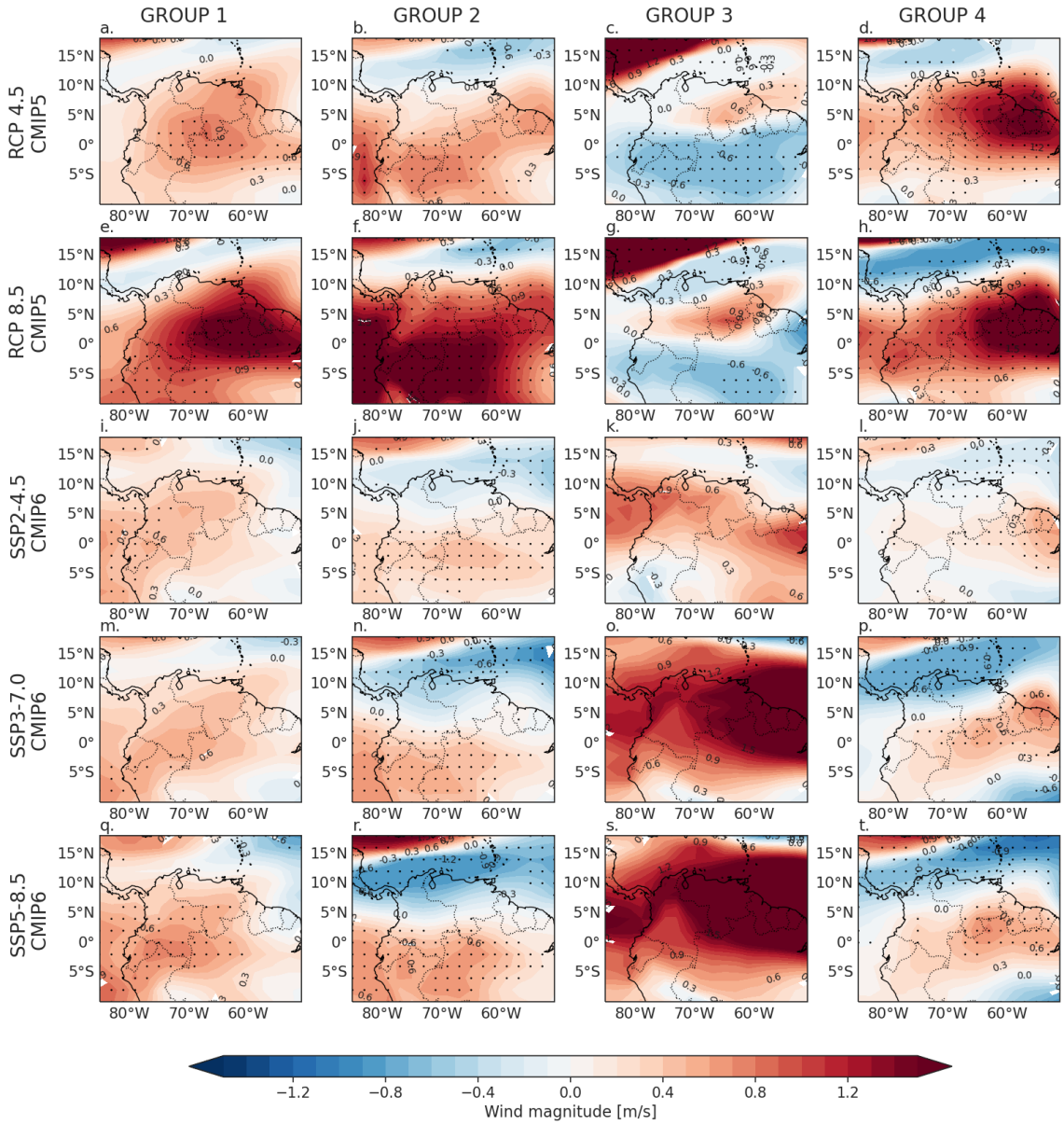

Figure 3.8: Projected changes of the wind field at 500 hPa during DJF for the long-term (2081-2100) under different scenarios: (a, b, c, d) RCP 4.5 and RCP 8.5 (e, f, g, h) for CMIP5, and SSP2-4.5 (i, j, k, l), SSP3-7.0 (m, n, o, p) and SSP 5-8.5 (q, r, s, t) for CMIP6. Dots represent grid cells where there is agreement on at least 80% of the models within each group in the sign of the projected change.

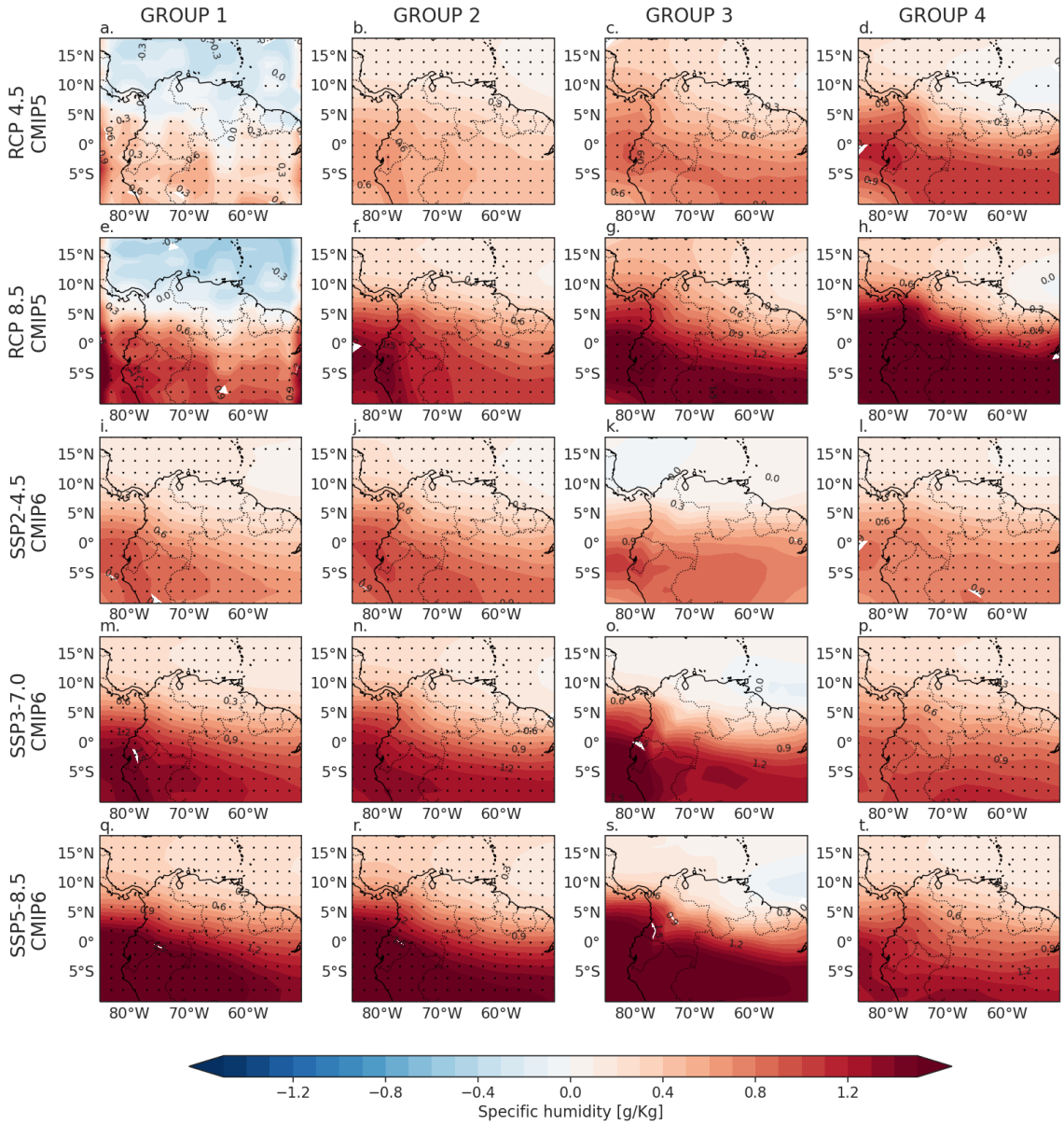

Figure 3.9: Projected changes of the specific humidity at 500 hPa during DJF for the long-term (2081-2100) under different scenarios: (a, b, c, d) RCP 4.5 and RCP 8.5 (e, f, g, h) for CMIP5, and SSP2-4.5 (i, j, k, l), SSP3-7.0 (m, n, o, p) and SSP 5-8.5 (q, r, s, t) for CMIP6. Dots represent grid cells where there is agreement on at least 80% of the models within each group in the sign of the projected change.

to the weakening of the low-level circulation along the Orinoco basin (section 3.3.1). These patterns through the jet corridor lose agreement among the models of each cluster, suggesting uncertainties in the effects of the weakening of the OLLJ. Previous research efforts for South America suggest the increase in atmospheric moisture transport through the continent, specifically from tropical areas (e.g., Soares and Marengo, 2009; Lee et al., 2018; Pascale et al., 2019). Nonetheless, our results focus on the Orinoco basin, where the jet modulates moisture transport at lower pressure levels, therefore its projected weakening implies changes in the regional patterns, particularly the reduction of the VIMF at the exit of the jet.

Finally, in section 2.3.5, we perform a simple linear regression analysis between the anomalies of the OLLJ index and the series of VIMF between 825 and 950 hPa in each grid cell in northern South America. We used the climate projections of the same models: HadGEM2-AO and IPSL-CM5A-LR from CMIP5 and MPI-ESM1-2-HR and KIOST-ESM from CMIP6, and the climate change scenarios considered were RCP4.5 and RCP8.5 for CMIP5, and SSP2-4.5 and SSP5-8.5 for CMIP6. The SSP3-7.0 scenario was not included due to data availability from the models. Figure 3.11 shows the results of the linear regression analysis with marked variations from each model's estimates in the historical experiment (Figure 2.22).

A marked change was obtained in RCP4.5 because of the absence of a statistically significant relationship between the OLLJ index and moisture patterns in the region with HadGEM2-AO (Figure 3.11a), suggesting that by the end of the century, the models' projection in this climate scenario does not capture any link. However, this result is not shared among other models and climate change scenarios. For RCP4.5, IPSL-CM5A-LR simulates a predominant statistically significant negative link over Brazil, while a positive influence of the OLLJ over VIMF is found in limited areas in southern and western Colombia. Regarding a more adverse climate change scenario for CMIP5, RCP8.5, both models exhibit marked changes, where the OLLJ seems to influence VIMF across the Orinoco basin, northern Colombia, and northern Brazil, that for HadGEM2-AO suggests the shrinking of the region where the OLLJ influences the VIMF, in comparison to its historical linkage where this influence region extends to Peru (Figure 2.22a).

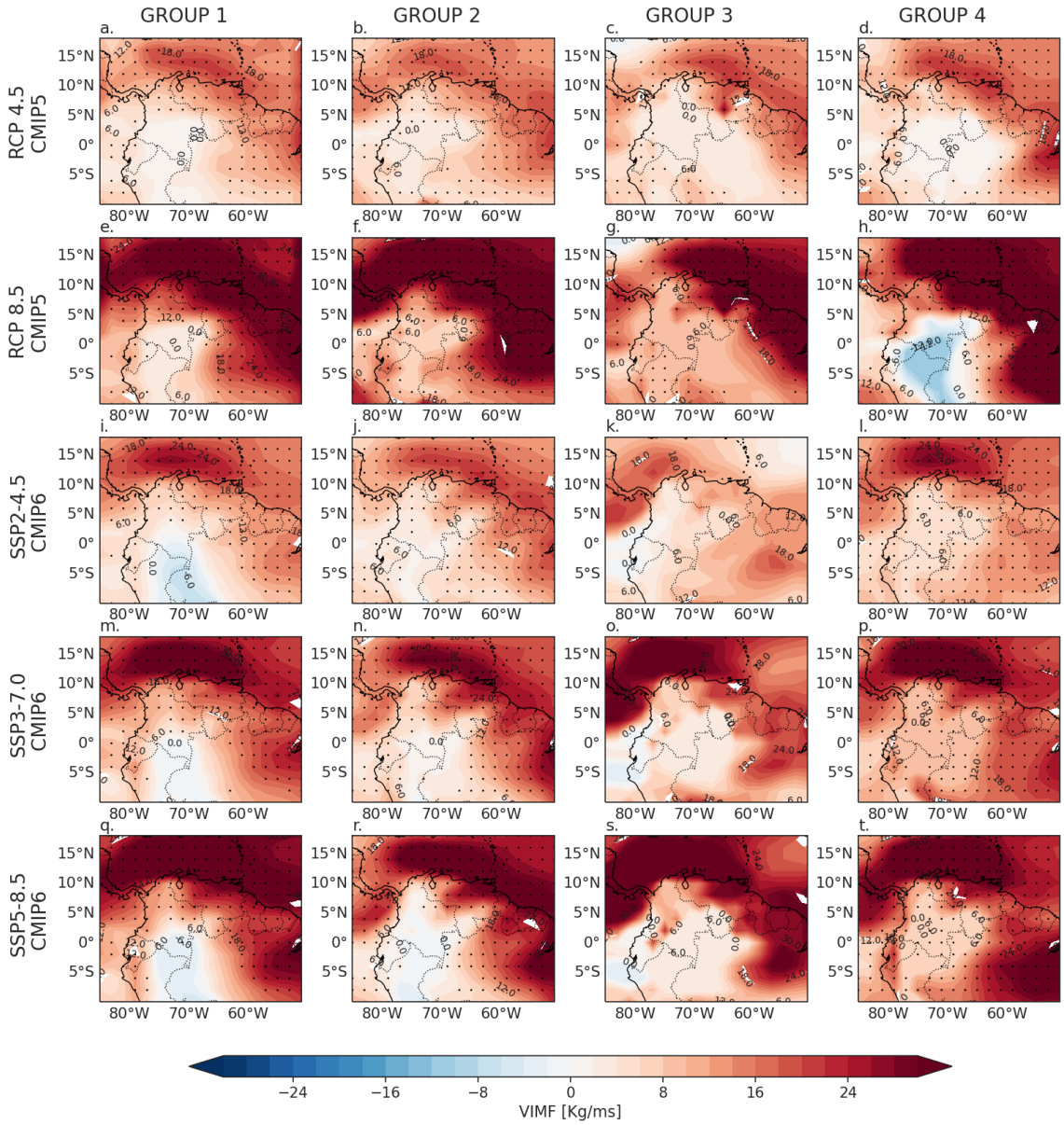

Figure 3.10: Projected changes of the VIMF between 1000 and 800 hPa during DJF for the long-term (2081-2100) under different scenarios: (a, b, c, d) RCP 4.5 and RCP 8.5 (e, f, g, h) for CMIP5, and SSP2-4.5 (i, j, k, l), SSP3-7.0 (m, n, o, p) and SSP 5-8.5 (q, r, s, t) for CMIP6. Dots represent grid cells where there is agreement on at least 80% of the models within each group in the sign of the projected change.

CMIP6 models also capture the previously observed pattern in SSP2-4.5 and SSP5-8.5 (Figure 3.11e, f, g, h), where the OLLJ role over VIMF in northern South America is positive in the Orinoco basin, but negative in western South America and northern Amazon. For KIOST-ESM (Figure 3.11f, h), changes are not so marked in SSP4.5, while in SSP5-8.5, the model suggests a reduction of the role of the OLLJ in VIMF. However, MPI-ESM1-2-HR (Figure 3.11e, g) does exhibit relevant changes, as the role of the activation of the OLLJ in high VIMF is limited to northeastern South America and the Orinoco basin. However, for the long-term, it does not extend to Peru, as the historical simulation suggests (Figure 2.22b).

These results highlight the role of the OLLJ in atmospheric moisture patterns in northern South America, as the projected weakening of this jet under different scenarios induce variations in the low-level VIMF in northern South America. Specifically, regions with high VIMF due to higher wind speed at the exit of the jet are limited to the Orinoco basin and northeastern South America. This relationship is observed for the reference data ERA5 (Figure 1.8d) and the historical simulation of the CMIP models (Figure 2.22). However, projections no longer exhibit this link over the southernmost regions (Figure 3.11).

3.4 Conclusions

This chapter focuses on the possible future changes of the OLLJ and other regional circulation patterns in northern South America linked to this LLJ. To do this, we used the projections under different emission scenarios from a set of CMIP5/CMIP6 models. These projections are estimated for the long term during the period 2081-2100. In addition, we analyze the projected changes in the wind speed during DJF from the OLLJ index throughout the 21st century. Besides, to have a wide overview of the possible projected changes of these features, we used different emission scenarios from both CMIP5 (RCP 4.5, RCP 8.5) and CMIP6 (SSP2-4.5, SSP3-7.0, SSP5-8.5).

The projected changes of the OLLJ assessed under different scenarios in CMIP5 and CMIP6 suggest the weakening of the LLJ through the 21st century. Focusing on the

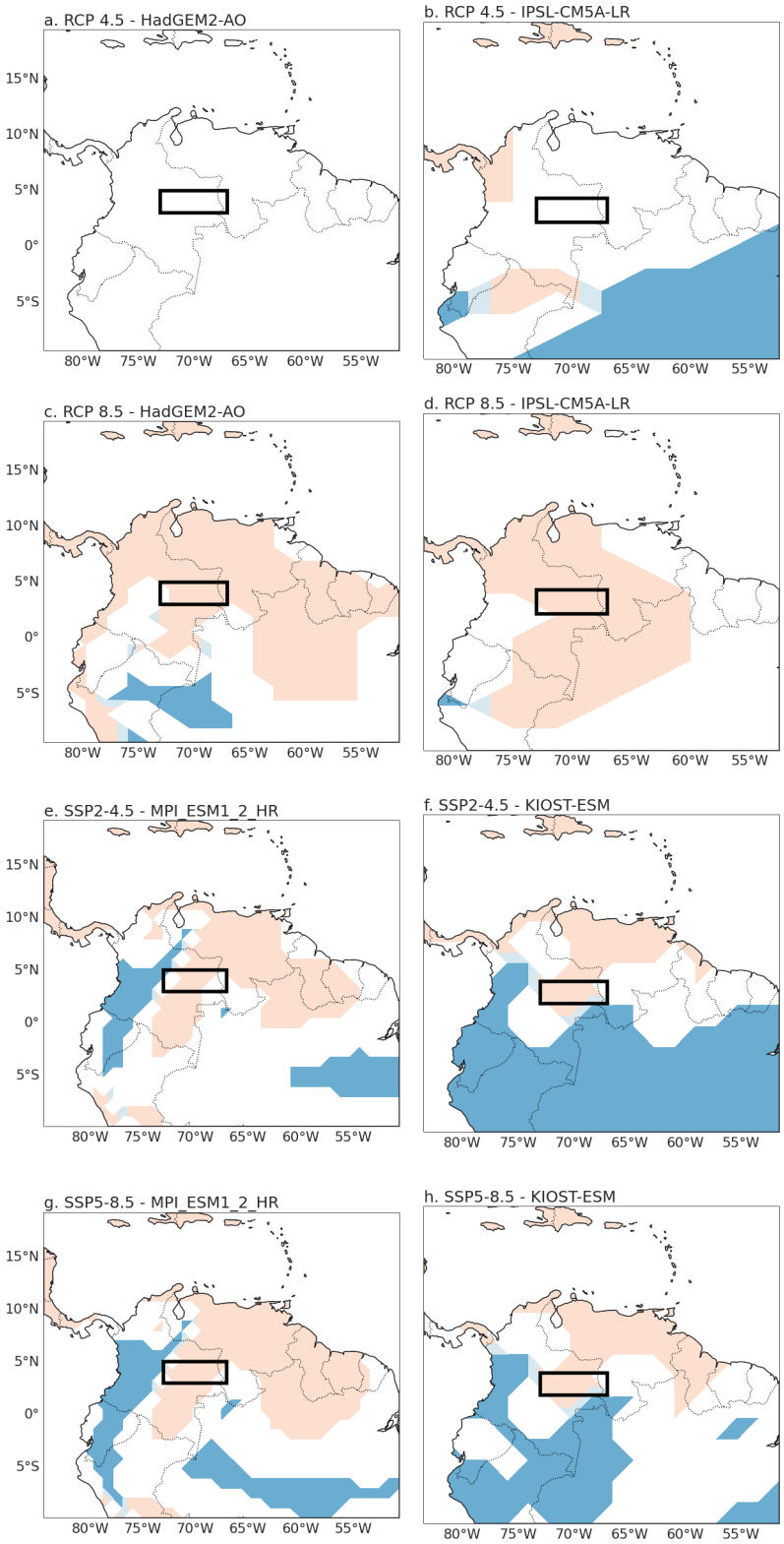

Figure 3.11: Simple linear regression for the long-term (2081-2100) between the anomalies of the OLLJ index estimated in region C3.4 (black rectangle) and the anomalies of VIMF in each cell from four selected CMIP models: (a, c) HadGEM2-AO and (b, d) IPSL-CM5A-LR for CMIP5 under the RCP4.5 and RCP8.5 scenarios, and (e, g) MPI-ESM1-2-HR and (f, h) KIOST-ESM for CMIP6 under the SSP2-4.5 and SSP5-8.5 scenarios. Colored cells represent a statistically significant relationship with an alpha of 0.05. Red colors represent a positive slope and blue colors represent a negative slope.

long-term (2081-2100), the projected weakening of the wind field in northern South America is extended over most of the landmass but models show a higher agreement in the sign of the change over the exit region of the jet (Figure 3.1). The above indicates that most of the models of each cluster exhibit projections of reduced wind speed along the Orinoco basin, specifically at the exit of the jet, which in turn may be related to a shrinking of the OLLJ through its spatial domain. These results imply changes in the patterns of atmospheric moisture transport in northern South America because of the role of the OLLJ in the moisture transport in the region (see section 1.3.4).

The assessment of the projected changes of the gradients of MSLP and near-surface air temperature between the Tropical North Atlantic and the Andes-Amazon transition region shown in Figure 3.4 indicates no clear relationship between the projections of the gradients between the ocean and the northern South American landmass and the weakening of the jet because the MSLP gradient did not exhibit major changes while the contrasts of near-surface air temperature increased as a result of the projected rise in temperature over the land. The above either would not generate larger changes in the wind circulation or on the contrary, would increase the wind speed associated with the OLLJ as a result of an enhanced surface temperature gradient.

Even though the projected changes of the OLLJ cannot be related to variations in the gradients between the ocean and the South American landmass, the analysis of the projections of SSHF, MSLP, and air temperature in northern South America and their contrasts between the northern and southern regions of the OLLJ corridor suggests the influence of these regional patterns on the projected changes in the OLLJ. Most of the clusters in CMIP5 and CMIP6 project decreases in MSLP over northern South America (Figure 3.5), independently of the scenario, while increasing near-surface air temperature and SSHF is projected particularly in the Orinoco region (Figures 3.6 and 3.7). These regional changes, especially for SSHF, can modulate the gradients along the jet corridor, inducing the projected weakening and shrinking of the OLLJ by the late 21st century.

The climate projections of wind circulation, and specific humidity at mid-levels for DJF indicate a generalized increase of these variables along the OLLJ corridor by the end of the century, with high agreement among the CMIP5/CMIP6 models (Figures 3.8 and 3.9). However, the projected changes of VIMF along the exit of the jet of some clusters suggest its decrease by the end of the century in response to the weakening of the jet (Figure 3.10). The changes in wind circulation and specific humidity at 500 hPa are in agreement with the surface variables, suggesting that drier conditions over the Orinoco region (red rectangle in Figure 2.1), which seems to be related to the weakening of the OLLJ, can be linked to a strengthening of the wind flow at mid-levels over the Orinoco that in turn can induce to enhanced moisture transport out of the region, enhancing drier atmospheric characteristics in northeastern South America. The projection of drier conditions over the Orinoco region is suggested by the most recent report of the IPCC, which shows increased consecutive dry days as well as more frequent and intense agricultural and ecological droughts over this region (Arias et al., 2021a; Seneviratne et al., 2021).

Except for the VIMF changes, which show little agreement among models, the patterns tend to be shared by most of the clusters in CMIP5 and CMIP6, with a high agreement in key regions of northern South America, adding robustness to these results. On the other hand, the magnitude of the changes is enhanced for the scenarios with the highest radiative forcing (RCP8.5 and SSP5-8.5). Our results are consistent among the different scenarios considered, highlighting the robustness of the possible future changes of the OLLJ and some regional features related to the low and mid-level wind circulation in northern South America.

On the other hand, the simple linear regression analysis indicates that under the projected changes of the OLLJ (its weakening), low-level VIMF in northern South America is also expected to variate. The intensification of the wind speed at the exit of the OLLJ is set to enhance VIMF in northeastern South America and the Orinoco basin; however, this link is not observed across Peru, which indicates the shrinking of the region where the OLLJ enhances VIMF, thus representing major variations in moisture patterns in the region.

3.5 Supplementary material

Table S3.1: Slope of the projected changes of the OLLJ index for DJF in m/s per decade. All trends are statistically significant, and minus indicates decreasing trends according to the Mann-Kendall test. Blank spaces indicate the lack of a statistically significant trend.

	Group 1	**Group 2**	**Group 3**	**Group 4**
RCP 4.5 CMIP5	-0.050	-0.018	-0.042	-0.030
RCP 8.5 CMIP5	-0.063	-0.023	-0.102	-0.054
SSP2-4.5 CMIP6	-0.024	-0.037		-0.052
SSP3-7.0 CMIP6	-0.041	-0.039		-0.040
SSP5-8.5 CMIP6	-0.054	-0.067		-0.058

Chapter 4

Final remarks

Through this study, we assessed the main features of the OLLJ, the links with atmospheric moisture transport and moisture-related processes in northern South America, and the ability of GCMs included in CMIP5 and CMIP6 to simulate these features in the historical experiment. Additionally, we focused on the 21st century projections of these aspects under different emission scenarios.

Chapter 1 focused on the characterization of the OLLJ through a reanalysis database (ERA5), after its validation with radiosonde data in the Colombian Llanos (Figure 1.2). We analyzed the annual and diurnal cycles of the jet between 825 and 950 hPa. Among our main results, we find that the OLLJ reaches its maximum activation during DJF. On the diurnal scale, the peak intensity of the jet occurs during the nighttime and early morning hours (Figures 1.4 and 1.5), which agrees with previous studies (Torrealba and Amador, 2010; Jiménez-Sánchez et al., 2019, 2020; Martínez et al., 2022). The seasonal activation of the OLLJ is modulated by the strengthening of the northeasterly trade winds in the Orinoco basin due to the meridional gradient of MSLP and air temperature between the Atlantic Ocean/Caribbean Sea and the South American landmass. On the other hand, the variations of the diurnal cycle of the jet, which are consistent with the occurrence of a nocturnal low-level jet, are strongly modulated by the PBL evolution along the day (Figure 1.6). Even though we only focused on the PBL features during daytime and nighttime to explain the diurnal variations of the LLJ, it is relevant to consider that other processes may also influence the evolution of the OLLJ in the diurnal scale (Jiménez-Sánchez et al., 2020).

Regarding the atmospheric moisture patterns associated with the LLJ, our results suggest that VIMF in lower pressure levels increases during DJF along the Orinoco basin (Figure 1.7), which could be modulated by the OLLJ activity. Besides, from a simple linear regression analysis, we found that the effect of the OLLJ on the atmospheric moisture flux, divergence, and precipitation in northern South America varies across the region, depending on if it is considered the entrance or the exit regions of the OLLJ (Figures 1.8, 1.9 and 1.10). The jet activity at its entrance is related to enhanced VIMF and VIMD in the Venezuelan Llanos and enhanced moisture convergence and precipitation in the Colombian Llanos and northern Amazon. At its exit, the OLLJ causes VIMF and divergence through the Orinoco basin, while its effects on precipitation and moisture convergence migrate to northern Brazil and the Colombian Andes, with a lagged response between the jet activity and its effect on precipitation.

On the other hand, the interannual strengthening of the OLLJ is influenced by regional variations in the gradients of MSLP, near-surface air temperature, and SSHF between the northern and southern OLLJ corridor. In particular, strong (weak) OLLJ events occur with increased (decreased) MSLP and decreased (increased) air temperature and SSHF gradients (Figure 1.13). Additionally, the occurrence of strong (weak) OLLJ events tends to couple with La Niña (El Niño) events, suggesting the modulation of ENSO in the interannual variability of the OLLJ, as discussed by Builes-Jaramillo et al. (2022a).

After performing the description of the observed features of the OLLJ as depicted by ERA5, Chapter 2 focused on the simulation of the OLLJ by different CMIP5/CMIP6 models in the historical experiment. We analyzed the information of 37 CMIP5 and 34 CMIP6 models and classified the set of models in terms of their seasonal simulation of northern South America's low-level wind circulation through the PCC and the RMSE. The evaluation of the performance of the models was based on the horizontal wind between 825 and 950 hPa, the cross-section and vertical structure of the wind field at the exit of the jet, and the monthly variations of the meridional wind using the OLLJ index. After obtaining the PCC and the RMSE of those estimates concerning to ERA5, these metrics were used as the input for the factor analysis,

and the resulting factors were, at the same time, the input to the cluster analysis (section 2.3.2).

The classification method suggests four groups of models in each CMIP phase. CMIP5 groups exhibited significant differences in their simulation of the main features of the OLLJ. In contrast, CMIP6 models tend to adequately simulate the spatial and temporal features of the OLLJ, showing a similar performance (section 2.3.3). Regarding the links between the simulation of the mechanisms that modulate the activation of the OLLJ (meridional gradients) and the representation of the OLLJ itself, the performance of the CMIP5 models appears to be more influenced by an accurate simulation of the MSLP and near-surface air temperature gradients between the ocean and the South American landmass (Figure 2.14) than CMIP6 models (Figure 2.15).

On the other hand, following Martinez et al. (2022) and the results from Chapter 1, the assessment of how CMIP5/CMIP6 models link the interannual variations of the OLLJ intensity with the regional contrasts of MSLP, air temperature, and SSHF between the Orinoco and the Andes-Amazon transition region (red and blue rectangle in Figure 2.1), indicates that models capture the regional variations associated with changes in the jet strengthening independently of their simulation of the main features of the OLLJ (Figures 2.16 to 2.19). These findings show that GCMs can represent the atmospheric circulation in northern South America, as they can associate fluctuations in the gradients between the northern and southern regions of the OLLJ corridor with stronger or weaker wind circulation in the basin. Recently, Olmo et al. (2022) showed that some of the CMIP6 models are able to represent the low-level circulation over tropical South America, based on a weather pattern classification approach. This highlights that, although CMIP6 models still have large biases simulating variables like precipitation in the region (Almazroui et al., 2021; Arias et al., 2021b; Ortega et al., 2021), they may have a better representation of the dynamic process associated with precipitation.

Finally, Chapter 3 focused on the analysis of the projected changes of the OLLJ under different scenarios: RCP4.5 and RCP8.5 for CMIP5, and SSP2-4.5, SSP3-7.0,

and SSP5-8.5 for CMIP6. The most notable change of the OLLJ in the long-term (2081-2100) is its weakening and shrinking, as projected changes indicate reduced wind speed by the end of the century along the Orinoco basin, specifically at the jet exit (Figures 3.1 to 3.3). This pattern is observed in CMIP5 and CMIP6 models under all the scenarios considered. However, the projected changes are greater for scenarios with higher radiative forcing (RCP8.5 and SSP5-8.5).

The projected weakening of the OLLJ may be driven by changes in the regional gradients of MSLP, air temperature, and mainly, SSHF between the Orinoco and the Andes-Amazon transition region instead of the influence of meridional gradients between the Tropical North Atlantic and the Amazon (section 3.3.2). Projected changes in the gradients between the Orinoco and the Andes-Amazon transition region are strongly modulated by increased SSHF over the Orinoco, which modifies the regional gradients in the OLLJ corridor.

Figure 4.1 shows a general schematic of the main climatological features and projected changes for the low and mid-level circulation in northern South America in association with the OLLJ. The activation of the OLLJ occurs due to the meridional gradients between the Tropical North Atlantic and the South American landmass, with high pressure over the ocean and low pressure over the land. These gradients enhance the northeasterly trade winds circulation into the Orinoco basin, which contributes to the strengthening of the OLLJ during DJF (Figure 4.1a). The activation of the OLLJ occurs alongside local higher sensible heat flux from the surface (SSHF) in the northern part of the jet corridor due to the drier conditions of this region, where regional variations of the SSHF spatial distribution, alongside changes in air temperature and MSLP, can modulate the interannual intensity of the OLLJ.

Regarding the projected changes of the OLLJ (Figure 4.1b), the main projected variation is the weakening of the OLLJ during DJF, especially at its exit region, which in turn suggests the shrinking of the LLJ in its spatial domain. This change is expected to occur due to increasing SSHF over the northern part of the jet corridor (northeastern South America) as a consequence of increasing wind circulation at mid-levels (500 hPa) that influences the atmospheric moisture content over the region

(increased moisture transport out of the region), enhancing drier conditions at the surface. On the other hand, projections around the meridional gradient between the Tropical North Atlantic and the South American landmass suggest its strengthening by the end of the 21st century; therefore, the projected changes of the OLLJ may be more influenced by regional variations along the jet corridor than by ocean-landmass contrasts.

According to our results, the linkage between mid-level atmospheric moisture transport and near-surface conditions can influence the enhancement of future drier conditions in the Orinoco basin. The projected changes in wind circulation and specific humidity at 500 hPa over the Orinoco region indicate that models project enhanced mid-level wind speed and specific humidity in northeastern South America by the end of the 21st century, which means stronger wind circulation that can drag the moisture out of the region, inducing drier conditions. The projection of drier conditions over the Orinoco region is suggested by the most recent report of the IPCC, which shows increased consecutive dry days as well as more frequent and intense agricultural and ecological droughts over this region (Arias et al., 2021a; Seneviratne et al., 2021). This is particularly important since the Orinoco and the Guiana Shield are very important regions in terms of biodiversity in South America (Bovolo et al., 2018). This suggests the importance of addressing research focused on this region given it is one of the most understudied regions in South America.

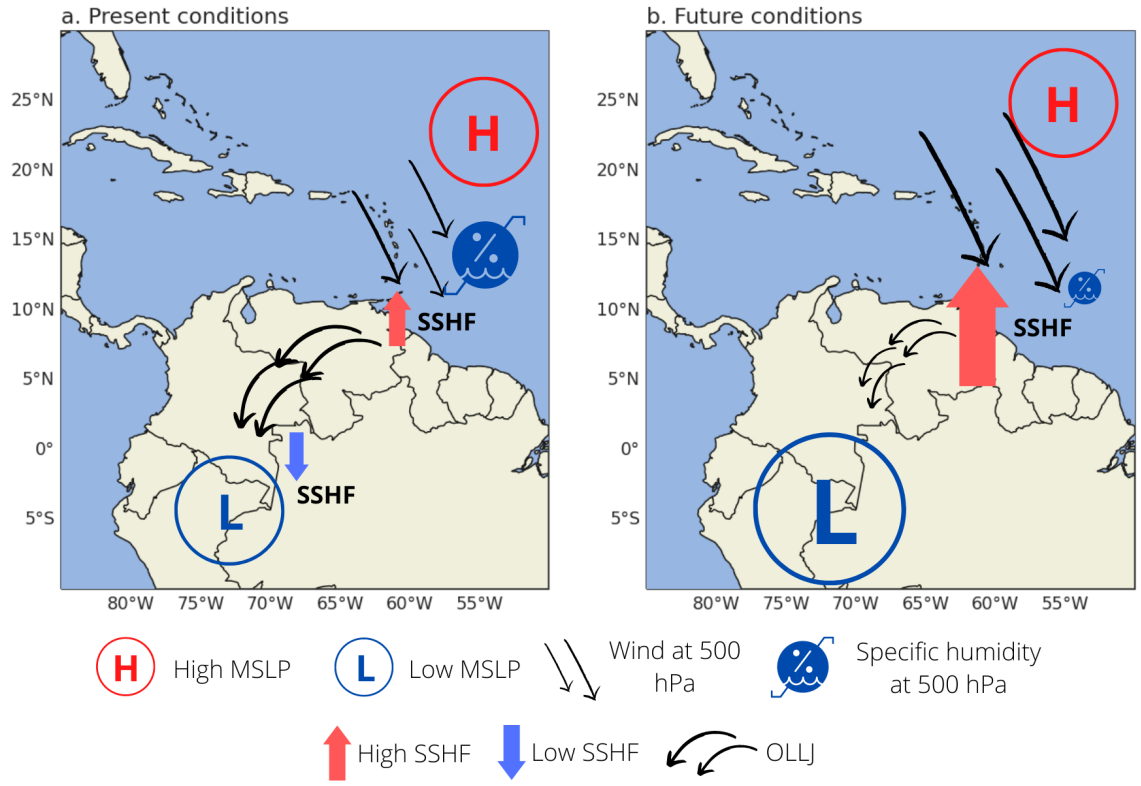

Figure 4.1: General schematics of the (a) main climatological features during the historical period and (b) projected changes by the end of the 21st century under different emission scenarios for the low and mid-level circulation in northern South America during DJF, in association with the OLLJ. Bigger (smaller) arrows and symbols indicate an increase (decrease) under future conditions.

References

Acosta, R. P., & Huber, M. (2017). The neglected Indo-Gangetic Plains low-level jet and its importance for moisture transport and precipitation during the peak summer monsoon. Geophysical Research Letters, 44(16), 8601-8610. https://doi.org/10.1002/2017GL074440

Algarra, I., Eiras-Barca, J., Nieto, R., & Gimeno, L. (2019). Global climatology of nocturnal low-level jets and associated moisture sources and sinks. Atmospheric Research, 229, 39-59. https://doi.org/10.1016/j.atmosres.2019.06.016

Al-Ghussain, L. (2019). Global warming: Review on driving forces and mitigation. Environmental Progress & Sustainable Energy, 38(1), 13-21. https://doi.org/10.1002/ep.13041

Almazroui, M., Ashfaq, M., Islam, M. N., Rashid, I. U., Kamil, S., Abid, M. A., ... & Sylla, M. B. (2021). Assessment of CMIP6 performance and projected temperature and precipitation changes over South America. Earth Systems and Environment, 5(2), 155-183. https://doi.org/10.1007/s41748-021-00233-6

Allan, R. P., Barlow, M., Byrne, M. P., Cherchi, A., Douville, H., Fowler, H. J., ...& Zolina, O. (2020). Advances in understanding large-scale responses of the water cycle to climate change. Annals of the New York Academy of Sciences, 1472(1), 49-75. https://doi.org/10.1111/nyas.14337

Amador Astúa, J. A. (1998). A climate feature of the tropical Americas: The trade wind easterly jet.

Amador, J. A. (2008). The intra-Americas sea low-level jet: Overview and future research. Annals of the New York Academy of Sciences, 1146(1), 153-188. https://doi.org/10.1196/annals.1446.012

Anjos, L. J., & de Toledo, P. M. (2018). Measuring resilience and assessing vulnerability of terrestrial ecosystems to climate change in South America. PloS one, 13(3), e0194654. https://doi.org/10.1371/journal.pone.0194654

Anjos, L. J., de Souza, E. B., Amaral, C. T., Igawa, T. K., ? de Toledo, P. M. (2021). Future projections for terrestrial biomes indicate widespread warming and moisture reduction in forests up to 2100 in South America. Global Ecology and Conservation, 25, e01441. https://doi.org/10.1016/j.gecco.2020.e01441

Anselmo, E. M., Schumacher, C., & Machado, L. A. (2020). The Amazonian low-level jet and its connection to convective cloud propagation and evolution. Monthly Weather Review, 148(10), 4083-4099. https://doi.org/10.1175/MWR-D-19-0414.1

Arias, P., Bellouin, N., Coppola, E., Jones, R., Krinner, G., Marotzke, J., ... & Zickfeld, K. (2021a). Climate Change 2021: The Physical Science Basis. Contribution of Working Group14 I to the Sixth Assessment Report of the Intergovernmental Panel on Climate Change; Technical Summary. doi:10.1017/9781009157896.002

Arias, P. A., Garreaud, R., Poveda, G., Espinoza, J. C., Molina-Carpio, J., Masiokas, M., ... & van Oevelen, P. J. (2021b). Hydroclimate of the Andes Part II: Hydroclimate variability and sub-continental patterns. Frontiers in Earth Science, 8, 666. doi: 10.3389/feart.2020.505467

Arias, P. A., Martínez, J. A., Mejía, J. D., Pazos, M. J., Espinoza, J. C., & Wongchuig-Correa, S. (2020). Changes in normalized difference vegetation index in the Orinoco and Amazon River Basins: Links to tropical atlantic surface temperatures. Journal of Climate, 33(19), 8537-8559. doi: 10.1175/JCLI-D-19-0696.1

Arora, V. K., Scinocca, J. F., Boer, G. J., Christian, J. R., Denman, K. L., Flato, G. M., ... & Merryfield, W. J. (2011). Carbon emission limits required to satisfy future representative concentration pathways of greenhouse gasses. Geophysical Research Letters, 38(5). https://doi.org/10.1029/2010GL046270

Bao, Y., Song, Z., & Qiao, F. (2020). FIO-ESM version 2.0: Model description and evaluation. Journal of Geophysical Research: Oceans, 125(6), e2019JC016036. https://doi.org/10.1029/2019JC016036

Barichivich, J., Gloor, E., Peylin, P., Brienen, R. J., Schöngart, J., Espinoza, J. C., & Pattnayak, K. C. (2018). Recent intensification of Amazon flooding extremes driven by strengthened Walker circulation. Science advances, 4(9), eaat8785. doi: 10.1126/sciadv.aat8785

Beck, H. E., Zimmermann, N. E., McVicar, T. R., Vergopolan, N., Berg, A., & Wood, E. F. (2018). Present and future Köppen-Geiger climate classification maps at 1-km resolution. Scientific data, 5(1), 1-12. doi: 10.1038/sdata.2018.214

Bellouin, N., Collins, W. J., Culverwell, I. D., Halloran, P. R., Hardiman, S. C., Hinton, T. J., ... & Wiltshire, A. (2011). The HadGEM2 family of met office unified model climate configurations. Geoscientific Model Development, 4(3), 723-757. doi:10.5194/gmd-4-723-2011

Bentsen, M., Bethke, I., Debernard, J. B., Iversen, T., Kirkevåg, A., Seland, Ø., ... & Kristjansson, J. E. (2013). The Norwegian Earth System Model, NorESM1-M–Part 1: description and basic evaluation of the physical climate. Geoscientific Model Development, 6(3), 687-720. https://doi.org/10.5194/gmd-6-687-2013

Bethke, I., Wang, Y., Counillon, F., Keenlyside, N., Kimmritz, M., Fransner, F., ... & Eldevik, T. (2021). NorCPM1 and its contribution to CMIP6 DCPP. Geoscientific Model Development, 14(11), 7073-7116. https://doi.org/10.5194/gmd-14-7073-2021

Bi, D., Dix, M., Marsland, S., O'Farrell, S., Sullivan, A., Bodman, R., ... & Heerdegen, A. (2020). Configuration and spin-up of ACCESS-CM2, the new generation Australian Community Climate and Earth System Simulator Coupled Model. Journal of Southern Hemisphere Earth Systems Science, 70(1), 225-251. https://doi.org/10.1071/ES19040

Bonner, W. D. (1968). Climatology of the low-level jet. Monthly Weather Review, 96(12), 833-850. https://doi.org/10.1175/1520-0493(1968)096<0833:COTLLJ>2.0.CO;2

Boucher, O., Servonnat, J., Albright, A. L., Aumont, O., Balkanski, Y., Bastrikov, V., ... & Vuichard, N. (2020). Presentation and evaluation of the IPSL-CM6A-LR cli-

mate model. Journal of Advances in Modeling Earth Systems, 12(7), e2019MS002010. https://doi.org/10.1029/2019MS002010

Bovolo, C. I., Wagner, T., Parkin, G., Hein-Griggs, D., Pereira, R., & Jones, R. (2018). The Guiana Shield rainforests—overlooked guardians of South American climate. Environmental Research Letters, 13(7), 074029. https://doi.org/10.1088/1748-9326/aacf60

Bracegirdle, T. J., Lu, H., & Robson, J. (2022). Early-winter North Atlantic low-level jet latitude biases in climate models: implications for simulated regional atmosphere-ocean linkages. Environmental Research Letters, 17(1), 014025. https://doi.org/10.1088/1748-9326/ac417f

Braz, D. F., Ambrizzi, T., Da Rocha, R. P., Algarra, I., Nieto, R., & Gimeno, L. (2021). Assessing the moisture transports associated with nocturnal low-level jets in continental south america. Frontiers in Environmental Science, 108. https://doi.org/10.338/fenvs.2021.657764

Builes-Jaramillo, A., Yepes, J., & Salas, H. D. (2022a). The Orinoco Low-Level Jet and its association with the hydroclimatology of northern South America. Journal of Hydrometeorology, 23(2), 209-223. doi: 10.1175/JHM-D-21-0073.1.

Builes-Jaramillo, A., Yepes, J., & Salas, H. D. (2022b). The Orinoco Low-Level Jet during El Niño-Southern Oscillation. International Journal of Climatology, 1-15. doi: 10.1002/joc.7681.

Burrows, S. M., Maltrud, M., Yang, X., Zhu, Q., Jeffery, N., Shi, X., ... & Leung, L. R. (2020). The DOE E3SM v1. 1 biogeochemistry configuration: Description and simulated ecosystem-climate responses to historical changes in forcing. Journal of Advances in Modeling Earth Systems, 12(9), e2019MS001766. https://doi.org/10.1029/2019MS001766

Carvajal-Romo, G., Valderrama-Mendoza, M., Rodríguez-Urrego, D., & Rodríguez-Urrego, L. (2019). Assessment of solar and wind energy potential in La Guajira, Colombia: Current status, and future prospects. Sustainable Energy Technologies and Assessments, 36, 100531. https://doi.org/10.1016/j.seta.2019.100531

Castellanos, E., M.F. Lemos, L. Astigarraga, N. Chacón, N. Cuvi, C. Huggel, L. Miranda, M. Moncassim Vale, J.P. Ometto, P.L. Peri, J.C. Postigo, L. Ramajo, L. Roco, & M. Rusticucci (2022). Central and South America. In: Climate Change 2022: Impacts, Adaptation and Vulnerability. Contribution of Working Group II to the Sixth Assessment Report of the Intergovernmental Panel on Climate Change [H.-O. Pörtner, D.C. Roberts, M. Tignor, E.S. Poloczanska, K. Mintenbeck, A. Alegría, M. Craig, S. Langsdorf, S. Löschke, V. Möller, A. Okem, B. Rama (eds.)]. Cambridge University Press, Cambridge, UK and New York, NY, USA, pp. 1689–1816, doi:10.1017/9781009325844.014.

CCSP. (2008). Climate Models: An Assessment of Strengths and Limitations. A Report by the U.S. Climate Change Science Program and the Subcommittee on Global Change Research [Bader D.C., C. Covey, W.J. Gutowski Jr., I.M. Held, K.E. Kunkel, R.L. Miller, R.T. Tokmakian and M.H. Zhang (Authors)]. Department of Energy, Office of Biological and Environmental Research, Washington, D.C., USA, 124 pp.

Ceron, W. L., Kayano, M. T., Andreoli, R. V., Avila-Diaz, A., Ayes, I., Freitas, E. D., ... & Souza, R. A. (2021). Recent intensification of extreme precipitation events in the La Plata Basin in Southern South America (1981–2018). Atmospheric Research, 249, 105299. https://doi.org/10.1016/j.atmosres.2020.105299

Chai, R., Mao, J., Chen, H., Wang, Y., Shi, X., Jin, M., ... & Wullschleger, S. D. (2021). Human-caused long-term changes in global aridity. npj Climate and Atmospheric Science, 4(1), 1-8. https://doi.org/10.1038/s41612-021-00223-5

Chen, D., Rojas, M., Samset, B., Cobb, K., Diongue, A., Niang, A., ... & Tréguier, A. (2021). Framing, Context, and Methods. in Climate Change 2021: The Physical Science Basis. Contribution of Working Group I to the Sixth Assessment Report of the Intergovernmental Panel on Climate Change, 215. doi:10.1017/9781009157896.003.

Cherchi, A., Fogli, P. G., Lovato, T., Peano, D., Iovino, D., Gualdi, S., ... & Navarra, A. (2019). Global mean climate and main patterns of variability in the CMCC-CM2 coupled model. Journal of Advances in Modeling Earth Systems, 11(1), 185-209. https://doi.org/10.1029/2018MS001369

Churio-Silvera, O., Vanegas, M., & Barros, P. (2018). Status of Non-Conventional Sources of Energy in Colombia: A Look at the Challenges and Opportunities of the Electric Sector. Contemporary Engineering Sciences, 11(44), 2163-2172. https://doi.org/10.12988/ces.2018.85221

Collins, M., Knutti, R., Arblaster, J., Dufresne, J. L., Fichefet, T., Friedlingstein, P., ... & Booth, B. B. (2013). Long-term climate change: projections, commitments and irreversibility. In Climate change 2013-The physical science basis: Contribution of working group I to the fifth assessment report of the intergovernmental panel on climate change (pp. 1029-1136). Cambridge University Press.

Cook, K. H., & Vizy, E. K. (2010). Hydrodynamics of the Caribbean low-level jet and its relationship to precipitation. Journal of Climate, 23(6), 1477-1494. https://doi.org/10.1175/2009JCLI3210.1

Correa Sánchez, N. (2020). Caracterización de la radiación solar para la estimación del potencial de energía fotovoltaica en entornos urbanos, caso de estudio: Valle de Aburrá. Universidad Nacional de Colombia.

Correa, A., Ochoa-Tocachi, B. F., Birkel, C., Ochoa-Sánchez, A., Zogheib, C., Tovar, C., & Buytaert, W. (2020). A concerted research effort to advance the hydrological understanding of tropical páramos. Hydrological Processes, 34(24), 4609-4627. doi: 10.1002/hyp.13904

Danabasoglu, Gokhan (2019). NCAR CESM2-FV2 model output prepared for CMIP6 CMIP historical. Version 20191120. Earth System Grid Federation. https://doi.org/10.22033/ESGF/CMIP6.11297

Danco, J. F., & Martin, E. R. (2018). Understanding the influence of ENSO on the Great Plains low-level jet in CMIP5 models. Climate Dynamics, 51(4), 1537-1558. doi: 10.1007/s00382-017-3970-9

Delworth, T. L., Broccoli, A. J., Rosati, A., Stouffer, R. J., Balaji, V., Beesley, J. A., ... Zhang, R. (2006). GFDL's CM2 global coupled climate models. Part I: Formulation and simulation characteristics. Journal of Climate, 19(5), 643-674. https://doi.org/10.1175/JCLI3629.1

Dix, M., Vohralik, P., Bi, D., Rashid, H., Marsland, S., O'Farrell, S., ... & Puri, K. (2013). The ACCESS coupled model: documentation of core CMIP5 simulations and initial results. Aust. Meteorol. Oceanogr. J, 63(1), 83-99.

Donner, L. J., Wyman, B. L., Hemler, R. S., Horowitz, L. W., Ming, Y., Zhao, M., ... & Zeng, F. (2011). The dynamical core, physical parameterizations, and basic simulation characteristics of the atmospheric component AM3 of the GFDL global coupled model CM3. Journal of Climate, 24(13), 3484-3519. doi:10.1175/2011JCLI3955.1.

Douville, H., K. Raghavan, J. Renwick, R.P. Allan, P.A. Arias, M. Barlow, R. Cerezo-Mota, A. Cherchi, T.Y. Gan, J. Gergis, D. Jiang, A. Khan, W. Pokam Mba, D. Rosenfeld, J. Tierney, & O. Zolina. (2021). Water Cycle Changes. In Climate Change 2021: The Physical Science Basis. Contribution of Working Group I to the Sixth Assessment Report of the Intergovernmental Panel on Climate Change [Masson-Delmotte, V., P. Zhai, A. Pirani, S.L. Connors, C. Péan, S. Berger, N. Caud, Y. Chen, L. Goldfarb, M.I. Gomis, M. Huang, K. Leitzell, E. Lonnoy, J.B.R. Matthews, T.K. Maycock, T. Waterfield, O. Yelekçi, R. Yu, and B. Zhou (eds.)]. Cambridge University Press, Cambridge, United Kingdom and New York, NY, USA, pp. 1055–1210, doi:10.1017/9781009157896.010.

Dufresne, J. L., Foujols, M. A., Denvil, S., Caubel, A., Marti, O., Aumont, O., ... & Vuichard, N. (2013). Climate change projections using the IPSL-CM5 Earth System Model: from CMIP3 to CMIP5. Climate dynamics, 40(9), 2123-2165. https://doi.org/10.1007/s00382-012-1636-1

Dunne, J. P., John, J. G., Adcroft, A. J., Griffies, S. M., Hallberg, R. W., Shevliakova, E., ... & Zadeh, N. (2012). GFDL's ESM2 global coupled climate–carbon earth system models. Part I: Physical formulation and baseline simulation characteristics. Journal of climate, 25(19), 6646-6665. https://doi.org/10.1175/JCLI-D-11-00560.1

Dunne, J. P., Horowitz, L. W., Adcroft, A. J., Ginoux, P., Held, I. M., John, J. G., ... & Zhao, M. (2020). The GFDL Earth System Model version 4.1 (GFDL-ESM 4.1): Overall coupled model description and simulation characteristics. Journal of Advances in Modeling Earth Systems, 12(11), e2019MS002015. https://doi.org/10.1029/2019MS002015

Eiras-Barca, J., Dominguez, F., Yang, Z., Chug, D., Nieto, R., Gimeno, L., & Miguez-Macho, G. (2020). Changes in South American hydroclimate under projected Amazonian deforestation. Annals of the New York Academy of Sciences, 1472(1), 104-122. https://doi.org/10.1111/nyas.14364

Espinoza, J. C., Garreaud, R., Poveda, G., Arias, P. A., Molina-Carpio, J., Masiokas, M., ... & Scaff, L. (2020). Hydroclimate of the Andes Part I: main climatic features. Frontiers in Earth Science, 64. doi: 10.3389/feart.2020.00064.

Eyring, V., Bony, S., Meehl, G. A., Senior, C. A., Stevens, B., Stouffer, R. J., & Taylor, K. E. (2016). Overview of the Coupled Model Intercomparison Project Phase 6 (CMIP6) experimental design and organization. Geoscientific Model Development, 9(5), 1937-1958. https://doi.org/10.5194/gmd-9-1937-2016

Ferguson, C. R. (2022). Changes in Great Plains Low-Level Jet Structure and Associated Precipitation Over the 20th Century. Journal of Geophysical Research: Atmospheres, 127(3), e2021JD035859. https://doi.org/10.1029/2021JD035859

Flato, G., J. Marotzke, B. Abiodun, P. Braconnot, S.C. Chou, W. Collins, P. Cox, F. Driouech, S. Emori, V. Eyring, C. Forest, P. Gleckler, E. Guilyardi, C. Jakob, V. Kattsov, C. Reason and M. Rummukainen. (2013): Evaluation of Climate Models. In: Climate Change 2013: The Physical Science Basis. Contribution of Working Group I to the Fifth Assessment Report of the Intergovernmental Panel on Climate Change [Stocker, T.F., D. Qin, G.-K. Plattner, M. Tignor, S.K. Allen, J. Boschung, A. Nauels, Y. Xia, V. Bex and P.M. Midgley (eds.)]. Cambridge University Press, Cambridge, United Kingdom and New York, NY, USA.

Fox-Kemper, B., H.T. Hewitt, C. Xiao, G. Aðalgeirsdóttir, S.S. Drijfhout, T.L. Edwards, N.R. Golledge, M. Hemer, R.E. Kopp, G. Krinner, A. Mix, D. Notz, S. Nowicki, I.S. Nurhati, L. Ruiz, J.-B. Sallée, A.B.A. Slangen, Y. Yu. (2021). Ocean, Cryosphere and Sea Level Change. In Climate Change 2021: The Physical Science Basis. Contribution of Working Group I to the Sixth Assessment Report of the Intergovernmental Panel on Climate Change [Masson-Delmotte, V., P. Zhai, A. Pirani, S.L. Connors, C. Péan, S. Berger, N. Caud, Y. Chen, L. Goldfarb, M.I. Gomis, M. Huang, K. Leitzell, E. Lonnoy, J.B.R. Matthews, T.K. Maycock, T. Waterfield, O.

Yelekçi, R. Yu, and B. Zhou (eds.)]. Cambridge University Press, Cambridge, United Kingdom and New York, NY, USA, pp. 1211–1362, doi:10.1017/9781009157896.011.

Gimeno, L., Stohl, A., Trigo, R. M., Dominguez, F., Yoshimura, K., Yu, L., ... & Nieto, R. (2012). Oceanic and terrestrial sources of continental precipitation. Reviews of Geophysics, 50(4). https://doi.org/10.1029/2012RG000389

Gimeno, L., Dominguez, F., Nieto, R., Trigo, R., Drumond, A., Reason, C. J., ... & Marengo, J. (2016). Major mechanisms of atmospheric moisture transport and their role in extreme precipitation events. Annual Review of Environment and Resources, 41, 117-141.

Giorgetta, M. A., Jungclaus, J., Reick, C. H., Legutke, S., Bader, J., Böttinger, M., ... & Stevens, B. (2013). Climate and carbon cycle changes from 1850 to 2100 in MPI-ESM simulations for the Coupled Model Intercomparison Project phase 5. Journal of Advances in Modeling Earth Systems, 5(3), 572-597. https://doi.org/10.1002/jame.20038

Golaz, J. C., Caldwell, P. M., Van Roekel, L. P., Petersen, M. R., Tang, Q., Wolfe, J. D., ... & Zhu, Q. (2019). The DOE E3SM coupled model version 1: Overview and evaluation at standard resolution. Journal of Advances in Modeling Earth Systems, 11(7), 2089-2129. https://doi.org/10.1029/2018MS001603

Gordon, C., Cooper, C., Senior, C. A., Banks, H., Gregory, J. M., Johns, T. C., ... & Wood, R. A. (2000). The simulation of SST, sea ice extents and ocean heat transports in a version of the Hadley Centre coupled model without flux adjustments. Climate dynamics, 16(2), 147-168.

Grose, M. R., Narsey, S., Delage, F. P., Dowdy, A. J., Bador, M., Boschat, G., ... & Power, S. (2020). Insights from CMIP6 for Australia's future climate. Earth's Future, 8(5), e2019EF001469. https://doi.org/10.1029/2019EF001469

Gulev, S.K., P.W. Thorne, J. Ahn, F.J. Dentener, C.M. Domingues, S. Gerland, D. Gong, D.S. Kaufman, H.C. Nnamchi, J. Quaas, J.A. Rivera, S. Sathyendranath, S.L. Smith, B. Trewin, K. von Schuckmann, & R.S. Vose. (2021): Changing State of the Climate System. In Climate Change 2021: The Physical Science Basis. Contribution

of Working Group I to the Sixth Assessment Report of the Intergovernmental Panel on Climate Change [Masson-Delmotte, V., P. Zhai, A. Pirani, S.L. Connors, C. Péan, S. Berger, N. Caud, Y. Chen, L. Goldfarb, M.I. Gomis, M. Huang, K. Leitzell, E. Lonnoy, J.B.R. Matthews, T.K. Maycock, T. Waterfield, O. Yelekçi, R. Yu, and B. Zhou (eds.)]. Cambridge University Press, Cambridge, United Kingdom and New York, NY, USA, pp. 287–422, doi:10.1017/9781009157896.004. Hersbach, H., Bell, B., Berrisford, P., Hirahara, S., Horányi, A., Muñoz-Sabater, J., ... Thépaut, J. N. (2020). The ERA5 global reanalysis. Quarterly Journal of the Royal Meteorological Society, 146(730), 1999-2049. doi: 10.1002/qj.3803

Hourdin, F., Grandpeix, J. Y., Rio, C., Bony, S., Jam, A., Cheruy, F., ... & Roehrig, R. (2013b). From LMDZ5A to LMDZ5B: revisiting the parameterizations of clouds and convection in the atmosperic component of the IPSL-CM5 climate model. Clim Dyn. doi:10.1007/s00382-012-1411-3.

IPCC. (2021). Summary for Policymakers. In: Climate Change 2021: The Physical Science Basis. Contribution of Working Group I to the Sixth Assessment Report of the Intergovernmental Panel on Climate Change [Masson-Delmotte, V., P. Zhai, A. Pirani, S.L. Connors, C. Péan, S. Berger, N. Caud, Y. Chen, L. Goldfarb, M.I. Gomis, M. Huang, K. Leitzell, E. Lonnoy, J.B.R. Matthews, T.K. Maycock, T. Waterfield, O. Yelekçi, R. Yu, and B. Zhou (eds.)]. Cambridge University Press, Cambridge, United Kingdom and New York, NY, USA, pp. 332, doi:10.1017/9781009157896.001.

Jeffrey, S., Rotstayn, L., Collier, M., Dravitzki, S., Hamalainen, C., Moeseneder, C., ... & Syktus, J. (2013). Australia's CMIP5 submission using the CSIRO-Mk3. 6 model. Aust. Meteor. Oceanogr. J, 63(1), 1-14.

Jiménez-Sánchez, G., Markowski, P. M., Jewtoukoff, V., Young, G. S., & Stensrud, D. J. (2019). The Orinoco low-level jet: An investigation of its characteristics and evolution using the WRF model. Journal of Geophysical Research: Atmospheres, 124(20), 10696-10711. https://doi.org/10.1029/2019JD030934

Jiménez-Sánchez, G., Markowski, P. M., Young, G. S., & Stensrud, D. J. (2020). The Orinoco low-level jet: An investigation of its mechanisms of formation using the WRF

model. Journal of Geophysical Research: Atmospheres, 125(13), e2020JD032810. https://doi.org/10.1029/2020JD032810

Jones, C. (2019). Recent changes in the South America low-level jet. Npj Climate and Atmospheric Science, 2(1), 1-8. https://doi.org/10.1038/s41612-019-0077-5

Kaiser, H.F., (1958). The varimax criterion for analytic rotation in factor analysis. Psychometrika, 23, 187–200.

Kelley, M., Schmidt, G. A., Nazarenko, L. S., Bauer, S. E., Ruedy, R., Russell, G. L., ... & Yao, M. S. (2020). GISS-E2. 1: Configurations and climatology. Journal of Advances in Modeling Earth Systems, 12(8), e2019MS002025. https://doi.org/10.1029/2019MS002025

Kendall, M. G. (1948). Rank correlation methods.

Kodinariya, T. M., & Makwana, P. R. (2013). Review on determining number of Cluster in K-Means Clustering. International Journal, 1(6), 90-95.

Krishnan, R., Swapna, P., Choudhury, A. D., Narayansetti, S., Prajeesh, A. G., Singh, M., ... & Ingle, S. (2021). The IITM Earth System Model (IITM ESM). arXiv preprint arXiv:2101.03410. https://doi.org/10.48550/arXiv.2101.03410

Labar, R. J., Douglas, M., Murillo, J., & Mejia, J. F. (2005). The Llanos low-level jet and its association with Venezuelan convective precipitation. Weather, 98926(August), 1–21.

Lee, J., Kim, J., Sun, M. A., Kim, B. H., Moon, H., Sung, H. M., ... & Byun, Y. H. (2020). Evaluation of the Korea meteorological administration advanced community earth-system model (K-ACE). Asia-Pacific Journal of Atmospheric Sciences, 56(3), 381-395. https://doi.org/10.1007/s13143-019-00144-7

Lee, J. Y., Marotzke, J., Bala, G., Cao, L., Corti, S., Dunne, J. P., ... & Zappa, G. (2021). Future global climate: scenario-based projections and near-term information. IPCC.

Liu, B., Tan, X., Gan, T. Y., Chen, X., Lin, K., Lu, M., & Liu, Z. (2020). Global atmospheric moisture transport associated with precipitation extremes: Mechanisms

and climate change impacts. Wiley Interdisciplinary Reviews: Water, 7(2), e1412. https://doi.org/10.1002/wat2.1412

Llopart, M., Simões Reboita, M., & Porfírio da Rocha, R. (2020). Assessment of multi-model climate projections of water resources over South America CORDEX domain. Climate Dynamics, 54(1), 99-116. https://doi.org/10.1007/s00382-019-04990-z

Loaiza Cerón, W., Andreoli, R. V., Kayano, M. T., Ferreira de Souza, R. A., Jones, C., & Carvalho, L. M. (2020). The influence of the atlantic multidecadal oscillation on the choco low-level jet and precipitation in colombia. Atmosphere, 11(2), 174. https://doi.org/10.3390/atmos11020174

Magrin, G.O., J.A. Marengo, J.-P. Boulanger, M.S. Buckeridge, E. Castellanos, G. Poveda, F.R. Scarano, & S. Vicuña. (2014). Central and South America. In: Climate Change 2014: Impacts, Adaptation, and Vulnerability. Part B: Regional Aspects. Contribution of Working Group II to the Fifth Assessment Report of the Intergovernmental Panel on Climate Change [Barros, V.R., C.B. Field, D.J. Dokken, M.D. Mastrandrea, K.J. Mach, T.E. Bilir, M. Chatterjee, K.L. Ebi, Y.O. Estrada, R.C. Genova, B. Girma, E.S. Kissel, A.N. Levy, S. MacCracken, P.R. Mastrandrea, and L.L. White (eds.)]. Cambridge University Press, Cambridge, United Kingdom and New York, NY, USA, pp. 1499-1566.

Makinde, A. I., Abiodun, B. J., James, R., Washington, R., Dyer, E., & Webb, T. (2022). How Well Do CMIP6 Models Simulate the Influence of the West African Westerly Jet on Sahel Precipitation? https://doi.org/10.21203/rs.3.rs-1274137/v1

Mann, H. B. (1945). Nonparametric tests against trend. Econometrica: Journal of the econometric society, 245-259.

Martin, E. R., & Schumacher, C. (2011). The Caribbean low-level jet and its relationship with precipitation in IPCC AR4 models. Journal of Climate, 24(22), 5935-5950. doi: 10.1175/JCLI-D-11-00134.1

Martinez, J. A., Arias, P. A., Junquas, C., Espinoza, J. C., Condom, T., Dominguez, F., & Morales, J. S. (2022). The Orinoco Low-Level Jet and the Cross-Equatorial

Moisture Transport Over Tropical South America: Lessons from Seasonal WRF Simulations. Journal of Geophysical Research: Atmospheres, 127(3), e2021JD035603. https://doi.org/10.1029/2021JD035603

Mauritsen, T., Bader, J., Becker, T., Behrens, J., Bittner, M., Brokopf, R., ... & Roeckner, E. (2019). Developments in the MPI-M Earth System Model version 1.2 (MPI-ESM1. 2) and its response to increasing CO2. Journal of Advances in Modeling Earth Systems, 11(4), 998-1038. https://doi.org/10.1029/2018MS001400

Meinshausen, M., Smith, S. J., Calvin, K., Daniel, J. S., Kainuma, M. L., Lamarque, J. F., ... & Van Vuuren, D. P. P. (2011). The RCP greenhouse gas concentrations and their extensions from 1765 to 2300. Climatic change, 109(1), 213-241. doi: 10.1007/s10584-011-0156-z

Meinshausen, M., Nicholls, Z. R., Lewis, J., Gidden, M. J., Vogel, E., Freund, M., ... & Wang, R. H. (2020). The shared socio-economic pathway (SSP) greenhouse gas concentrations and their extensions to 2500. Geoscientific Model Development, 13(8), 3571-3605. https://doi.org/10.5194/gmd-13-3571-2020

Merryfield, W. J., Lee, W. S., Boer, G. J., Kharin, V. V., Scinocca, J. F., Flato, G. M., ... & Polavarapu, S. (2013). The Canadian seasonal to interannual prediction system. Part I: Models and initialization. Monthly weather review, 141(8), 2910-2945. https://doi.org/10.1175/MWR-D-12-00216.1

Mesa, O., Urrea, V., & Ochoa, A. (2021). Trends of hydroclimatic intensity in Colombia. Climate, 9(7), 120. https://doi.org/10.3390/cli9070120

Molod, A., Salmun, H., & Marquardt Collow, A. B. (2019). Annual cycle of planetary boundary layer heights estimated from wind profiler network data. Journal of Geophysical Research: Atmospheres, 124(12), 6207-6221. https://doi.org/10.1029/2018JD030102

Montoya G., G., Pelkowski, J., & Eslava R., J. A. (2001). Sobre los alisios del nordeste y la existencia de una corriente en el piedemonte oriental andino. Revista de la Academia Colombiana de Ciencias Exactas, Fisicas y Naturales, 25(96), 363+.

https://link.gale.com/apps/doc/A498583713/IFME?u=googlescholar&sid=bookmark-IFME&xid=2e07c8fa

Montini, T. L., Jones, C., & Carvalho, L. M. (2019). The South American low-level jet: a new climatology, variability, and changes. Journal of Geophysical Research: Atmospheres, 124(3), 1200-1218. https://doi.org/10.1029/2018JD029634

Morales, J. S., Arias, P. A., Martínez, J. A., & Durán-Quesada, A. M. (2021). The role of low-level circulation on water vapour transport to central and northern South America: Insights from a 2D Lagrangian approach. International Journal of Climatology, 41, E2662-E2682. https://doi.org/10.1002/joc.6873

Munday, C., Washington, R., & Hart, N. (2021). African low-level jets and their importance for water vapor transport and rainfall. Geophysical Research Letters, 48(1), e2020GL090999. https://doi.org/10.1029/2020GL090999

Muñoz, E., Busalacchi, A. J., Nigam, S., & Ruiz-Barradas, A. (2008). Winter and summer structure of the Caribbean low-level jet. Journal of Climate, 21(6), 1260-1276. https://doi.org/10.1175/2007JCLI1855.1

Nagy, G. J., Gutierrez, O., Brugnoli, E., Verocai, J. E., Gomez-Erache, M., Villamizar, A., ... & Amaro, N. (2019). Climate vulnerability, impacts and adaptation in Central and South America coastal areas. Regional Studies in Marine Science, 29, 100683. https://doi.org/10.1016/j.rsma.2019.100683

Navarro-Monterroza, E., Arias, P. A., ? Vieira, S. C. (2019). El Niño-Oscilación del Sur, fase Modoki, y sus efectos en la variabilidad espacio-temporal de la precipitación en Colombia. Revista de la Academia Colombiana de Ciencias Exactas, Físicas y Naturales, 43(166), 120-132. ?urlhttp://dx.doi.org/10.18257/raccefyn.704

Nieto, R., Gallego, D., Trigo, R., Ribera, P., & Gimeno, L. (2008). Dynamic identification of moisture sources in the Orinoco basin in equatorial South America. Hydrological sciences journal, 53(3), 602-617. https://doi.org/10.1623/hysj.53.3.602

O'Connor, J. C., Santos, M. J., Dekker, S. C., Rebel, K. T., & Tuinenburg, O. A. (2021). Atmospheric moisture contribution to the growing season in the Amazon arc

of deforestation. Environmental Research Letters, 16(8), 084026. https://doi.org/10.1088/1748-9326/ac12f0

O'Neill, B. C., Tebaldi, C., Van Vuuren, D. P., Eyring, V., Friedlingstein, P., Hurtt, G., ... & Sanderson, B. M. (2016). The scenario model intercomparison project (ScenarioMIP) for CMIP6. Geoscientific Model Development, 9(9), 3461-3482. doi:10.5194/gmd-9-3461-2016

Olmo, M. E., Espinoza, J. C., Bettolli, M. L., Sierra, J. P., Junquas, C., Arias, P. A., ... & Balmaceda-Huarte, R. (2022). Circulation patterns and associated rainfall over South Tropical South America: GCMs evaluation during the dry-to-wet transition season. Journal of Geophysical Research: Atmospheres, e2022JD036468. doi: 10.1029/2022JD036468.

Ortega, G., & Arias, P. A. (2018). Evaluación de la representación de la precipitación y la temperatura media por modelos CMIP5 sobre Colombia y el neotrópico: implicaciones en regímenes hidrológicos. Sociedad Colombiana de Ingenieros XXIII Seminario Nacional de Hidráulica e Hidrología.

Ortega, G., Arias, P. A., Villegas, J. C., Marquet, P. A., & Nobre, P. (2021). Present-day and future climate over central and South America according to CMIP5/CMIP6 models. International Journal of Climatology, 41(15), 6713-6735. doi: 10.1002/joc.7221

Oscar, L., Nzau, M. J., Ellen, D., Franklin, O., Rachel, J., Richard, W., & Tom, W. (2022). Characteristics of the Turkana low-level jet stream and the associated rainfall in CMIP6 models. Climate Dynamics, 1-17. https://doi.org/10.1007/s00382-022-06499-4.

Pabón-Caicedo, J. D., Arias, P. A., Carril, A. F., Espinoza, J. C., Borrel, L. F., Goubanova, K., ... & Villalba, R. (2020). Observed and projected hydroclimate changes in the Andes. Frontiers in Earth Science, 8, 61. doi: 10.3389/feart.2020.00061

Pak, G., Noh, Y., Lee, M. I., Yeh, S. W., Kim, D., Kim, S. Y., ... & Kim, Y. H. (2021). Korea institute of ocean science and technology earth system model and its simulation characteristics. Ocean Science Journal, 56(1), 18-45. https://doi.org/10.1007/s12601-021-00001-7

Park, S., Shin, J., Kim, S., Oh, E., & Kim, Y. (2019). Global climate simulated by the Seoul National University atmosphere model version 0 with a unified convection scheme (SAM0-UNICON). Journal of Climate, 32(10), 2917-2949. https://doi.org/10.1175/JCLI-D-18-0796.1

Pascale, S., Carvalho, L., Adams, D. K., Castro, C. L., & Cavalcanti, I. F. (2019). Current and future variations of the monsoons of the Americas in a warming climate. Current Climate Change Reports, 5(3), 125-144. https://doi.org/10.1007/s40641-019-00135-w

Poveda, G., & Mesa, O. (1999). La corriente de chorro superficial del Oeste ("del Chocó") y otras dos corrientes de chorro en Colombia: climatología y variabilidad durante las fases del ENSO. Revista Académica Colombiana de Ciencia, 23(89), 517-528.

Poveda, G. (2004). La hidroclimatología de Colombia: una síntesis desde la escala inter-decadal hasta la escala diurna. Rev. Acad. Colomb. Cienc, 28(107), 201-222.

Poveda, G., Jaramillo, L., & Vallejo, L. F. (2014). Seasonal precipitation patterns along pathways of South American low-level jets and aerial rivers. Water Resources Research, 50(1), 98-118. doi:10.1002/2013WR014087

Ramírez-Tovar, A., Moreno, R., & Carrillo-Rodríguez, L. A. (2021). The Colombian Energy Policy Challenges in Front of Climate Change. International Journal of Energy Economics and Policy, 11(6), 401–407. https://doi.org/10.32479/ijeep.10517

Ramos, A. M., Blamey, R. C., Algarra, I., Nieto, R., Gimeno, L., Tomé, R., ... & Trigo, R. M. (2019). From Amazonia to southern Africa: Atmospheric moisture transport through low-level jets and atmospheric rivers. Annals of the New York Academy of Sciences, 1436(1), 217-230. https://doi.org/10.1111/nyas.13960

Ramos, A. M., Nieto, R., Tomé, R., Gimeno, L., Trigo, R. M., Liberato, M. L., & Lavers, D. A. (2016). Atmospheric rivers moisture sources from a Lagrangian perspective. Earth System Dynamics, 7(2), 371-384. https://doi.org/10.5194/esd-7-371-2016

Ranjha, R., Svensson, G., Tjernström, M., & Semedo, A. (2013). Global distribution

and seasonal variability of coastal low-level jets derived from ERA-Interim reanalysis. Tellus A: Dynamic Meteorology and Oceanography, 65(1), 20412. https://doi.org/10.3402/tellusa.v65i0.20412

Reboita, M. S., da Rocha, R. P., Dias, C. G., & Ynoue, R. Y. (2014). Climate projections for South America: RegCM3 driven by HadCM3 and ECHAM5. Advances in Meteorology, 2014. http://dx.doi.org/10.1155/2014/376738

Rencher AC (2003) Methods of multivariate analysis, vol 492. Wiley, New Jersey Reyer, C. P., Adams, S., Albrecht, T., Baarsch, F., Boit, A., Canales Trujillo, N., ... Thonicke, K. (2017). Climate change impacts in Latin America and the Caribbean and their implications for development. Regional Environmental Change, 17(6), 1601-1621. https://doi.org/10.1007/s10113-015-0854-6

Riahi, K., Rao, S., Krey, V., Cho, C., Chirkov, V., Fischer, G., ... & Rafaj, P. (2011). RCP 8.5—A scenario of comparatively high greenhouse gas emissions. Climatic change, 109(1), 33-57. https://doi.org/10.1007/s10584-011-0149-y

Rife, D. L., Pinto, J. O., Monaghan, A. J., Davis, C. A., & Hannan, J. R. (2010). Global distribution and characteristics of diurnally varying low-level jets. Journal of Climate, 23(19), 5041-5064. doi: 10.1175/2010JCLI3514.1

Rind, D., Orbe, C., Jonas, J., Nazarenko, L., Zhou, T., Kelley, M., ... & Schmidt, G. (2020). GISS Model E2. 2: A climate model optimized for the middle atmosphere—Model structure, climatology, variability, and climate sensitivity. Journal of Geophysical Research: Atmospheres, 125(10), e2019JD032204. https://doi.org/10.1029/2019JD032204

Rodríguez-Gómez, C., Echeverry, G., Jaramillo, A., & Ladino, L. A. (2022). The negative impact of biomass burning and the Orinoco low-level jet on the air quality of the Orinoco River Basin. Atmósfera, 35(3), 497-520. https://doi.org/10.20937/ATM.52979

Romanou, A., Gregg, W. W., Romanski, J., Kelley, M., Bleck, R., Healy, R., ... & Tausnev, N. (2013). Natural air–sea flux of CO2 in simulations of the NASA-

GISS climate model: Sensitivity to the physical ocean model formulation. Ocean Modelling, 66, 26-44. doi: 10.1016/j.ocemod.2013.01.008, 2013.

Rousseeuw, P. J. (1987). Silhouettes: a graphical aid to the interpretation and validation of cluster analysis. Journal of computational and applied mathematics, 20, 53-65. https://doi.org/10.1016/0377-0427(87)90125-7

Rueda, C. (2015). Caracterización de la corriente en chorro de bajo nivel de los llanos orientales colombianos (Characterization of the low-level jet over the Colombian Eastern llanos). Bogotá, Colombia: Universidad Nacional de Colombia.

Ruiz-Vásquez, M., Arias, P. A., Martínez, J. A., & Espinoza, J. C. (2020). Effects of Amazon basin deforestation on regional atmospheric circulation and water vapor transport towards tropical South America. Climate Dynamics, 54(9), 4169-4189. https://doi.org/10.1007/s00382-020-05223-4

Sakamoto, T. T., Komuro, Y., Nishimura, T., Ishii, M., Tatebe, H., Shiogama, H., ... & Kimoto, M. (2012). MIROC4h—a new high-resolution atmosphere-ocean coupled general circulation model. Journal of the Meteorological Society of Japan. Ser. II, 90(3), 325-359. https://doi.org/10.2151/jmsj.2012-301

San José, J. J., Montes, R., & Mazorra, M. (1998). The nature of savanna heterogeneity in the Orinoco Basin. Global Ecology Biogeography Letters, 7(6), 441-455.

Satyamurty, P., Nobre, C. A., & Silva Dias, P. L. (1998). South America. In Meteorology of the southern hemisphere (pp. 119-139). American Meteorological Society, Boston, MA. https://doi.org/10.1007/978-1-935704-10-2_5

Schmidt, G. A., Kelley, M., Nazarenko, L., Ruedy, R., Russell, G. L., Aleinov, I., ... & Zhang, J. (2014). Configuration and assessment of the GISS ModelE2 contributions to the CMIP5 archive. Journal of Advances in Modeling Earth Systems, 6(1), 141-184. https://doi.org/10.1002/2013MS000265

Scoccimarro, E., Gualdi, S., Bellucci, A., Sanna, A., Giuseppe Fogli, P., Manzini, E., ... & Navarra, A. (2011). Effects of tropical cyclones on ocean heat transport in a high-resolution coupled general circulation model. Journal of Climate, 24(16), 4368-4384. https://doi.org/10.1175/2011JCLI4104.1

Segura, H., Espinoza, J. C., Junquas, C., Lebel, T., Vuille, M., & Garreaud, R. (2020). Recent changes in the precipitation-driving processes over the southern tropical Andes/western Amazon. Climate Dynamics, 54(5), 2613-2631. https://doi.org/10.1007/s00382-020-05132-6

Seland, Ø., Bentsen, M., Olivié, D., Toniazzo, T., Gjermundsen, A., Graff, L. S., ... & Schulz, M. (2020). Overview of the Norwegian Earth System Model (NorESM2) and key climate response of CMIP6 DECK, historical, and scenario simulations. Geoscientific Model Development, 13(12), 6165-6200. https://doi.org/10.5194/gmd-13-6165-2020

Sénési, S., Richon, J., Franchistéguy, L., Tyteca, S., Moine, M. P., Voldoire, A., ... & Chauvin, F. (2011). CNRM-CM5-2 model output prepared for CMIP5 piControl, served by ESGF. https://doi.org/10.1594/WDCC/CMIP5.CEF5pc

Seneviratne, S. I., Zhang, X., Adnan, M., Badi, W., Dereczynski, C., Di Luca, A., ... & Zhou, B. (2021). 11 Chapter 11: Weather and climate extreme events in a changing climate. doi:10.1017/9781009157896.013

Sepulchre, P., Caubel, A., Ladant, J. B., Bopp, L., Boucher, O., Braconnot, P., ... & Tardif, D. (2020). IPSL-CM5A2–an Earth system model designed for multi-millennial climate simulations. Geoscientific Model Development, 13(7), 3011-3053. https://doi.org/10.5194/gmd-2019-332

Sierra, J. P. (2017). The Choco low-level jet in CMIP5 experiments: present and future (Tesis de maestría). Universidad de Antioquia, Medellín, Colombia.

Sierra, J. P., Arias, P. A., Vieira, S. C., & Agudelo, J. (2018). How well do CMIP5 models simulate the low-level jet in western Colombia? Climate Dynamics, 51(5), 2247-2265. https://doi.org/10.1007/s00382-017-4010-5

Sierra, J. P., Arias, P. A., Durán-Quesada, A. M., Tapias, K. A., Vieira, S. C., & Martínez, J. A. (2021). The Choco low-level jet: past, present and future. Climate Dynamics, 56(7), 2667-2692. https://doi.org/10.1007/s00382-020-05611-w

Sierra, J. P., Junquas, C., Espinoza, J. C., Segura, H., Condom, T., Andrade, M., ... & Sicart, J. E. (2022). Deforestation impacts on Amazon-Andes hydroclimatic

connectivity. Climate Dynamics, 58(9), 2609-2636. https://doi.org/10.1007/s00382-021-06025-y

Sheffield, J., Barrett, A. P., Colle, B., Nelun Fernando, D., Fu, R., Geil, K. L., ... & Yin, L. (2013). North American climate in CMIP5 experiments. Part I: Evaluation of historical simulations of continental and regional climatology. Journal of Climate, 26(23), 9209-9245. doi: 10.1175/JCLI-D-12-00592.1

Stensrud, D. J. (1996). Importance of low-level jets to climate: A review. Journal of Climate, 1698-1711.

Soares, W. R., & Marengo, J. A. (2009). Assessments of moisture fluxes east of the Andes in South America in a global warming scenario. International Journal of Climatology: A Journal of the Royal Meteorological Society, 29(10), 1395-1414. doi: 10.1002/joc.1800

Stouffer, R. J. (2019). UA MCM-UA-1-0 model output prepared for CMIP6 CMIP historical, Earth System Grid Federation. https://doi.org/10.22033/ESGF/CMIP6.8888

Swart, N. C., Cole, J. N., Kharin, V. V., Lazare, M., Scinocca, J. F., Gillett, N. P., ... & Winter, B. (2019). The Canadian earth system model version 5 (CanESM5. 0.3). Geoscientific Model Development, 12(11), 4823-4873. https://doi.org/10.5194/gmd-12-4823-2019.

Tang, Y., Winkler, J., Zhong, S., Bian, X., Doubler, D., Yu, L., & Walters, C. (2017). Future changes in the climatology of the Great Plains low-level jet derived from fine resolution multi-model simulations. Scientific reports, 7(1), 1-10. https://doi.org/10.1038/s41598-017-05135-0

Tatebe, H., Ogura, T., Nitta, T., Komuro, Y., Ogochi, K., Takemura, T., ... & Kimoto, M. (2019). Description and basic evaluation of simulated mean state, internal variability, and climate sensitivity in MIROC6. Geoscientific Model Development, 12(7), 2727-2765. https://doi.org/10.5194/gmd-12-2727-2019

Taylor, K. E. (2001). Summarizing multiple aspects of model performance in a single diagram. Journal of Geophysical Research: Atmospheres, 106(D7), 7183-7192.

Taylor, K. E., Stouffer, R. J., & Meehl, G. A. (2012). An overview of CMIP5 and the experiment design. Bulletin of the American Meteorological Society, 93(4), 485-498. https://doi.org/10.1175/BAMS-D-11-00094.1

Thaler, V., Loikith, P. C., Mechoso, C. R., & Pampuch, L. A. (2021). A multivariate assessment of climate change projections over South America using the fifth phase of the Coupled Model Intercomparison Project. International Journal of Climatology, 41(8), 4265-4282. doi: 10.1002/joc.7072

Thomson, A. M., Calvin, K. V., Smith, S. J., Kyle, G. P., Volke, A., Patel, P., ... & Edmonds, J. A. (2011). RCP4. 5: a pathway for stabilization of radiative forcing by 2100. Climatic change, 109(1), 77-94. https://doi.org/10.1007/s10584-011-0151-4

Tjiputra, J. F., Roelandt, C., Bentsen, M., Lawrence, D. M., Lorentzen, T., Schwinger, J., ... & Heinze, C. (2013). Evaluation of the carbon cycle components in the Norwegian Earth System Model (NorESM). Geoscientific Model Development, 6(2), 301-325. doi:10.5194/gmd-6-301-2013.

Torrealba, E. R., & Amador, J. A. (2010). La corriente en chorro de bajo nivel sobre los Llanos Venezolanos de Sur América. Revista de climatología, 10.

Torres-Alavez, J. A., Das, S., Corrales-Suastegui, A., Coppola, E., Giorgi, F., Raffaele, F., ... & Sines, T. (2021). Future projections in the climatology of global low-level jets from CORDEX-CORE simulations. Climate Dynamics, 57(5), 1551-1569. https://doi.org/10.1007/s00382-021-05671-6

Valencia, J., & Mejía, J. F. (2022). Projected Changes of Day-to-Day Precipitation and Choco Low-Level Jet Relationships over the Far Eastern Tropical Pacific and Western Colombia from Two CMIP6 GCM Models. Atmosphere, 13(11), 1776. ht tps://doi.org/10.3390/atmos13111776

Vera, C., Baez, J., Douglas, M., Emmanuel, C. B., Marengo, J., Meitin, J., ... & Zipser, E. (2006). The South American low-level jet experiment. Bulletin of the American Meteorological Society, 87(1), 63-78. https://doi.org/10.1175/BAMS-8 7-1-63

Vichi, M., Manzini, E., Fogli, P. G., Alessandri, A., Patara, L., Scoccimarro, E., ...

& Navarra, A. (2011). Global and regional ocean carbon uptake and climate change: sensitivity to a substantial mitigation scenario. Climate dynamics, 37(9), 1929-1947.

Voldoire, A., Sanchez-Gomez, E., Salas y Mélia, D., Decharme, B., Cassou, C., Sénési, S., ... & Chauvin, F. (2013). The CNRM-CM5. 1 global climate model: description and basic evaluation. Climate dynamics, 40(9), 2091-2121.

Volodin, E. M., Diansky, N. A., & Gusev, A. V. (2013). Simulation and prediction of climate changes in the 19th to 21st centuries with the Institute of Numerical Mathematics, Russian Academy of Sciences, model of the Earth's climate system. Izvestiya, Atmospheric and Oceanic Physics, 49(4), 347-366. doi:10.1134/S0001433813040105

Volodin, E., & Gritsun, A. (2018). Simulation of observed climate changes in 1850–2014 with climate model INM-CM5. Earth System Dynamics, 9(4), 1235-1242. https://doi.org/10.5194/esd-9-1235-2018 Wang, H., Fu, R. (2002). Cross-equatorial flow and seasonal cycle of precipitation over South America. Journal of Climate, 15(13), 1591-1608. https://doi.org/10.117/1520-0442(2002)015<1591:CEFASC>2.0.CO;2

Wang, C. (2007). Variability of the Caribbean low-level jet and its relations to climate. Climate dynamics, 29(4), 411-422. doi: 10.1007/s00382-007-0243-z

Wang, Y., Sayit, H., Mamtimin, A., Zhu, J., Zhou, C., Huo, W., ... & Zhao, X. (2021). Evaluation of five planetary boundary layer schemes in WRF over China's largest semi-fixed desert. Atmospheric Research, 256, 105567. https://doi.org/10.101/j.atmosres.2021.105567

Ward Jr, J. H. (1963). Hierarchical grouping to optimize an objective function. Journal of the American statistical association, 58(301), 236-244.

Watanabe, M., Suzuki, T., O'ishi, R., Komuro, Y., Watanabe, S., Emori, S., ... & Kimoto, M. (2010). Improved climate simulation by MIROC5: mean states, variability, and climate sensitivity. Journal of Climate, 23(23), 6312-6335. https://doi.org/10.1175/2010JCLI3679.1

Watanabe, S., Hajima, T., Sudo, K., Nagashima, T., Takemura, T., Okajima, H., ...& Kawamiya, M. (2011). MIROC-ESM: model description and basic results of CMIP5-

20c3m experiments. Geosci Model Dev Discuss, 4(2), 1063-1128. doi:10.5194/gmdd-4-1063-2011

Weaver, S. J., & Nigam, S. (2008). Variability of the Great Plains low-level jet: Large-scale circulation context and hydroclimate impacts. Journal of Climate, 21(7), 1532-1551. doi: 10.1175/2007JCLI1586.1

Whyte, F. S., Taylor, M. A., Stephenson, T. S., & Campbell, J. D. (2007). Features of the Caribbean low-level jet. International Journal of Climatology: A Journal of the Royal Meteorological Society, 28(1), 119-128. https://doi.org/10.1002/joc.1510

Wierik, S. A., Cammeraat, E. L., Gupta, J., & Artzy-Randrup, Y. A. (2021). Reviewing the Impact of Land Use and Land-Use Change on Moisture Recycling and Precipitation Patterns. Water Resources Research, 57(7), e2020WR029234. https://doi.org/10.1029/2020WR029234

Wilks, D.S. (2006) Statistical Methods in the Atmospheric Sciences. 2nd Edition, Academic Press, London.

Wimhurst, J. J., Greene, J. S. (2020). The influence of climate change on low-level jet characteristics over the South-Central Plains as simulated by CMIP5 models. International Journal of Climatology, 40(14), 6020-6038. doi: 10.1002/joc.6563

Wu, T., Lu, Y., Fang, Y., Xin, X., Li, L., Li, W., ... & Liu, X. (2019). The Beijing Climate Center climate system model (BCC-CSM): the main progress from CMIP5 to CMIP6. Geoscientific Model Development, 12(4), 1573-1600. https://doi.org/10.5194/gmd-12-1573-2019.

Wu, T., Zhang, F., Zhang, J., Jie, W., Zhang, Y., Wu, F., ... & Hu, A. (2020). Beijing Climate Center Earth System Model version 1 (BCC-ESM1): model description and evaluation of aerosol simulations. Geoscientific Model Development, 13(3), 977-1005. https://doi.org/10.5194/gmd-13-977-2020

Xin-Yao, R. O. N. G., Jian, L. I., Hao-Ming, C. H. E. N., Yu-Fei, X. I. N., Jing-Zhi, S. U., & Li-Juan, H. U. A. (2019). Introduction of CAMS-CSM model and its participation in CMIP6. Advances in Climate Change Research, 15(5), 540. doi: 10.12006/j.issn.1673-1719.2019.186

Yang, Z., & Dominguez, F. (2019). Investigating land surface effects on the moisture transport over South America with a moisture tagging model. Journal of Climate, 32(19), 6627-6644. https://doi.org/10.1175/JCLI-D-18-0700.1

Yang, D., Yang, Y., & Xia, J. (2021). Hydrological cycle and water resources in a changing world: A review. Geography and Sustainability, 2(2), 115-122. https://doi.org/10.1016/j.geosus.2021.05.003

Yepes, J., Poveda, G., Mejía, J. F., Moreno, L., & Rueda, C. (2019). Choco-jex: A research experiment focused on the Chocó low-level jet over the far eastern Pacific and western Colombia. Bulletin of the American Meteorological Society, 100(5), 779-796. doi: 10.1175/BAMS-D-18-0045.1

Yukimoto, S., Yoshimura, H., Hosaka, M., Sakami, T., Tsujino, H., HIRABARA, M., ... & KITOH, A. (2011). Meteorological research institute-earth system model version 1 (MRI-ESM1)-model description. Technical Reports of the Meteorological Research Institute, (64), 92.

Yukimoto, S., Adachi, Y., Hosaka, M., Sakami, T., Yoshimura, H., Hirabara, M., ... & Kitoh, A. (2012). A new global climate model of the Meteorological Research Institute: MRI-CGCM3—Model description and basic performance—. Journal of the Meteorological Society of Japan. Ser. II, 90, 23-64. https://doi.org/10.2151/jmsj.2012-A02

Yukimoto, S., Kawai, H., Koshiro, T., Oshima, N., Yoshida, K., Urakawa, S., ... & Ishii, M. (2019). The Meteorological Research Institute Earth System Model version 2.0, MRI-ESM2. 0: Description and basic evaluation of the physical component. Journal of the Meteorological Society of Japan. Ser. II. https://doi.org/10.2151/jmsj.2019-051

Zaninelli, P. G., Menéndez, C. G., Falco, M., López-Franca, N., & Carril, A. F. (2019). Future hydroclimatological changes in South America based on an ensemble of regional climate models. Climate Dynamics, 52(1), 819-830. https://doi.org/10.1007/s00382-018-4225-0

Zhao, A., Ryder, C. L., & Wilcox, L. J. (2022). How well do the CMIP6 models

simulate dust aerosols?. Atmospheric Chemistry and Physics, 22(3), 2095-2119. https://doi.org/10.5194/acp-22-2095-2022

Zelinka, M. D., Myers, T. A., McCoy, D. T., Po-Chedley, S., Caldwell, P. M., Ceppi, P., ... & Taylor, K. E. (2020). Causes of higher climate sensitivity in CMIP6 models. Geophysical Research Letters, 47(1), e2019GL085782. https://doi.org/10.1029/2019GL085782

Zeng, Z., Wang, D., Yang, L., Wu, J., Ziegler, A. D., Liu, M., ... & Wood, E. F. (2021). Deforestation-induced warming over tropical mountain regions regulated by elevation. Nature Geoscience, 14(1), 23-29. https://doi.org/10.1038/s41561-020-00666-0

Ziehn, T., Chamberlain, M. A., Law, R. M., Lenton, A., Bodman, R. W., Dix, M., ... & Srbinovsky, J. (2020). The Australian earth system model: ACCESS-ESM1. 5. Journal of Southern Hemisphere Earth Systems Science, 70(1), 193-214. https://doi.org/10.1071/ES19035.